Diss. ETH No. 25572

Parametric resonance in classical and quantum systems

A thesis submitted to attain the degree of

DOCTOR OF SCIENCES of ETH ZURICH

(Dr. sc. ETH Zurich)

presented by

Luca Papariello

MSc ETH in Physics

born on July 8, 1989

citizen of Bellinzona (TI), Switzerland

accepted on the recommendation of

Prof. Dr. Manfred Sigrist, examiner
Dr. Chitra Ramasubramanian, co-examiner
Prof. Dr. Christoph Bruder, co-examiner

2018

Life is like riding a bicycle. To keep your balance, you must keep moving.

Albert Einstein

Abstract

FROM personal experience we all know that a child on a swing has two possibilities to increase his motion: ask a parent to push him or lower and raise his legs periodically in time. The second option is called parametric driving and the great ability to increase the oscillatory motion, which is obtained for wisely chosen excitation frequencies, is called parametric resonance. The subject matter of this thesis is the manifestation of parametric resonance, under different forms, in classical and quantum systems.

Much of the sensors around us can be described in terms of harmonic resonators. However, as resonators miniaturize, nonlinear effects become more pronounced and strongly restrict the dynamic range in which they can operate linearly. Our research proposes a new paradigm for the detection of small forces, which is the result of a complex interplay between parametric driving and nonlinearities. We provide a detailed theoretical description of the working principle of the proposed force detection scheme and the mechanism behind it. We also contributed to its first experimental demonstration.

In recent years parametric driving in quantum many-body systems has attracted considerable attention in experimental as well as in theoretical physics as it opens the doors to out-of-equilibrium phenomena that do no have equilibrium counterparts. An important example where interesting nonequilibrium phases and dynamical phase transitions emerge is in the quintessential Dicke model. This model, describing the interaction between a mode of quantized light and a collection of two-level systems, is an important pillar of quantum optics; its equilibrium counterpart is characterized by two phases: the normal and the superradiant phase, with a continuous quantum phase transition sepa-

rating the two. Recently, it was shown that when driven parametrically a novel phase emerges as a manifestation of many-body parametric resonance. This parametric resonance is identical in spirit to the one discussed above. In this thesis, we provide an exact study of this system, under driving and dissipation, and characterize the phase transitions across its phase diagram.

The last part of the thesis studies experimentally realistic models which are good candidates for realizing the many-body parametric resonance seen in the Dicke model. The experimental realization of the Dicke superradiant phase transition, predicted long ago, is very challenging as it requires relatively strong coupling between matter and light. This transition was only recently observed in a Bose-Einstein condensate coupled to an optical cavity. In this system the coupling strength between the atoms and the cavity field can be tuned by changing the amplitude of a pump laser. The easy controllability of this setup makes it the perfect candidate to implement the periodically modulated Dicke model and to test the emergence of many-body parametric resonance.

The last project deals indeed with the investigation of an interacting Bose gas coupled to a cavity and subject to a modulation of the laser pump amplitude. As the examination of this system involves studying a quantum many-body problem with time dependence, we resort to numerical methods. We thus exploit the capabilities of the Multi-Configurational Time-Dependent Hartree method for indistinguishable particles (MCTDH-X), to investigate the dynamics of the system. Parametric resonance gives rise to a phase not seen in the static scenario, in which the condensate oscillates between different lattice configurations and displays peculiar heating characteristics.

Sunto

Per esperienza personale tutti noi sappiamo che un bambino su un'altalena ha due possibilità per aumentare l'ampiezza delle proprie oscillazioni: chiedere a un genitore di spingerlo oppure alzare ed abbassare le gambe ad intervalli regolari. La seconda opzione è detta forzatura parametrica e la capacità di aumentare considerevolmente il moto oscillatorio scegliendo con accortezza la frequenza della forzatura è invece chiamata risonanza parametrica. L'oggetto di studio di questa tesi è la manifestazione, sotto diverse forme, della risonanza parametrica in sistemi classici e quantistici.

Gran parte dei sensori che ci circondano possono essere descritti in termini di oscillatori armonici. Tuttavia, con la miniaturizzazione dei risonatori, i fenomeni di natura non lineare acquisiscono rilevanza limitando notevolmente l'intervallo in cui operano linearmente. La nostra ricerca propone un nuovo paradigma per la misurazione di forze molto piccole, il quale risulta da una complessa interazione tra la forzatura parametrica e le nonlinearità. In questo lavoro forniamo un'accurata descrizione teorica dello schema proposto per la misurazione di forze e del meccanismo su cui si basa. Inoltre, abbiamo anche contribuito alla sua prima dimostrazione sperimentale.

La forzatura parametrica apre di fatto le porte a dei fenomeni fuori dell'equilibrio che non possiedono una controparte in equilibrio. Negli ultimi anni questo aspetto ha attirato considerevole interesse sia in fisica teorica che sperimentale. Un esempio emblematico dove emergono interessanti fasi di non equilibrio e transazioni di fase dinamiche è il rinomato modello di Dicke. Questo modello, che descrive l'interazione tra un modo di luce quantizzata e un insieme di sistemi a due livelli, è un pilastro importante dell'ottica quantistica. La sua controparte in equili-

brio è caratterizzata da due fasi: quella normale e quella superradiante, separate da una transizione di fase quantistica continua. Recentemente è stato dimostrato che in una situazione di non equilibrio una nuova fase emerge quale manifestazione di una risonanza parametrica a molti corpi. Questa risonanza parametrica è in essenza identica a quella descritta sopra. In questa tesi forniamo uno studio esatto di questo sistema, sotto forzatura e dissipazione, e caratterizziamo le transizioni di fase presenti nel suo diagramma di fase.

L'ultima parte della tesi studia modelli sperimentalmente realistici per la realizzazione della risonanza parametrica a molti corpi osservata nel modello di Dicke. La realizzazione sperimentale della transizione di fase superradiante di Dicke, predetta molti anni orsono, è molto complessa in quanto richiede un accoppiamento tra la materia e la luce relativamente forte. Questa transizione di fase è stata osservata solo recentemente in un condensato di Bose-Einstein accoppiato ad una cavità ottica. In questo sistema è possibile regolare l'intensità di accoppiamento tra gli atomi e il campo della cavità modificando l'intensità di un laser esterno che irradia il sistema. La facile controllabilità di questo apparato sperimentale lo rende il candidato ideale per la realizzazione del modello di Dicke modulato periodicamente e per verificare l'emergenza del fenomeno di risonanza parametrica a molti corpi.

L'ultimo progetto di questa tesi riguarda infatti lo studio di un gas di Bose, formato da particelle interagenti, accoppiato ad una cavità e soggetto ad una modulazione dell'intensità del laser sopra citato. Dato che l'esame di questo sistema comporta lo studio di un problema quantistico a molti corpi con dipendenza dal tempo, ricorriamo a metodi numerici e sfruttiamo, in particolare, la capacità del "Multi-Configurational Time-Dependent Hartree method for indistinguishable particles" (MCTDH-X) di indagare le dinamiche del sistema. In questo sistema la risonanza parametrica da origine ad una fase non presente nello scenario statico, in cui il condensato oscilla tra diverse configurazioni reticolari e presenta caratteristiche di riscaldamento peculiari.

Contents

I Introduction

The secret of getting ahead is getting started.

Mark Twain

THIS brief preface provides a broad overview of the topics that we will encounter in this thesis. Here, we limit ourselves to a rather short and preparatory introduction to the different subjects. However, we will provide a more exhaustive discussion at the beginning of every chapter. After getting familiar with the basic notions that will be used throughout this work, we will provide a sketch of the contents of the individual chapters.

I.1 Brief review

I.1.1 The harmonic oscillator

The harmonic oscillator is perhaps one of the easiest and widely used models in physics. In its most common incarnation, which is the *classical* harmonic oscillator, it describes the simple physics of a mass connected to a spring [1]. In the quantum world, if we consider the one-dimensional motion of a particle in a quadratic potential, then what we obtain is nothing but the *quantum* harmonic oscillator. We will refer from now on to *the* harmonic oscillator, but the context will clarify its classical or quantum nature.

The importance of this model goes way beyond its adequacy for first year lectures; it is rather due to its versatility. Several complex systems can indeed by analyzed in terms of normal modes, which behave like simple harmonic oscillators. Sidney Coleman once said:

> *The career of a young theoretical physicist consists of treating the harmonic oscillator in ever-increasing levels of abstraction.*

Of course, this is a little exaggerated, but it surely contains a good amount of truth. The harmonic oscillator provided the ground for the understanding of a huge number of phenomena appearing in nature. The quantum mechanical description of the electromagnetic field is an emblematic example. At a quantum level it is an infinite collection of harmonic oscillators, whose excitation quanta are the photons [2]. Further, in condensed matter the quantum mechanical understanding of lattice vibrations, whose elementary vibrational modes are the phonons, is again provided by the physics of harmonic oscillators [3]. This result is anything but irrelevant, as phonons play a very significant role in solid state physics and explain properties such as the thermal and electrical conductivity of materials and provide a key mechanism for the description of conventional superconductors [4].

Coleman's quote captures the spirit of the present thesis rather well. In this work we will deal, under different circumstances, with classical as well as quantum oscillators.

I.1.2 Parametric resonance

Another classic example of a harmonic oscillator is the pendulum, which consists of a mass suspended from a pivot and performing small oscillations around the equilibrium position. A more engaging case, which we all know from personal experience, is represented by a child on a swing. What the child can do in order to increase its swinging amplitude is to lower and raise his legs (that is, his center of gravity) periodically in time. Some attempts will eventually teach him that the best strategy is to do it at twice the frequency of the swing. This is a prototypical example of parametrically driven system and the large increase in amplitude due to the frequency match just described is an example of *parametric resonance* [1]. In general, a system is said *parametrically driven* if one, or more, of its parameters is varied periodically in time and the phenomenon of

parametric resonance can also occur at frequencies other than the one just discussed.

Probably, the earliest demonstration of this kind of resonance dates back to Faraday in the early 1800s [5]. He experimentally observed peculiar wave structures on fluid surfaces on periodically shaking the tank containing the fluid at *twice* the frequency of the surface vibrations. After the pioneering works of Floquet [6] and Hill [7] in the late 1800s, it was understood that parametric resonance emerges also for frequencies other than that identified by Faraday.

The understanding of parametric driving – nowadays also known as *Floquet* driving – and parametric resonance resulted in a very broad scientific development. A field that greatly profited from this advances is the one of microelectromechanical and nanoelectromechanical systems (MEMS and NEMS), where higher mechanical amplification, thermomechanical noise squeezing and enhanced sensitivity have been obtained [8, 9]. Subsequently, a great effort has been made to explore the phenomenon of parametric resonance in the quantum domain. An acclaimed product of these attempts is the quantum mechanical description of the quadrupole ion trap [10], which was awarded the Nobel Prize in Physics in the 1989.

I.1.3 Nonlinear systems

While for many situations the simple picture of the (linear) harmonic oscillator described above is sufficient to accurately describe a given phenomenon, for some systems it is necessary to resort to more complex models. In the previous example of the child on a swing, when the amplitude of his oscillations becomes large enough nonlinearities come into play and the motion can change in a qualitative way [1]. The phenomenon of resonance acquires indeed very nontrivial properties when external forces and/or parametric driving act on nonlinear systems [1, 11]. Nonlinear dynamical systems host indeed new fascinating phenomena, such as multistability, bifurcations concepts, chaotic dynamics and catastrophe theory, which go beyond the paradigms of linear systems [12]. Particularly important for the purpose of this thesis is the concept of bifurcation, which describes the significant qualitative change, or topological change, in its behavior caused be an infinitesimal smooth change in a key parameter of the system.

The effect of nonlinearities becomes particularly important as oscil-

lators scale down [13] and strongly affects the dynamical behavior of systems such as MEMS and NEMS, which are usually employed for mass and force detection purposes. In recent times it was realized that nonlinearities – previously avoided, restricting the resonators to work in the linear regime of small oscillations – could be turned into an advantage [14, 15]. Inspired by the capabilities of MEMS and NEMS to implement parametric driving, as well as the natural occurrence of nonlinearities, in this thesis we study a parametrically driven nonlinear oscillator in the presence of an external periodic force. Combining the effects of nonlinearities and parametric driving, we brought to light a new way to accurately measure weak forces. We provided the theoretical framework behind this new paradigm for sensitive force detection and contributed to its experimental demonstration.

I.1.4 Light-matter systems

What happens when light meets matter? In this thesis, we will consider the quantum-mechanical interaction between light and matter. The field of physics that deals with this interaction at a quantum level is the cavity quantum electrodynamics (QED) [16, 17]. The easiest nontrivial realization, known as the Jaynes-Cummings (JC) model [18, 19], consists of a single two-level system interacting with a single quantized mode of the electromagnetic field. A major achievement of cavity QED lies in the fact that a single photon can be absorbed and re-emitted by the two-level atom several times before leaving the cavity. This phenomenon, known as quantum Rabi oscillations, is fundamentally different from the spontaneous emission observed in free space. The said regime of coherent light-matter interaction is known in the literature as the strong coupling regime (SCR) [16, 17]. Even though the idea is quite simple, experimentally probing the SCR for a single two-level system in a single-mode cavity is exceptionally challenging and has only been realized recently.

In the standard treatment of light-matter systems, the latter is considered as an ensemble of two-level atoms and are confined between cavity mirrors. This two-level assumption can be justified a posteriori, or experimentally. One can indeed choose the frequency of the quantized cavity mode to be (near) resonant with an atomic transition, in such a way that the other atomic states can be neglected [17]. The system described here, which considers the interaction between a single quantized field mode and the collection of many noninteracting two-level systems

is known as the Dicke model [20] and is a leading example of system exhibiting light-matter collective behavior. In such a scenario the atomic ensemble absorbs and emits photons collectively, leading to strong correlations in the atomic ensemble. When the interaction strength between the atoms and the light mode exceeds a critical value, the system undergoes a ($\mathbb{Z}_2$) symmetry breaking quantum phase transition from a normal phase to a superradiant phase. While the former is characterized by all the atoms being in their ground state and the cavity being empty, in the latter the ground state of the overall system is surprisingly distinguished by a macroscopic population of the excited atomic levels as well as the cavity mode. Recently, it was shown that parametric resonance leads to the emergence of a novel nonequilibrium phase in the periodically driven Dicke model [21]. The rich out-of-equilibrium phase diagram of this model is distinguished by three phases of matter and in this thesis we will discuss it in great detail.

Nowadays, due to colossal technological steps forwards it is possible to load Bose-Einstein condensates into optical cavities and lattices, which can then be used as quantum simulators. The well-known Bose-Hubbard model, which undergoes a quantum phase transition from a superfluid to a Mott insulating phase, was indeed realized in one of these systems [22]. Light-matter systems allow to engineer an unprecedented range of physical models, among which periodically driven quantum many-body systems. In most cases, the introduction of periodic driving is achieved by modulating the strength of laser fields. Time dependent quantum many-body systems are particularly intriguing as they offer the possibility of studying the dynamics of systems out of equilibrium [23–26]. In recent times, they have shown an enormous diversity of new phenomena in several fields, with no counterparts in equilibrium systems. Striking examples of such results are the coherent destruction of tunneling [27, 28], in which quantum tunneling can be completely suppressed in a dynamically coherent way; dynamical localization [29–31], which has a close relation with the well-known Anderson localization [32] and superfluid-insulator transitions in driven optical lattices [33], in which a quantum phase transition between superfluid and Mott insulator is induced by an oscillating force. Parametric driving also opened the door to Floquet topological insulators [34], in which a non-equilibrium topological state can be induced by periodically driving a system initially in a topologically trivial phase, and to the detections of

the Majorana Fermions [35, 36].

I.1.5 Beyond toy models

More relevant to this thesis is instead the experimental realization of the Dicke model in a cavity-BEC system [20, 37]. In this experiment, an effective Dicke model is realized in which the interaction between light and matter can be tuned by changing the amplitude of a pump laser. This fact makes the system used in Ref. [20, 37] an ideal candidate for the actualization of the modulated Dicke model outlined above (see Sec. I.1.2), and for the study of its nonequilibrium phase diagram. The physics manifested by realistic systems under periodic drive is expected to be very rich as interatomic interactions, neglected in the Dicke (toy) model, are indeed present in the cold atom experiment. A crucial question for the long-time behavior of interacting many-body system is the one of heating. The present common belief is that closed, interacting many-body systems subject to periodic driving will absorb energy from the driving field and end up in an infinite-temperature thermal state [38, 39].

In the present thesis, we use parameter values close to the ones of the original experiment [37] to numerically simulate the dynamics of an interacting Bose-Einstein condensate inside an optical cavity under the condition of parametric driving. We investigate the nonequilibrium phase diagram of the periodically driven cavity-BEC system and observe very intriguing heating characteristics.

I.2 Outline and Contributions of this Thesis

This thesis covers all the fields presented above; in each chapter one or more of them simultaneously could be the actor on stage. Broadly speaking, it deals with the phenomenon of parametric resonance in (nonlinear) classical and quantum systems. Even though all the chapters share the same main theme, the thesis is conceptually divided into *two* parts. The first part, constituted by Chapter II, is classical, while the second one, comprising Chapters III and IV, is quantum. In the present section we provide a short summary of the different chapters and describe how they are connected.

The first contribution [40], presented in Chapter II, deals with the problem of accurate detection of small forces. Contrarily to standard

resonator-based sensors, which are confined to their linear range, we deliberately combined nonlinearities and parametric driving and came up with a new paradigm. We found that a nonlinear resonator, when parametrically driven with the *right* strength and at the *right* frequency, displays a very characteristic response which can be exploited for force detection purposes.

The second contribution [41], also presented in Chapter II and carried out in collaboration with Anina Leuch, Alexander Eichler and Christian Degen, reports the first experimental observation of the predicted nonlinear phenomena. It is in this work that we coined the term *parametric symmetry breaking*, which is referred to the fact that a periodic external force can lift the amplitude degeneracy between the parametric phase states.

The third project [42], contained in Chapter III, takes inspiration from the pioneering work of R. Chitra and O. Zilberberg [21], in which the impact of parametric driving on the phase diagram of the dissipative Dicke model (DM) was analyzed. In the static case this model is known to host the well-known superradiant phase transition from a normal phase (NP) to a superradiant phase (SP). Surprisingly, parametric driving leads to a novel dynamical normal phase (D-NP), extending the phase diagram to three phases. In this chapter we study in great detail the driven NP with particular attention on its transition to the D-NP. We found that in the absence of dissipation the entanglement between the cavity field and the atoms shows a bounded oscillatory behavior, whose precise form strongly depends on the strength and frequency of the parametric modulation. The maximal values of entanglement are reached close to the D-NP phase boundary. However, upon hitting the instability boundary the entanglement behavior undergoes a qualitative change from bounded and oscillatory to unbounded and monotonously increasing. Dissipation has a drastic impact on the system: it only allows the system to sustain entanglement in the transient dynamics, but always kills it after a finite time. Upon approaching the D-NP phase the entanglement lifetime is prolonged and approaches a steady-state finite value on the phase boundary. Moreover, we found that in the nonequilibrium setting provided by the parametric drive, the criticality of the NP-SP transition can be continuously modified across the phase boundary.

In recent years the long-sought Hepp-Lieb superradiant phase transition in the Dicke model has been realized in a Bose-Einstein conden-

sate (BEC) coupled to an optical cavity [37, 43, 44]. This fact, together with the rich physics exhibited by the modulated DM, brought us to the fourth and last project [45] realized in collaboration with Axel Lode. In Chapter IV we study the dynamics of a BEC coupled to an optical cavity, where the light-matter coupling is parametrically modulated. We found that, apart from a normal and superradiant phase, a third nonequilibrium phase emerges as a many-body parametric resonance. This dynamical phase switches between two symmetry-broken superradiant configurations. Unlike the other two phases, the emergent phase shows features of nonintegrability and thermalization.

I.3 Averaging method

An important tool that we will extensively use in the first half of the thesis is the *averaging method* (AM). Its origin dates back to the works of Lagrange and Laplace in the late 1700s on celestial mechanics. However, it is only after the important contributions of Krylov, Bogoliubov and Mitropolsky that the method has solid foundations [46, 47]. In the late 1900s, after rigorous proofs of the validity of averaging both in the periodic and the general case [48–50], it became a well-established method in the investigation of nonlinear systems.

As an introduction, we start in a rather informal way by looking at a concrete example (see [11]). This will help us to develop an intuitive picture of the method. Afterwards, we will give the statement of the *Averaging Theorem* and develop a more rigorous theory of the AM up to second order.

I.3.1 Basic idea

Consider the *Van der Pol* equation

$$\ddot{x} + x = \varepsilon f(x, \dot{x}), \qquad 0 < \varepsilon \ll 1, \tag{I.1}$$

where f is a T-periodic function and ε a small positive parameter. For $\varepsilon = 0$ we recover the well-know equation of a harmonic oscillator (HO), whose solution is given by

$$x(t) = r_0 \cos(t + \beta_0),$$

with r_0 and β_0 constants fixed by the initial conditions. For sufficiently small values of ε a solution of the same form is expected to be valid, but with slowly varying coefficients r and β

$$x(t) = r(t)\cos\left(t + \beta(t)\right). \tag{I.2}$$

We further fix the remaining degree of freedom by imposing [46]

$$\dot{x}(t) = -r(t)\sin(t + \beta(t)), \tag{I.3}$$

as for the unperturbed case. In order to determine $r(t)$ and $\beta(t)$ we start by differentiating Eq. (I.2) and comparing the result to Eq. (I.3) which leads to the condition

$$\dot{r}\cos(t+\beta) - r\dot{\beta}\sin(t+\beta) = 0.$$

We dropped here the time dependence of r and β for readability. Then, differentiating Eq. (I.3) and substituting the result into Eq. (I.1) gives

$$-\dot{r}\sin(t+\beta) - r\dot{\beta}\cos(t+\beta) = \varepsilon f\big(r\cos(t+\beta), -r\sin(t+\beta)\big). \tag{I.4}$$

Solving the last two equations with respect to $\dot{r}$ and $\dot{\beta}$ leads to

$$\dot{r} = -\varepsilon\sin(t+\beta) f\big(r\cos(t+\beta), -r\sin(t+\beta)\big), \tag{I.5}$$

$$\dot{\beta} = -\frac{\varepsilon}{r}\cos(t+\beta) f\big(r\cos(t+\beta), -r\sin(t+\beta)\big). \tag{I.6}$$

So far the treatment has been exact. The only thing we did is to replace the original second-order differential equation [cf. Eq. (I.1)] by two first-order differential equations [cf. Eqs. (I.5) and (I.6)]. The key point is to realize that, being the right-hand side of these two equation periodic in $t+\beta$, both $\dot{r}$ and $\dot{\beta}$ are of order $\mathcal{O}(\varepsilon)$. This means that r and β are slowly varying during the time $T = 2\pi$ compared to the terms appearing on the right-hand side of Eqs. (I.5) and (I.6). The approximation consists therefore in averaging the last two equations by keeping r and β constant. The resulting *slow flow* equations for $\bar{r}$ and $\bar{\beta}$, which determine the evolution of the amplitude and phase on a slow time scale (εt), are given by

$$\dot{\bar{r}} = -\frac{\varepsilon}{2\pi}\int_0^{2\pi} \sin\varphi\, f(\bar{r}\cos\varphi, -\bar{r}\sin\varphi)\mathrm{d}\varphi, \tag{I.7}$$

$$\dot{\bar{\beta}} = -\frac{\varepsilon}{2\pi\bar{r}}\int_0^{2\pi} \cos\varphi\, f(\bar{r}\cos\varphi, -\bar{r}\sin\varphi)\mathrm{d}\varphi, \tag{I.8}$$

where we have introduced $\varphi \equiv t + \bar{\beta}$. The main idea behind the method, as can be seen from the Eqs. (I.7) and (I.8), is to approximate the original complex system by an easier autonomous averaged system.

The short summary we gave in the last lines above essentially anticipates the statement of the Averaging Theorem. Consider a differential equation in the *standard form*

$$\dot{\mathbf{x}} = \varepsilon \mathbf{f}(\mathbf{x}, t), \qquad 0 < \varepsilon \ll 1, \tag{I.9}$$

where $\mathbf{x}$ and $\mathbf{f}(\mathbf{x}, t)$ are vectors in $\mathbb{R}^n$. We further consider $\mathbf{f}(\mathbf{x}, t)$ to be a T-periodic function in t. The basic result is that the solution of the original system (I.9) and the one of the following *averaged system*

$$\dot{\mathbf{z}} = \varepsilon \bar{\mathbf{f}}(\mathbf{z}), \tag{I.10}$$

with

$$\bar{\mathbf{f}}(\mathbf{z}) = \frac{1}{T} \int_0^T \mathbf{f}(\mathbf{z}, t) \mathrm{d}t, \tag{I.11}$$

remain close, i.e. $\|\mathbf{x}(t) - \mathbf{z}(t)\| = \mathcal{O}(\varepsilon)$, on a time scale $t \sim 1/\varepsilon$. Additional details or proofs of this statement can be found in the abounding literature on the subject [46, 47, 51, 52] and references therein.

I.3.2 Formal theory of averaging

So far we have described the averaging procedure for the specific case of the Van der Pol equation. However, the lack of generality and rigorousness makes it hard to apply it to other kinds of equations. The crucial question of how to extend it to higher orders remains unanswered. Even though the methodology of averaging has been elegantly generalized to arbitrary order using *Lie series* [52–54], we limit ourselves to present an easier and more transparent derivation using *near-identity transformations* (NITs), up to second order, following Holmes and Holmes [55].

To start with, we can still profit from the previous example to outline the basic idea behind the method in its most general form. The only thing we need is a change of the point of view. Fundamentally, the method is related to the existence of a change of variables which eliminates the time t from the equations [47]. We can interpret the Eqs. (I.2)

and (I.3) as a transformation from x, $\dot{x}$ to r, β. Crucially, instead of integrating Eqs. (I.5) and (I.6), we introduce a NIT of the form

$$r = \bar{r} + \varepsilon w_1(\bar{r}, \bar{\beta}, t) + \mathcal{O}(\varepsilon^2), \tag{I.12}$$

$$\beta = \bar{\beta} + \varepsilon w_2(\bar{r}, \bar{\beta}, t) + \mathcal{O}(\varepsilon^2). \tag{I.13}$$

The two functions w_1 and w_2 are called the *generating functions* of the NIT. The corresponding equations for $\bar{r}$ and $\bar{\beta}$, obtained by inserting the Eqs. (I.12) and (I.13) into Eqs. (I.5) and (I.6), have exactly the same form of the latter ones except for the additional terms $-\varepsilon\,\partial_t w_1$ and $-\varepsilon\,\partial_t w_2$, respectively. The two generators w_1 and w_2 are chosen in order to eliminate all the $\mathcal{O}(\varepsilon)$ terms, except for their averaged value[1]. This procedure gives the same result we have obtained in Eqs. (I.7) and (I.8). The additional work we have done, however, is far from being useless. We have now a scheme at hand that allows us to extend the averaging procedure to any order.

We are now in a good position to discuss the general scheme. Consider the nonautonomous system

$$\dot{\mathbf{x}} = \varepsilon \mathbf{f}(\mathbf{x}, t, \varepsilon), \qquad 0 < \varepsilon \ll 1, \tag{I.14}$$

which is obtained by a slight extension of Eq. (I.9). As we just discussed, the transition from the initial differential equation (I.14) to the averaged system relies on the existence of a NIT. Similarly to Eqs. (I.12) and (I.13) we set here

$$\mathbf{x} = \mathbf{y} + \varepsilon \mathbf{w}_1(\mathbf{y}, t), \tag{I.15}$$

where $\mathbf{w}_1$ is not known yet. Upon insertion of this transformation into Eq. (I.14) we obtain

$$\big[\mathbb{I} + \varepsilon D_{\mathbf{y}} \mathbf{w}_1\big]\dot{\mathbf{y}} = \varepsilon\big[\mathbf{f}(\mathbf{y} + \varepsilon \mathbf{w}_1, t, \varepsilon) - \partial_t \mathbf{w}_1\big],$$

where $\mathbb{I}$ denotes the identity matrix and $D_{\mathbf{y}}\mathbf{w}_1$ is the Jacobian matrix $\partial(w_{1,1}, \cdots, w_{1,n})/\partial(y_1, \cdots, y_n)$. Inverting the near-identity operator on the left-hand side[2], $\mathbb{I} + \varepsilon D_{\mathbf{y}}\mathbf{w}_1$, and expanding the right-hand side in a Taylor series about $\mathbf{y}$ gives

$$\dot{\mathbf{y}} = \varepsilon\big[\mathbf{f}(\mathbf{y}, t, 0) - \partial_t \mathbf{w_1}\big] + \mathcal{O}(\varepsilon^2). \tag{I.16}$$

[1] Note that they are *not* simply chosen in order to eliminate all the $\mathcal{O}(\varepsilon)$ terms. This choice leads to divergent generating functions and thus to a violation of the uniform validity of the NIT [cf. Eqs (I.12) and (I.13)].

[2] It is invertible because it is close to the identity.

We now split the function $\mathbf{f}$ into its mean, denoted by $\bar{\mathbf{f}}(\mathbf{y})$ [cf. Eq. (I.11)], and an oscillating part with zero mean, denoted by $\tilde{\mathbf{f}}(\mathbf{y},t)$, that is $\mathbf{f}(\mathbf{y},t) = \bar{\mathbf{f}}(\mathbf{y}) + \tilde{\mathbf{f}}(\mathbf{y},t)$. As anticipated above, we choose $\mathbf{w}_1$ such that $\partial_t \mathbf{w}_1 = \tilde{\mathbf{f}}(\mathbf{y},t)$ is satisfied[3]. This gives the known result

$$\dot{\mathbf{y}} = \varepsilon \bar{\mathbf{f}}(\mathbf{y}) + \mathcal{O}(\varepsilon^2) \tag{I.17}$$

for first order averaging [cf. Eqs. (I.7), (I.8) and (I.10)].

The advantage of working with NITs is that we can easily extend the procedure to second order. This is achieved by extending the transformation (I.15) as

$$\mathbf{x} = \mathbf{y} + \varepsilon \mathbf{w}_1(\mathbf{y},t) + \varepsilon^2 \mathbf{w}_2(\mathbf{y},t).$$

After performing the same steps as we did for the first order case, Eq. (I.16) is extended to

$$\dot{\mathbf{y}} = \varepsilon \big[\mathbf{f}(\mathbf{y},t,0) - \partial_t \mathbf{w}_1\big] + \varepsilon^2 \big[\mathbf{g}(\mathbf{y},t) - \partial_t \mathbf{w}_2\big] + \mathcal{O}(\varepsilon^3), \tag{I.18}$$

where we have defined $\mathbf{g}(\mathbf{y},\mathbf{t})$ as

$$\mathbf{g}(\mathbf{y},\mathbf{t}) = D_{\mathbf{y}}\mathbf{w}_1\big(\partial_t \mathbf{w}_1 - \mathbf{f}(\mathbf{y},t,0)\big) + D_{\mathbf{y}}\mathbf{f}(\mathbf{y},t,0)\mathbf{w}_1 + \partial_\varepsilon \mathbf{f}(\mathbf{y},t,0). \tag{I.19}$$

We choose $\mathbf{w}_1$ as before. This fixes the $\mathcal{O}(\varepsilon)$ term in Eq. (I.18) as well as the first term on the right-hand side in Eq. (I.19). We split the function $\mathbf{g}$ into its mean, $\bar{\mathbf{g}}(\mathbf{y})$, and an oscillating part, $\tilde{\mathbf{g}}(\mathbf{y},t)$, and use the same splitting for $\mathbf{f}$ in order to rewrite the second term on the right-hand side in Eq. (I.19) as $D_{\mathbf{y}}\bar{\mathbf{f}}(\mathbf{y})\mathbf{w}_1 + D_{\mathbf{y}}\tilde{\mathbf{f}}(\mathbf{y},t)\mathbf{w}_1$. The only terms of non-zero mean, at $\mathcal{O}(\varepsilon^2)$, are $D_{\mathbf{y}}\tilde{\mathbf{f}}(\mathbf{y},t)\mathbf{w}_1$ and the last one in Eq. (I.19). For this reason, as opposed to $\bar{\mathbf{f}}(\mathbf{y})$, which is given by Eq. (I.11), the mean component $\bar{\mathbf{g}}(\mathbf{y})$ is given by

$$\bar{\mathbf{g}}(\mathbf{y}) = \frac{1}{T}\int_0^T \big[\partial_\varepsilon \mathbf{f}(\mathbf{y},t,0) + D_{\mathbf{y}}\tilde{\mathbf{f}}(\mathbf{y},t)\mathbf{w}_1\big]\,\mathrm{d}t.$$

Choosing $\mathbf{w}_2$ such that $\partial_t \mathbf{w}_2 = \tilde{\mathbf{g}}(\mathbf{y},t)$ leads us to the second order averaged system

$$\dot{\mathbf{y}} = \varepsilon \bar{\mathbf{f}}(\mathbf{y}) + \varepsilon^2 \bar{\mathbf{g}}(\mathbf{y}) + \mathcal{O}(\varepsilon^3). \tag{I.20}$$

There are cases in which the system (I.17) is degenerate and first order averaging does not provide a satisfactory description of the true system [Eq. (I.14)]. The last Eq. (I.20) is therefore of great importance for those systems in which crucial informations only enter at second order [55]. We will see in Sec. II.7 and II.8 two cases for which this is necessary.

[3] The integration constant is chosen such that $\mathbf{w}_1$ has zero mean.

I.4 MCTDH-X

The multiconfigurational time-dependent Hartree method for indistinguishable particles (MCTDH-F for fermions and MCTDH-B for bosons; in short MCTDH-X) is an efficient variational method for the simulation of the quantum dynamics of interacting ultracold atoms [56, 57]. The method does not rely on finding a simpler effective Hamiltonian, rather on finding an approximation for the state of the system Ψ for the full many-body Hamiltonian. Being a variational method, the ansatz for the wave-function crucially determines the accuracy and generality of the method. As opposed to the Gross-Pitaevskii theory, which is a mean-field theory, the MCTDH-X is based on a more general multiconfigurational ansatz that captures the transition from condensation to fragmentation. By construction, this is clearly not accessible by a mean-field theory. We briefly outline here the basic idea behind the numerical method.

Consider the time-dependent many-body Schrödinger equation for N structureless bosons:

$$\hat{\mathcal{H}}\Psi = i\partial_t\Psi. \tag{I.21}$$

The Hamiltonian is given by

$$\hat{\mathcal{H}}(\mathbf{r}_1,\ldots,\mathbf{r}_N,t) = \sum_{i=1}^{N}\hat{h}(\mathbf{r}_i,t) + \sum_{i<j}^{N}\hat{W}(\mathbf{r}_i-\mathbf{r}_j,t), \tag{I.22}$$

where $\hat{h}(\mathbf{r},t) = \hat{T}(\mathbf{r}) + \hat{V}(\mathbf{r},t)$ is the one-body Hamiltonian containing the kinetic ($\hat{T}$) and potential ($\hat{V}$) energy terms and $\hat{W}(\mathbf{r}_i-\mathbf{r}_j,t)$ is the two-body interparticle interaction between the i-th and j-th boson. Obviously, in general the many-body Schrödinger equation (I.21) is *not* analytically solvable and one has to resort to numerical methods.

The present method is based on the following ansatz for the many-body wave function

$$|\Psi(t)\rangle = \sum_{\mathbf{n}} C_{\mathbf{n}}(t)|\mathbf{n},t\rangle\,. \tag{I.23}$$

$|\Psi(t)\rangle$ is written in the basis of symmetrized states (permanents) $|\mathbf{n},t\rangle$, which consist of products of N particles in M single-particle functions (orbitals) $\Phi_i(\mathbf{r},t)$, with $i = 1,...,M$. The sum in Eq. (I.23) runs over all configurations $\mathbf{n} = (n_1,\ldots,n_M)$ such that $\sum_{i=1}^{M} n_i = N$. The number of orbitals, M, can be chosen at will and in the limit of $M \to \infty$ the

expansion in Eq. (I.23) becomes exact. The approximation introduced here consists hence in the assumption that a set of M orbitals provides a sufficient description of the full Hilbert space of the N-particle wave function. Note that both the weights $C_{\mathbf{n}}(t)$ and the permanents $|\mathbf{n},t\rangle$ are explicitly time dependent. We can express the configurations $|\mathbf{n},t\rangle$ as

$$|\mathbf{n},t\rangle = \prod_{i=1}^{M}\left[\frac{\left(\hat{b}_i^\dagger(t)\right)^{n_i}}{\sqrt{n_i!}}\right]|\mathrm{vac}\rangle\,, \tag{I.24}$$

where the operator $\hat{b}_i^\dagger(t)$ creates a boson in the i-th single-particle state $\Phi_i(\mathbf{r},t)$ and $|\mathrm{vac}\rangle$ is the vacuum.

The MCTDH-X equations of motion (EOM) are derived employing the time-dependent variational principle [58]. The actual time evolution of the many-body system is the one that minimizes the action functional[4], denoted by $\mathcal{S}$. Both the expansion coefficients $\{C_{\mathbf{n}}(t)\}$ as well as the orbitals $\{\Phi_k(\mathbf{r},t)\}$ are independent parameters. One thus require stationarity of the action $\mathcal{S}[\{C_{\mathbf{n}}(t)\},\{\Phi_k(\mathbf{r},t)\}]$ with respect to both sets of arguments. The variation of the action with respect to the expansion coefficients gives the following EOM

$$i\partial_t\boldsymbol{\mathcal{C}}(t) = \boldsymbol{\mathcal{H}}(t)\boldsymbol{\mathcal{C}}(t), \tag{I.25}$$

where all the coefficients $\{C_{\mathbf{n}}(t)\}$ are collected into the vector $\boldsymbol{\mathcal{C}}(t)$ and $\mathcal{H}_{\mathbf{n},\mathbf{n}'} = \langle\mathbf{n},t|\hat{\mathcal{H}}|\mathbf{n}',t\rangle$ is the Hamiltonian represented in the chosen many-body basis. On the other hand, the variation of the action with respect to the orbitals leads to

$$i\partial_t|\Phi_j\rangle = \hat{P}\left[\hat{h}|\Phi_j\rangle + \sum_{k,s,q,l=1}^{M}\{\boldsymbol{\rho}\}^{-1}_{jk}\rho_{ksql}\hat{W}_{sl}|\Phi_q\rangle\right], \tag{I.26}$$

where $\rho_{kq} = \langle\Psi|\hat{b}_k^\dagger\hat{b}_q|\Psi\rangle$ and $\rho_{ksql} = \langle\Psi|\hat{b}_k^\dagger\hat{b}_s^\dagger\hat{b}_q\hat{b}_l|\Psi\rangle$ are the matrix elements of the reduced one-body and two-body density matrix. The one-body Hamiltonian, denoted by $\hat{h}$, follows Eq. (I.22) and $\hat{W}_{sl}(\mathbf{r}) = \int d\mathbf{r}'\Phi_s^*(\mathbf{r}',t)\hat{W}(\mathbf{r}-\mathbf{r}',t)\Phi_l(\mathbf{r}',t)$ are local time-dependent interaction potentials, in which $\hat{W}(\mathbf{r}-\mathbf{r}',t)$ is the two-body interparticle interaction. Lastly, $\hat{P}$ is a projection operator onto the subspace orthogonal to that

[4]The *action* or *action functional* $\mathcal{S}$ is the integral over time of the Lagrangian and is described in terms of so-called generalized coordinates.

spanned by the orbitals $\{\Phi_i(\mathbf{r},t)\}$. The coupled set of equations (I.25) and (I.26) are the core of the MCTDH-X method. For further details on the derivation of these equations, see Refs. [56, 57].

For the sake of later conveniency, we consider the common contact interparticle interaction $\hat{W}(\mathbf{r}-\mathbf{r}') = \lambda_0\delta(\mathbf{r}-\mathbf{r}')$, see e.g. Ref. [59]. With this choice of two-body interaction, characterized by the interaction strength λ_0, Eq. (I.26) for the time evolution of the orbitals becomes

$$i\partial_t|\Phi_j\rangle = \hat{P}\left[\hat{h}|\Phi_j\rangle + \lambda_0 \sum_{k,s,q,l=1}^{M} \{\boldsymbol{\rho}\}^{-1}_{jk}\rho_{ksql}\Phi^*_s\Phi_l|\Phi_q\rangle\right]. \tag{I.27}$$

This is the equation that we will solve numerically in Sec. IV, together with Eq. (I.25) for the coefficients, in order to investigate the time evolution of a weakly-interacting Bose-Einstein condensate. As a comparison with other standard techniques, we remark that the method here presented reduces to the well-known time-dependent Gross-Pitaevskii equation [59, 60] for $M = 1$ orbitals.

II

Nonlinear parametric oscillators

To speak of non-linear physics is like calling zoology the study of non-elephant animals.

Stanislaw Ulam

RESEARCH on nonlinear resonators started over a century ago, motivated by observations in electrodynamics and mechanics [11]. The fact that novel features are still discovered in nonlinear resonators today bears witness to their great complexity and variety. Nonlinear resonators manifest themselves in many modern fields of physics, e.g. quantum electrical circuits, cold atoms, levitated nanoparticles, microelectromechanical and nanoelectromechanical systems (MEMS and NEMS) [61]. They are intimately related to state-of-the-art metrology platforms used for measurements of weak external forces corresponding to single charges, spins, or mass on the atomic scale [62–65].

Interestingly, many of these modern resonators allow the study of individual modes whose nonlinearities can be tailored or tuned in situ and on which theoretical concepts, both classical and quantum, can be tested [66, 67]. One such concept is parametric resonance, where the frequency of the linear oscillator is modulated in time [1, 8, 68, 69]. The parametrically driven oscillator boasts a fascinating stability diagram called "Arnold's tongues" delineating zones where the oscillator is stable from those where it is exponentially unstable, as a function of its natural frequency and parametric driving strength [70]. In the stable regime, parametric resonance can be used to amplify signals and

squeeze noise [8, 71, 72], design mechanical logic circuits [73], or generate quantum entanglement [74, 75]. In the unstable regime, the resonator is driven to a large and stable response, which can be used for mechanical information storage [76] or signal amplification through bifurcation topology [15].

Nonlinearities become important as resonators scale down [13]. This can be attributed to geometric effects, external potentials, dissipation, or even feedback cooling used to control the resonator. Nonlinear effects strongly restrict the dynamic range within which the system operates linearly, even making it vanishingly small in NEMS, and limit the scope for applications. However, recent works focus on directly using nonlinearities to improve the sensitivity of parametrically amplified detectors [14, 15, 77]. For instance, though quartic (Duffing) nonlinearities stabilize the parametric oscillator (PO), it retains a "memory" of the underlying instability tongue structure in its frequency dependent response [78]. The precision measurement of this lobe [77, 78] then provides a very robust and stable way of detecting masses [77]. Still, the utility of nonlinearities in POs for sensing of external forces remains relatively unexplored.

In this chapter we obtain the solution for the response of an externally driven nonlinear parametric resonator *below* and *beyond* the instability threshold. The response features an unexpected double hysteresis whose position depends sensitively and linearly on the amplitude of the applied external force. Using recent experiments as examples, we predict how the double hysteresis should manifest, and we propose a method to use it for the detection of weak forces. Importantly, the force sensor we propose has a linear dependency of signal on measured force even though it is based on a nonlinear mechanical resonator.

The chapter is structured as follows. In Sec. II.1, we provide a brief, and surely non-exhaustive, review about linear POs. Several concepts that will be of key importance in the proceeding of the chapter are here presented. In Sec. II.2, we detail the model describing a general nonlinear PO. Section II.3 is dedicated to the application of the perturbative AM used for the analysis of the model and to obtain a closed equation for the steady-state positional response. Based on our results for the response, we present our method for hysteretic force detection in Sec. II.4 and we discuss the application of our force detection scheme to different experimental systems in Sec. II.5. In Sec. II.6 we show that the peculiar

double-hysteretic response of our system is intimately linked to a symmetry breaking between the phase states of the unforced oscillator. In Sec. II.7 we consider the possibility of observing the same behavior by driving the system around instability lobes other than the first one and, subsequently, we discuss in Sec. II.8 the effect of other nonlinear terms. To conclude, we provide in Sec. II.9 a final perspective of possible observations and applications of the hitherto described physics.

The contents of this chapter are largely included in References [40] and [41].

II.1 Linear parametric oscillators

Much of the physical world around us can be described in terms of harmonic oscillators. At the same time, parametric excitation of resonators and parametric resonance spontaneously occur in Nature and play an important role in many areas of science and technology. The idea behind parametric driving can be simply stated as the possibility of increasing the energy of an oscillating system *even when* the frequency of a weak excitation is far from the natural frequency of the system. This differs greatly from the case of an external driving, for which a weak excitation leads to a substantial energy increase *only if* close enough to the natural frequency. In the mechanical domain the working principle of parametric driving can be easily visualized by thinking at a child on a swing. In order to increase the swinging amplitude the child lowers and raises his center of gravity periodically in time. Experience will eventually teach him to do it at twice the frequency of the swing. Other areas in which parametric phenomena play a major part are, for instance, the stability of boats and inverted pendula [79], magnetic resonance force microscopy in micro and nano devices [80], electromagnetic ion traps [10] in quantum optical experiments and squeezing below the zero-point motion in optomechanical systems [81].

Parametric driving plays a particularly important role in the field of MEMS and NEMS. In their pioneering work, Rugar and Grütter refined a mechanical parametric amplification method to improve force detection sensitivity [8]. The proposed amplification technique works by choosing the frequency and strength of the parametric drive to lie just outside the first instability zone of the system, i.e. close to twice the natural frequency of the system (like the child above!).

In the exact same spirit, we investigate in this section the response of a parametric oscillator with particular regard to its instability. We first introduce a simple model of a HO in which parametric driving arises as a modulation of the natural frequency. We apply the AM (cf. Sec. I.3) to study the system in a parameter regime close to its first instability and derive an expression delineating the stability/instability boundary.

The content of this introductory section comprehend results that can be found in standard literature as well as personal unpublished results.

II.1.1 Model

The system under consideration is a HO in which parametric driving enters as a modulation of a single parameter: the system natural frequency. The EOM governing the dynamics of a damped parametric oscillator (PO) of mass m subject to a periodic external force is

$$m\ddot{x} + m\omega_0^2\big(1 - \lambda\cos\omega_p t\big)x + \gamma\dot{x} = F_0\cos\omega_f t, \tag{II.1}$$

where ω_0 is the unperturbed frequency of the oscillator, γ the linear damping and λ and ω_p denote the strength and frequency of the parametric drive. The external force is characterized by its strength F_0 and frequency ω_f. In its best-known form, parametric excitation describes the modulation of a resonator's natural frequency at *twice* the natural frequency itself [1, 5, 68, 82]. For this reason, we investigate the behavior of the system for the case where $\omega_p \approx 2\omega_0$. By the same token, we choose the frequency of the external drive as $\omega_f \approx \omega_0$. Standard resonance due to the action of an external force is indeed only effective when the frequency of the perturbation is close enough to the natural frequency of the system [1].

II.1.2 Response function and first instability

The harmless appearance of Eq. (II.1) conceals pitfalls: even though it is a linear differential equation of second oder it does not permit an analytical solution. The key point here is the presence of a periodic coefficient (the one multiplying the variable x). We thus resort to the perturbative AM, introduced in Sec. I.3, which replaces the full time dependent equation by an easier, time independent, averaged system. Before starting the procedure, we rewrite Eq. (II.1) in dimensionless form by redefining

time and length according to $\tau = \omega_0 t$ and $z = m\omega_0^2 x/F_0$. The resulting dimensionless EOM reads

$$\ddot{z} + \bar{\gamma}\dot{z} + \big(1 - \lambda\cos 2\Omega\tau\big)z = \cos(\Omega\tau + \vartheta), \tag{II.2}$$

where the dimensionless parameters are defined as $\bar{\gamma} \equiv \gamma/m\omega_0$ and $\Omega \equiv \omega/\omega_0$. Note that we focus here on the so called *degenerate* case [8], where the frequency of the external drive is locked at half the value of the parametric pump frequency. The parametrization of the frequency region around the first instability lobe is obtained by setting $\omega_p = 2\omega$, with $\omega \approx \omega_0$. We also allow a relative phase, denoted by ϑ, between the two drives.

The first step toward the averaged EOM is to reduce the second order differential equation (II.2) to a first order differential equation. More precisely, we can transform this one-dimensional second-order differential equation to a two-dimensional system of first-order differential equations by setting $y = \dot{z}$. This results in the following system

$$y = \dot{z}\,, \tag{II.3}$$

$$\dot{y} + \Omega^2 z = f(z, y, \tau)\,, \tag{II.4}$$

with

$$f(z, y, \tau) = -\sigma z - \bar{\gamma} y + \lambda\cos(2\Omega\tau)z + \cos(\Omega\tau + \vartheta). \tag{II.5}$$

We have introduced here the detuning parameter $\sigma = 1 - \Omega^2$. The next step is to bring the system into the standard form for averaging [cf. Eqs. (I.9) and (I.14)]. This can be done using the invertible Van der Pol transformation [51] to variables U and V,

$$\begin{bmatrix} z \\ y \end{bmatrix} = \begin{bmatrix} \cos\Omega\tau & -\sin\Omega\tau \\ -\Omega\sin\Omega\tau & -\Omega\cos\Omega\tau \end{bmatrix} \begin{bmatrix} U \\ V \end{bmatrix}. \tag{II.6}$$

The resulting equations for the evolution of U and V are given by

$$\begin{bmatrix} \dot{U} \\ \dot{V} \end{bmatrix} = -\frac{1}{\Omega} \begin{bmatrix} \sin\Omega\tau \\ \cos\Omega\tau \end{bmatrix} f(z, y, \tau), \tag{II.7}$$

where the right-hand side has to be expressed in terms of U and V according to Eq. (II.6). The system (II.7) is in the so-called standard form and the AM can easily be applied. To first order the averaged system is simply obtained by averaging the last equation over one period

$T = 2\pi/\Omega$ [see Eq. (I.17)]. This leads to the following slow flow equations

$$\dot{u} = -\frac{1}{2\Omega}\left[\bar{\gamma}\Omega u + v\left(\sigma + \frac{\lambda}{2}\right) - \sin\vartheta\right], \tag{II.8}$$

$$\dot{v} = -\frac{1}{2\Omega}\left[\bar{\gamma}\Omega v + u\left(-\sigma + \frac{\lambda}{2}\right) + \cos\vartheta\right], \tag{II.9}$$

for the two slow flow variables $u = \overline{U}$ and $v = \overline{V}$. The study of this averaged system reveals important informations about the original system.

The stability diagram of the system can be investigated by considering the obtained system in the absence of an external force[1]. The general solution of the resulting system of differential equations, which has the form

$$\dot{u} = -\frac{1}{2\Omega}(Au + Bv), \tag{II.10}$$

$$\dot{v} = -\frac{1}{2\Omega}(Av + Cu), \tag{II.11}$$

is given by

$$u(\tau) = \mathrm{e}^{-\frac{A}{2\Omega}\tau}\left[u_0\cosh\kappa\tau - v_0\sqrt{\frac{B}{C}}\sinh\kappa\tau\right], \tag{II.12}$$

$$v(\tau) = \mathrm{e}^{-\frac{A}{2\Omega}\tau}\left[v_0\cosh\kappa\tau - u_0\sqrt{\frac{C}{B}}\sinh\kappa\tau\right], \tag{II.13}$$

where $\kappa \equiv \sqrt{BC}/2\Omega$. From Eqs. (II.12) and (II.13) we see that the stability condition for the system, which is not affected by the transformation (II.6), is given by $\kappa = A/2\Omega$, i.e. $A = \sqrt{BC}$. In the present case, where $A = \bar{\gamma}\Omega$, $B = \sigma + \lambda/2$ and $C = -\sigma + \lambda/2$, this translates into the following equation for the stability boundary

$$(\bar{\gamma}\Omega)^2 = (\lambda/2)^2 - \sigma^2. \tag{II.14}$$

The boundary obtained from Eq. (II.14) is shown in Fig. II.1. Along this boundary, as can be seen from Eqs. (II.12) and (II.13), the system has an oscillatory behavior. For smaller (resp. larger) values of λ the system is stable (resp. unstable). Here stable means that for long enough times

[1] The stability only depends on the parametric drive, not on the direct one.

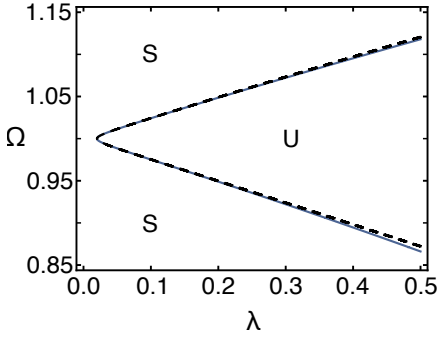

Figure II.1: First instability lobe (Arnold tongue) of the PO. The instability boundary obtained through first order averaging (continuous blue line) is compared to the one obtained through numerical computation of the Floquet exponents (dashed black line). Stable regions are denoted by S, while unstable by U. The damping parameter is $\bar{\gamma} = 0.01$.

the motion of the system decays to zero, while unstable stands for the (exponential) divergence of the amplitude of the motion.

The frequency response of the full system, which is a steady-state property, can be obtained from the fixed points of Eqs (II.8) and (II.9). Setting the left-hand side of these equations to zero and solving for u and v gives

$$u = \frac{1}{(\bar{\gamma}\Omega)^2 - (\lambda/2)^2 + \sigma^2}\left[-\bar{\gamma}\Omega\sin\vartheta + \cos\vartheta\left(-\sigma - \frac{\lambda}{2}\right)\right], \quad \text{(II.15)}$$

$$v = \frac{1}{(\bar{\gamma}\Omega)^2 - (\lambda/2)^2 + \sigma^2}\left[-\sin\vartheta\left(\sigma - \frac{\lambda}{2}\right) + \bar{\gamma}\Omega\cos\vartheta\right]. \quad \text{(II.16)}$$

Recalling now the transformation (II.6), that is $z = u\cos\Omega\tau - v\sin\Omega\tau$, we can rewrite z in terms of the slowly varying amplitude r and phase ϕ as $z = r(\tau)\cos(\Omega\tau + \phi(\tau))$. For the moment, we restrict ourselves to study the amplitude of the motion, denoted by $|\bar{X}|$, which is given by $|\bar{X}| = (u^2 + v^2)^{1/2}$. From the Eqs. (II.15) and (II.16) we immediately get

$$|\bar{X}| = \frac{\sqrt{(\bar{\gamma}\Omega)^2 + \sigma^2 + \left(\frac{\lambda}{2}\right)^2 + \lambda(\sigma\cos 2\vartheta + \bar{\gamma}\Omega\sin 2\vartheta)}}{(\bar{\gamma}\Omega)^2 + \sigma^2 - \left(\frac{\lambda}{2}\right)^2}. \quad \text{(II.17)}$$

This equation relates the amplitude of the oscillator response to the

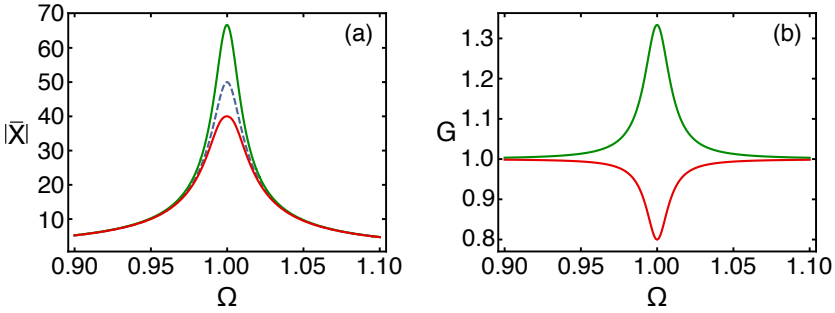

II

Figure II.2: (a) Typical frequency response for the usual HO (dashed line) and the PO (continuous lines). For the red (lower) line $\vartheta = 3\pi/4$ and the response is suppressed, while for the green (upper) line $\vartheta = \pi/4$ the response is enhanced. In (b) we show the gain function for the same two phases.

amplitude and frequency of the drives. The typical response for different regimes are plotted in Fig. II.2(a). We can see that parametric driving enhances or reduces the response depending on the relative phase between direct and parametric drives. For instance, for $\vartheta = \pi/4$ (respectively, $\vartheta = 3\pi/4$) we have a remarkable increase (respectively, decrease) of the gain [see Fig. II.2(b)]. The gain function is here defined as $G = |\bar{X}|_{\lambda\neq 0}/|\bar{X}|_{\lambda=0}$, in accordance with Ref. [8]. It is a simple comparison between the amplitude response of the PO ($|\bar{X}|_{\lambda\neq 0}$) and the one of the standard HO ($|\bar{X}|_{\lambda=0}$).

II.2 Nonlinear system

For minuscule resonators, such those in MEMS and NEMS devices, nonlinearities are almost unavoidable and the linear Eq. (II.1) ceases to furnish an acceptable description of the observed phenomena. Hence, we improve our model by incorporating nonlinearities which may arise from geometric effects as well as damping mechanisms. The resulting EOM, governing the dynamics of a nonlinear PO of mass m subject to a periodic external force, reads

$$m\ddot{x} + m\omega_0^2\left(1 - \lambda\cos\omega_p t\right)x + \gamma\dot{x} + \alpha x^3 + \eta x^2\dot{x} = F_0\cos\omega_f t, \quad \text{(II.18)}$$

where the parameters ω_0, γ, λ and ω_p are the same ones we already introduced for the linear case [see Eq. (II.1)]. Parametric resonance occurs whenever the parametric drive frequency satisfies the condition $\omega_p = 2\omega_0/n$, where n is an integer which labels the instability zones. As for the linear oscillator, we focus here on the case for which the effects of parametric driving are most pronounced, i.e. for $n = 1$. The nonlinearities are described by the Duffing parameter α characterizing the quartic contribution to the oscillator potential, and η the strength of the nonlinear feedback cooling, or nonlinear damping, that is present in generic experimental setups [83, 84]. Though nonlinearities stabilize the regions of instability [11, 78], the nonlinear parametric resonator retains a precise memory of the instability regions of the linear PO (see Sec. II.6).

Similarly to the linear case, the term on the right hand side of (II.18) refers to a periodic external force of strength F_0 and frequency ω_f. Equation (II.18) generically describes the physics of resonators realized in a wide range of experimental setups. Though a vast literature exists on the solutions to this equation in various regimes [11, 85], surprisingly, the impact of a periodically modulated external force on the full nonlinear problem has not been studied in great detail. In the following we consider a positive Duffing parameter α. Our methodology and results can be straightforwardly extended to the case of negative Duffing coefficients (as will be discussed later).

The main focus of this work involves studying the response of a parametric resonator to an external force, $F_0 \neq 0$, in the nonlinear regime. Bifurcations arise in this problem which essentially change the nature of the associated response. Equation (II.18) is a nonautonomous, inhomogeneous and nonlinear differential equation that does not permit an analytic solution for generic parameters. In typical experiments, the focus is on the first parametric resonance of the system, i.e. operating around twice the bare frequency of the undriven oscillator $\omega_p \approx 2\omega_0$ while the frequency of the external drive is $\omega_f \approx \omega_0$. As we will show, approximate analytic solutions to the frequency dependent response can be obtained in these experimentally relevant parameter regimes.

II.3 Response function

To analyze the EOM [Eq. (II.18)] we use again the perturbative AM, see Sec. I.3. Before that, we redefine time and length in Eq. (II.18) according

to[2] $\tau = \omega_0 t$ and $z = x\sqrt{\alpha/m\omega_0^2}$. This leads to the dimensionless EOM

$$\ddot{z} + \bar{\gamma}\dot{z} + z^3 + \bar{\eta}z^2\dot{z} + (1 - \lambda\cos 2\Omega\tau)\, z = \bar{F}_0\cos(\Omega\tau + \vartheta), \qquad \text{(II.19)}$$

where the dimensionless parameters are defined as $\bar{\gamma} \equiv \gamma/m\omega_0 = 1/Q$, $\bar{\eta} \equiv \eta\omega_0/\alpha$, $\Omega \equiv \omega/\omega_0$, and $\bar{F}_0 \equiv (F_0/\omega_0^3)\sqrt{\alpha/m^3}$. Exactly as for the linear case, the frequency region around the first instability lobe is parametrized by setting $\omega_p = 2\omega$, with $\omega \approx \omega_0$. We introduce again the detuning parameter $\sigma = 1 - \Omega^2$. Once more, we lock the frequency of the external drive at half the value of the parametric pump frequency $\omega_f = \omega$, with a relative phase ϑ between the two drives. With the parameters so defined, Eq. (II.18) can be recast as a pair of first order equations

$$y = \dot{z}\,, \qquad \text{(II.20)}$$

$$\dot{y} + \Omega^2 z = f(z, y, \tau)\,, \qquad \text{(II.21)}$$

with

$$f(z, y, \tau) = -\sigma z - \bar{\gamma}y - z^3 - \bar{\eta}z^2 y + \lambda\cos(2\Omega\tau)z + \bar{F}_0\cos(\Omega\tau + \vartheta). \qquad \text{(II.22)}$$

Note that, in order for the present perturbative method to be valid, the detuning σ, linear and nonlinear damping $\bar{\gamma}$ and $\bar{\eta}$, as well as the driving strengths λ and $\bar{F}_0$ have to be small. Since Eqs. (II.20)-(II.22) are dimensionless, the true range of forces that can be studied with this perturbative method, depends on the particular realization of the nonlinear resonator. Eq. (II.21) is brought into the so-called standard form for averaging, i.e., into a form $\dot{z} = \epsilon f(z, y, \tau)$ with $0 < \epsilon \ll 1$, using the Van der Pol transformation (II.6) [51]. Substituting Eq. (II.6) in Eq. (II.21) and averaging over the time period $T = 2\pi/\Omega$, we obtain the equations for the slow flow variables $u = \overline{U}$ and $v = \overline{V}$, which correspond to time-

[2]Note the different way in which length has been renormalized in the linear and nonlinear case.

averaged U and V over the time cycle:

$$\dot{u} = -\frac{1}{2\Omega}\left[\bar{\gamma}\Omega u + v\left(\sigma + \frac{\lambda}{2}\right) + \frac{3}{4}(u^2+v^2)v + \Omega\frac{\bar{\eta}}{4}(u^2+v^2)u - \bar{F}_0\sin\vartheta\right], \tag{II.23}$$

$$\dot{v} = -\frac{1}{2\Omega}\left[\bar{\gamma}\Omega v + u\left(-\sigma + \frac{\lambda}{2}\right) - \frac{3}{4}(u^2+v^2)u + \Omega\frac{\bar{\eta}}{4}(u^2+v^2)v + \bar{F}_0\cos\vartheta\right]. \tag{II.24}$$

Despite the perturbative nature of the AM, its results are valid for a surprisingly large range of values of the drive amplitude λ as well as for substantial detuning Ω (cf. Fig. II.1 and Ref. [86]). However, to access the full range of the system parameters as well as more complex nonlinearities, one would need to do a full numerical study.

The coupled slow flow Eqs. (II.23) and (II.24) remain analytically insolvable. However, from the perspective of measurements, one only needs to know the frequency response of the oscillator $|\bar{X}| = (u^2 + v^2)^{1/2}$. This is a property of the steady-state and does not require knowledge of transients. Consequently, in the steady-state, we set $\dot{u} = \dot{v} = 0$ in Eqs. (II.23) and (II.24), and we find that the response $|\bar{X}|^2$ satisfies the following polynomial equation

$$|\bar{X}|^2\left[\left(\bar{\gamma}\Omega + \frac{\bar{\eta}}{4}\Omega|\bar{X}|^2\right)^2 - \left(\frac{\lambda}{2}\right)^2 + \left(\sigma + \frac{3}{4}|\bar{X}|^2\right)^2\right]^2 = \bar{F}_0^2\left[\left(\bar{\gamma}\Omega + \frac{\bar{\eta}}{4}\Omega|\bar{X}|^2\right)^2 + \left(\frac{\lambda}{2}\right)^2 + \left(\sigma + \frac{3}{4}|\bar{X}|^2\right)^2 + \lambda\left(\sigma + \frac{3}{4}|\bar{X}|^2\right)\cos 2\vartheta + \lambda\left(\bar{\gamma}\Omega + \frac{\bar{\eta}}{4}\Omega|\bar{X}|^2\right)\sin 2\vartheta\right]. \tag{II.25}$$

Equation (II.25) determines the response in a finite frequency interval ω around ω_0. Obtaining the response for arbitrary ω requires a non-perturbative approach or the retention of higher order corrections.

As will be shown below, the interplay between the periodic external force, parametric drive and nonlinearities leads to two qualitative different behaviors for the response depending on the position in parameter space. The solutions to the fifth order polynomial[3] [Eq. (II.25)] can be sta-

[3] We only keep the half of the solutions for which $|\bar{X}|^2$ is positive.

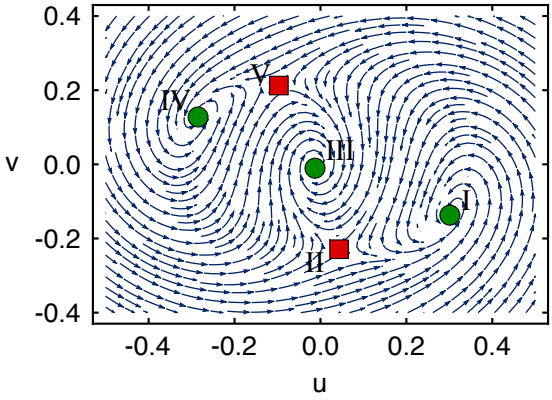

Figure II.3: Trajectories of the nonlinear parametric resonator in slow variables u and v, obtained by numerically integrating Eqs. (II.23) and (II.24). The parameters chosen correspond to the unstable regime of the unforced linear parametric resonator: $\lambda = 5 \times 10^{-2}$, $\bar{F}_0 = 1 \times 10^{-3}$, $\bar{\gamma} = 1 \times 10^{-2}$, $\bar{\eta} = 3 \times 10^{-1}$, $\vartheta = 0$ and $\Omega = 1.03$. The green circles denote stable solutions, while red squares unstable ones.

ble or unstable[4]. The stabilities can be directly inferred from the basins of attraction for this equation, plotted in Fig. II.3. We find that typically one has three stable solutions (I, III and IV) marked by green dots and two unstable solutions (II and V) denoted by the red squares.

For small amplitudes of the parametric drive λ pertaining to the stable regime [see inset in Fig. II.4(a)], the response shown in Fig. II.4(a) is dominated by the external force and resembles that of the Duffing oscillator [51]. Here the stable solutions I and IV become degenerate and the response has two stable branches (I and III) and one degenerate unstable branch (II). As λ increases and one crosses over to the unstable regime of the underlying linear oscillator [see inset in Fig. II.4(b)], the degeneracies of both stable and unstable solutions are broken corresponding to the three stable attractors and two saddle points shown in Fig. II.3.

[4]The Hartman-Grobman theorem [51, 87] states that the behavior of solutions of a nonlinear system near a hyperbolic fixed point is determined by the linearization near this equilibrium point. The stability analysis of the solutions shown in Fig. II.4 hence requires the repeated numerical solution of Eqs. (II.23) and (II.24) for different fixed values of Ω. The nonlinear system is then linearized around the found fixed points (u^*, v^*) and its stability is finally established. The results are further confirmed by the phase space trajectories shown in Fig. II.3.

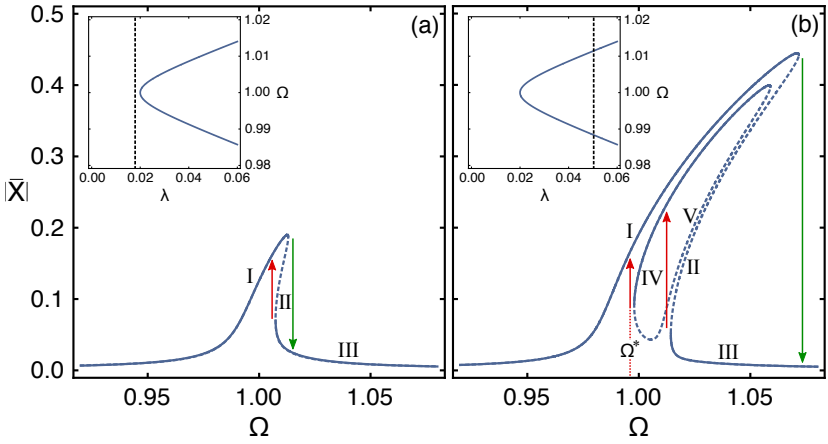

Figure II.4: Typical frequency responses of the system described by Eq. (II.18). The insets show the first instability region (Arnold tongue) of the unforced linear parametric resonator ($\alpha = \eta = F_0 = 0$) (continuous lines) and the chosen values of λ (dashed lines). (a) $\lambda = 1.8 \times 10^{-2}$ below the instability threshold (dashed line in inset); (b) $\lambda = 5 \times 10^{-2}$ above the instability threshold (dashed line in inset). Stable branches are indicated by whole lines, while unstable branches by dashed lines. The parameters $\bar{F}_0 = 1 \times 10^{-3}$, $\bar{\gamma} = 1 \times 10^{-2}$, $\bar{\eta} = 3 \times 10^{-1}$ and $\vartheta = 0$ are the same in both (a) and (b).

This generates a qualitatively different response as shown in Fig. II.4(b), with an enhanced Duffing-type response encompassing an island-like structure. This is due to a complex interplay between the cubic nonlinearity, the external force and the parametric drive. We reiterate that this response cannot be obtained without the periodic external force. The splitting takes place even in the absence of noise-activated switching between the stable solutions, in contrast to previous studies [88].

As F_0 increases, the island is raised and shifted to larger frequencies. A sufficiently strong F_0 wipes out the internal island and the resulting frequency response is external force dominated and appears to be Duffing-like. In the limit $F_0 \to 0$, we recover the response of a pure parametric system (cf. Sec. II.6), where I and IV (II and V) coalesce to a single stable (unstable) branch. The presence of F_0 thus leads to a splitting of the stable (unstable) branch into two stable (unstable) branches.

We now analyze the dependence of this novel response on the vari-

ous tunable parameters in the system. The driving strength λ strongly affects both the maximal amplitude of the response as well as the frequency at which the intermediate stable branch originates. As λ increases, the intermediate branch dips further towards lower frequencies though the maximal response increases. Linear damping γ, on the other hand simply shifts the stability boundaries of the linear PO away from the $\lambda = 0$ axis [see inset in Fig. II.4(a)]. As a result, for the response, it plays a role akin to the inverse of the driving strength λ, i.e. the larger the damping, the smaller the response and the origin of the intermediate branch is pushed to higher frequencies. For sufficiently large damping γ, one enters the parameter region where the linear oscillator is stable and we recover the typical response of Fig. II.4(a). Importantly, nonlinear damping η caps the response when ω increases, but it preserves the intermediate stable branch and the island-like structure.

II.4 Force detection

We will now show that the amplitude of the near resonant periodic external force can be directly extracted from the qualitatively new response discussed earlier. The presence of stable and unstable branches in the response is expected to lead to hysteretic behavior during upward and downward sweeps of the frequency ω across ω_0. Consider the response for weak parametric driving plotted in Fig. II.4(a). For upward sweeps of the frequency across ω_0, the response will gradually increase along branch I all the way to the maximal value where it hits the upper bifurcation and will then abruptly drop to the value of the lower stable branch III [green arrow pointing downwards in Fig. II.4(a)]. For downward sweeps, the response slowly increases along branch III and then jumps abruptly to the stable branch I (red arrow pointing upwards). This is very similar to the standard Duffing-like hysteresis seen in many systems both in the presence and absence of an external force [11, 51]. The sizes of the hysteretic jumps depend on many parameters, including F_0. It is highly nontrivial to extract the amplitude of the force from this hysteresis curve.

For λ in the unstable regime of the linear oscillator [cf. Fig. II.4(b)], the presence of additional branches in the response leads to a new kind of hysteresis curve. For upward sweeps across the resonance frequency, the response will gradually increase all the way along branch I to the

maximal value where it hits the upper bifurcation and will then abruptly drop to the value of the lower stable branch III. For downward sweeps, the response will increase very slowly across branch III until it hits the first bifurcation where it will abruptly jump to the stable branch IV of the island. It will then decrease further until it hits another bifurcation of the island at a frequency Ω^* where it will jump to the stable branch I. In short, the presence of stable solutions in the island results in two consecutive jumps in the downward sweeps.

The hysteretic jumps expected for the two response functions in the stable and unstable regimes are indicated in Fig. II.4. Figure II.4(b) shows a double jump hysteresis whereas Fig. II.4(a) shows the standard single jump hysteresis. The second jump in Fig. II.4(b) is a direct manifestation of the intermediate stable branch discussed above and exists only when the amplitude of the external force F_0 is nonzero. The second jump is lost for high values of η as the island shifts to higher frequencies. This feature provides a promising new method to detect weak forces. The force F_0 can be extracted either from the magnitude of the second jump or from the frequency Ω^* at which it occurs.

We find that Ω^* depends linearly on F_0 for a wide range of forces, allowing for a new and simple force detection scheme [see Fig. II.5(a)]. The slope of Ω^* versus $\bar{F}_0$ ($\Omega^* = \omega^*/\omega_0$) defines a dimensionless sensitivity $\bar{\kappa}$ which can be translated into physical units through the relation $\kappa = \frac{\bar{\kappa}}{\omega_0^2}\sqrt{\frac{|\alpha|}{m^3}}$. The jump frequency, and thus the sensitivity, also depend on the relative phase between the periodic drive and the external force, as shown in the inset of Fig. II.5(a). In the following, we consider the two cases that will be most relevant for experiments. On the one hand, if the phase ϑ of F_0 is stable and can be controlled, one can reach the maximum sensitivity $\kappa_{\max}$ that corresponds to $\vartheta \approx \pi/4$ [red dashed line in Fig. II.5(a)]. On the other hand, if the phase of F_0 is fluctuating, one effectively obtains a phase-averaged measurement with sensitivity κ_{mean} [blue solid line in Fig. II.5(a)]. In Fig. II.5(b), we plot the phase averaged dimensionless sensitivity of the device ($\bar{\kappa}_{\text{mean}}$) as a function of λ and $\bar{\eta}$. It is worth noting that as long as the parametric drive λ is beyond the instability threshold, the sensitivity *increases* with decreasing λ. We present values for both $\kappa_{\max}$ and κ_{mean} for typical experimental systems in the following section.

We note that a similar double jump hysteresis is expected for a system with negative Duffing parameter α where the response tilts towards

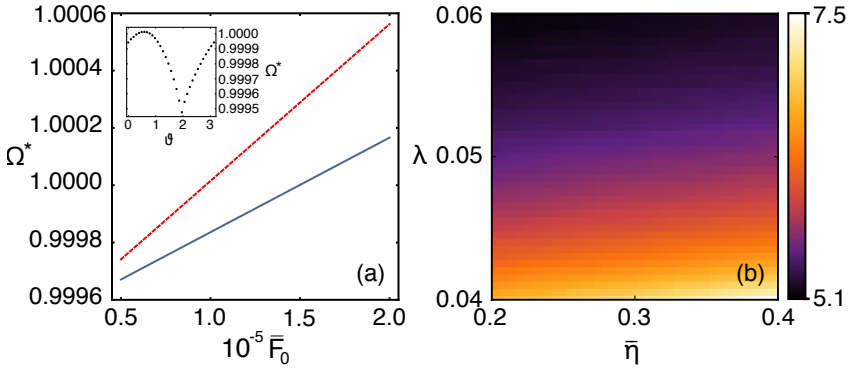

Figure II.5: (a) Jump frequency Ω^* as a function of the strength of the external force for $\vartheta = \pi/4$ (red dashed line) and averaged over a uniformly distributed phase ϑ (blue solid line). The parameters are given by $\lambda = 0.016$, $\bar{\gamma} = 10^{-3}$ and $\bar{\eta} = 5 \times 10^{-3}$. The inset shows the phase dependence of the jump frequency Ω^* for a fixed value of the external force ($\bar{F}_0 = 1 \times 10^{-5}$). (b) Sensitivity $\bar{\kappa}$ as a function of the strength of the parametric drive λ and nonlinear damping $\bar{\eta}$. The force range $\bar{F}_0$ is from 5×10^{-4} to 1×10^{-3}, and $\bar{\gamma} = 10^{-2}$. The other parameters are kept fixed.

the left (spring softening) [11]. In this case, Ω^* decreases linearly with increasing F_0 but the sensitivity, given by the magnitude of the slope, is expected to be the same as that for positive α. In other words, regardless of the sign of α, a direct measurement of the hysteresis curve in the nonlinear regime of the parametrically driven resonator permits a straightforward extraction of the amplitude of the external force.

Importantly, from an experimental perspective, one needs a nonlinear oscillator with well characterized Duffing nonlinearity, tunable parametric modulation and, preferably, nonlinear feedback cooling. The latter is particularly useful in generating a sizable second hysteretic jump. The device should first be calibrated, i.e. its sensitivity κ should be obtained via a series of measurements of Ω^* for different values of known force amplitudes F_0. Once the sensitivity is known, the device can be used to measure the amplitude of an unknown external force.

II.5 Discussion

We now discuss the magnitudes of the forces that can be detected via the double hysteresis scheme. We consider an external force to be in principle detectable when the frequency shift of the second hysteresis is larger than the frequency noise present in the system, that is, if

$$\kappa F_0 \geq \sigma_f, \tag{II.26}$$

where κ is the sensitivity of the device in physical units of angular frequency per force and we use σ_f to denote the total (angular) frequency noise expected during a measurement. The minimum detectable force is then given by $F_{\mathrm{min}} = \sigma_f/\kappa$.

We present estimates for the range of forces which can be detected with two different resonators. We first consider a laser-trapped nanoparticle in high vacuum [89] with a very high quality factor and a negative Duffing coefficient α. This system allows for a wide manipulation of the system parameters with small thermal noise. The system parameters are: $m \approx 3 \times 10^{-18}$ kg, $\omega_0 \approx 2\pi \times 1.25 \times 10^5$ s^{-1}, $Q \approx 10^8$ (controlled through the air pressure) and $|\alpha| \approx 1.8 \times 10^7$ kg m^{-2}s^{-2}. The nonlinear damping due to feedback cooling can be tuned in a range around $\eta \approx 14$ kg m^{-2}s^{-1} and the amplitude of the parametric drive we use is $\lambda = 10^{-4}$, which is well inside the available modulation range. Calculating $\bar{\kappa}$ from solutions of Eq. (II.25) and then transforming into physical units, we obtain $\kappa_{\mathrm{mean}} = 4 \times 10^{19}$ Hz/N and $\kappa_{\mathrm{max}} = 5.6 \times 10^{19}$ Hz/N. For a sweep duration of typically a few seconds, the frequency noise can be expected to be in the range of 2π kHz in units of angular frequency [84], which gives a minimum detectable force of about 110 aN and 160 aN for κ_{max} and κ_{mean}, respectively. Please note that the frequency noise used here is largely dominated by laser intensity noise and could in principle be decreased substantially.

The lightest nanomechanical resonators available today are made of individual carbon nanotubes. These resonators have pronounced nonlinearities and can be driven parametrically with high modulation depth [90]. Typical parameters are [83]: $m \approx 10^{-20}$ kg, $\omega_0 \approx 2\pi \times 5 \times 10^7$ s^{-1}, $Q \approx 10^3$, $\eta \approx 10^3$ kg m^{-2}s^{-1}, $|\alpha| \approx 4 \times 10^{11}$ kg m^{-2}s^{-2} and $\lambda = 2.5 \times 10^{-3}$. With these parameters, we get $\kappa_{\mathrm{mean}} = 4.5 \times 10^{20}$ Hz/N and $\kappa_{\mathrm{max}} = 7 \times 10^{20}$ Hz/N. From the linewidth of the frequency sweep in Fig. 4 of Ref. [83], we estimate an upper bound for the frequency noise

of $2\pi \times 5$ kHz in units of angular frequency, which result in minimum detectable forces of 45 aN and 70 aN for $\kappa_{\max}$ and κ_{mean}, respectively. The quality factor we use here is quite conservative. Values of up to $Q = 5 \times 10^6$ have been measured more recently [91]. The same study also demonstrated significantly reduced frequency noise. However, it is not clear how the device will behave when driven into the nonlinear regime.

We expect weak thermal fluctuations to broaden the response and modify the size of the hysteretic jumps, but leave Ω^* effectively unchanged. As a result, thermal noise will not have any qualitative impact on our detection scheme for devices with very high Q factors. Generically, we expect the force to be detectable as long as the second jump is visible above the background noise. This should hold true as long as the system parameters as well as noise are such that one avoids activation of degenerate states or higher energy states. Note, the combination of driving, nonlinearities and noise could lead to phenomena similar to stochastic resonance in the present context, but the study of these aspects is beyond the scope of the present work.

To conclude, we have presented a new paradigm for sensitive detection of forces using nonlinear parametric resonators. Though based on the nonlinear dynamics of the resonator, our measurement scheme is inherently linear. NEMS with relatively large Duffing nonlinearity α are good candidates for our force detection scheme. For state-of-the-art devices, our scheme might allow the detection of forces in the $10 - 100$ aN range. Furthermore, the high sensitivities associated with our detection scheme can potentially be exploited in the context of techniques such as nano-MRI aiming at great spatial resolution [92, 93].

II.6 Parametric symmetry breaking

So far the study of the frequency-response of a system described by Eq. (II.18) has been focused on the amplitude of the motion. The other side of the coin, i.e. the phase of the motion, provides further insights into the physics underlying the problem.

The response of the nonlinear PO in the absence of an external driving force features two very different behaviors that strongly depend on the stability of the linear oscillator [1, 85]. Even though the phenomenon of parametric resonance is eliminated by nonlinearities, the

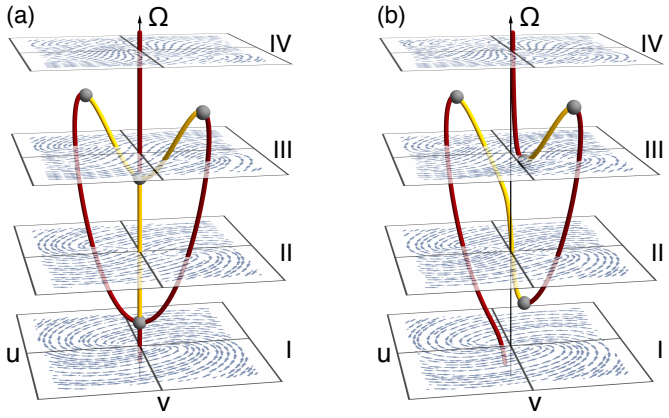

Figure II.6: Typical frequency responses of the system described by Eq. (II.18). In (a) the system is subject to purely parametric drive ($\lambda \neq 0$, $F_0 = 0$), while in (b) both external and parametric drives are turned on ($\lambda \neq 0$, $F_0 \neq 0$). Stable solutions (dark red lines) and unstable solutions (bright yellow lines), as well as the bifurcations (grey spheres) are shown as a function of Ω. In both cases, four domains (I-IV) of the response appear, which are characterized by a different number of solutions. The parameters are chosen to match those of the experiment (see Ref. [41]), i.e. $\bar{F}_0 = 0$ in (a) and $\bar{F}_0 = 1.2 \times 10^{-6}$ in (b); the other parameters $\lambda = 1.43 \times 10^{-3}$, $\bar{\gamma} = 1/1800$, $\bar{\eta} = 0.57$ and $\vartheta = -\pi/4$ are the same in both figures.

stability boundary of the linear system plays an important role for the nonlinear system. Outside the instability lobe the motion of the system is suppressed to zero. On the contrary, inside the instability lobe it displays two stable oscillation solutions. These two solutions, which we term "parametric phase states", are degenerate in amplitude but phase shifted by π [see Fig. II.6(a)]. Our results show that a periodic external force can lift the amplitude degeneracy between the parametric phase states, see Fig. II.6(b). This degeneracy lifting becomes pronounced in the presence of nonlinear damping and leads to a robust double hysteresis in the frequency-swept response of the resonator [cf. Fig. II.4(b)], which can be used to measure small near-resonant forces. Both figures show the Ω-dependent stability diagram of the system. Shown are the trajectories of the oscillator in slow variables u and v for four different domains (I-IV), from which the basins of attraction can be identi-

fied, along with the evolution of stable attractors and unstable saddle points. One can see clearly how, as a function of Ω, the total number of stationary solutions increases (decreases) due to generation (annihilation) of pairs of stable-unstable solutions at bifurcation points (see grey spheres in the figure). Following the evolution of the stable solutions in Fig. II.6(b) with increasing or decreasing Ω reveals the origin of the second hysteretic jump in both amplitude and phase. Intuitively, we can construct the full stability diagram from the purely parametric case by regarding the external drive as a perturbation. As a consequence of this perturbation, the parametric phase states are no longer symmetric and the trivial solutions ($u = 0 = v$) seen in Fig. II.6(a) are shifted toward finite amplitudes. Importantly, an opposite phase is imprinted on the stationary solution by the external drive in regions I and IV. As a combined result of these two effects, for opposing directions of frequency sweeps, a different parametric phase state is chosen and the double hysteresis is seen.

II.6.1 Experimental realization

Besides providing the theory behind the double-hysteretic response of the driven nonlinear oscillator, we contributed to its first experimental observation [41]. As a demonstrator, we used a macroscopic mechanical resonator that is similar to state-of-the-art nanomechanical resonators in terms of nonlinear characteristics while offering easy tuning and a signal-to-noise ratio that is rarely attained in nanomechanical devices.

The experimental setup, built in-house, consists of a doubly-clamped steel string, see Fig. II.7. The string acts as an Euler-Bernoulli beam in the high-tension limit [85]. Parametric excitation is realized by modulation of the position of one clamping point to change the tension of the string. The motion of the string at angular frequency ω is transduced into a voltage and read out via a lock-in amplifier (see Ref. [41] for further details). The lowest energy mode of the device satisfies the well-known EOM for a nonlinear, parametrically excited resonator [85], see Eq. (II.18). In Fig. II.8(a), the measured displacement amplitude for an upward frequency sweep exhibits a single jump (at the boundary between domains III and IV), akin to the jump expected in standard externally driven Duffing resonators in the absence of parametric excitation. However, for downward frequency sweeps, a double hysteresis appears and the response displays two consecutive jumps (at the III-II and II-I

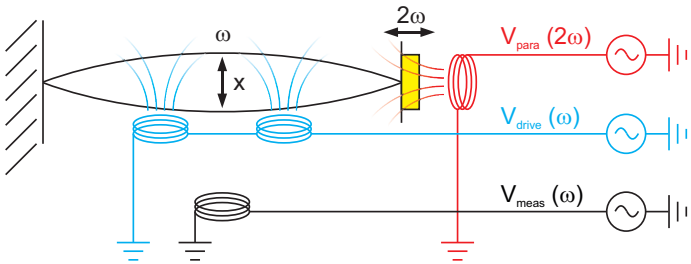

Figure II.7: Experimental realization of a parametric resonator based on a doubly clamped steel string. Direct driving at frequency ω and parametric excitation at frequency 2ω rely on ac currents through coils induced by voltages V_{drive} and V_{para} acting on the weakly magnetized steel wire and on a neodymium magnet (yellow element), respectively. The force acting on the magnet slightly displaces the right clamping point of the string. This displacement changes the tension in the string and generates a parametric modulation. The string position is read out from the voltage V_{meas} that is induced in a pickup coil by the vibrating and weakly magnetized string.

boundaries, respectively). While the jumps (III-IV) and (III-II) describe the typical hysteresis for externally driven Duffing resonators, the second jump (II-I) is a novel feature that stems from an interplay with parametric excitation and has not been seen before in an experiment. The same hysteretic responses are even more prominent in the measured oscillation phase, see Fig. II.8(b).

The theory results are found by rewriting Eqs. (II.23) and (II.24) in polar coordinates, where $u = r\cos\phi$ and $v = r\sin\phi$, and translating the obtained set of differential equations into physical units. For the sake of (experimental) convenience, this is done – instead of using Eq. (II.18) – consistently with the following equation

$$\ddot{x} + \omega_0^2\left[1 - \lambda\cos\left(2\omega t\right)\right]x + \gamma\dot{x} + \alpha x^3 + \eta x^2\dot{x} = \frac{F_0}{m}\cos\left(\omega t + \vartheta\right).$$

The resulting EOM for the displacement amplitude, r, and phase, ϕ, read

$$\dot{r} = -\frac{\alpha r\omega\left(4\gamma + \eta r^2\right) + 2\alpha k\lambda r\sin 2\phi + 4F_0\alpha\sin\left(\phi - \vartheta\right)}{8\omega k\sqrt{\alpha m}}, \tag{II.27}$$

$$\dot{\phi} = \frac{\omega_0}{2\omega}\left[\frac{3\alpha r^2}{4k} + 1 - \frac{\omega^2}{\omega_0^2} - \frac{\lambda}{2}\cos 2\phi - \frac{F_0}{kr}\cos\left(\phi - \vartheta\right)\right], \tag{II.28}$$

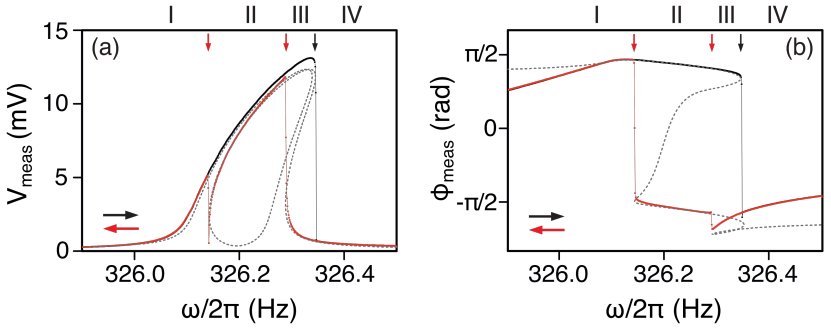

Figure II.8: First experimental demonstration of double-hysteretic response: (c) mean displacement and (d) oscillation phase as a function of ω for both upward sweep (black line-dots) and downward sweep (red line-dots). Four domains (I-IV) of the response appear. Theory curves are gray dashed lines. See Ref. [41] for further details on the experimental parameters.

where $k = m\omega_0^2$. Using the experimentally extracted values for the resonator parameters, we find that the model results, which are shown in Fig. II.8 as gray dashed lines, are in excellent agreement with the experiment and allow an unambiguous interpretation of the measured phenomena.

II.7 Second instability lobe

So far we have investigated the peculiar response of the system when parametrically driven inside the first Arnold tongue. What we want to understand now is whether the observed double hysteresis is a unique feature of the first lobe or not. To give this question an answer we investigate the response of the system for a frequency region around the second instability lobe. In order to explore this parameter regime we need to perform second order averaging as, to first order, linear damping completely stabilizes higher resonance regions other than the first one.

The system is still described by Eq. (II.18), but now we consider the case in which $\omega_p \approx \omega_0$, instead of $2\omega_0$. The right-hand side of Eq. (II.21)

is simply replaced by

$$f(z,y,\tau) = -\sigma z - \bar{\gamma} y - z^3 - \bar{\eta} z^2 y + \lambda \cos(\Omega\tau) z + \bar{F}_0 \cos(\Omega\tau + \vartheta). \tag{II.29}$$

Using again the Van der Pol transformation (II.6) we can recast the equations for the evolution of U and V in the same form of Eq. (II.7). By defining $\mathbf{U} = (U, V)$ and $\mathbf{f}(z, y, \tau) = (-\sin\Omega\tau, -\cos\Omega\tau) f(z, y, \tau)/\Omega$ we can express this equation as $\dot{\mathbf{U}} = \mathbf{f}(\mathbf{U}, \tau)$. We now split the function $\mathbf{f}$ into its mean, $\bar{\mathbf{f}}(\mathbf{U})$, and an oscillating part, $\tilde{\mathbf{f}}(\mathbf{U}, \tau)$, that is $\mathbf{f}(\mathbf{U}, \tau) = \bar{\mathbf{f}}(\mathbf{U}) + \tilde{\mathbf{f}}(\mathbf{U}, \tau)$. The first order result, obtained from $\bar{\mathbf{f}}(\mathbf{U})$, follows the same procedure outlined so far in this work. We will thus refrain from further details and directly present the outcome of the computation, which reads

$$\bar{f}_1 = -\frac{1}{2\Omega}\left[\bar{\gamma}\Omega u + \sigma v + \frac{3}{4}(u^2+v^2)v + \Omega\frac{\bar{\eta}}{4}(u^2+v^2)u - \bar{F}_0 \sin\vartheta\right], \tag{II.30}$$

$$\bar{f}_2 = -\frac{1}{2\Omega}\left[\bar{\gamma}\Omega v - \sigma u - \frac{3}{4}(u^2+v^2)u + \Omega\frac{\bar{\eta}}{4}(u^2+v^2)v + \bar{F}_0 \cos\vartheta\right]. \tag{II.31}$$

Note the absence of the strength of the parametric modulation, λ, in these two expressions. This parameter will appear again when including second order corrections. The oscillating part is then found by computing $\tilde{\mathbf{f}}(\mathbf{U}, \tau) = \mathbf{f}(\mathbf{U}, \tau) - \bar{\mathbf{f}}(\mathbf{U})$. According to Sec. I.3, the near-identity transformation $\mathbf{w}$ is chosen such that $\partial_\tau \mathbf{w} = \tilde{\mathbf{f}}(\mathbf{U}, \tau)$. Eventually, the second order correction is given by $\bar{\mathbf{g}} = \langle D\tilde{\mathbf{f}}(\mathbf{U}, \tau)\mathbf{w}\rangle_T$, where $\langle\cdot\rangle_T$ is a shorthand notation for the time average over a period T and $D\tilde{\mathbf{f}}(\mathbf{U}, \tau)$ is the Jacobian matrix $\partial(\tilde{\mathbf{f}}_1, \tilde{\mathbf{f}}_2)/\partial(U, V)$. The explicit expressions for the

components of $\bar{\mathbf{g}}$ are given by

$$\begin{aligned}\bar{g}_1 = \frac{1}{768\Omega^3}\Big[&v\Big(153(u^2+v^2)^2 - 32\lambda^2 + 288\sigma(u^2+v^2) + 96\sigma^2\Big)\\ &+24\bar{\eta}\Omega u(u^2+v^2)(u^2+v^2+2\sigma)\\ &+3\Omega^2 v\Big(32\bar{\gamma}^2 + 48\bar{\gamma}\bar{\eta}(u^2+v^2) + 11\bar{\eta}^2(u^2+v^2)^2\Big)\\ &-24\bar{F}_0\cos\vartheta\Big(6uv - 4\bar{\gamma}\Omega + \bar{\eta}\Omega(u^2-5v^2)\Big)\\ &-24\bar{F}_0\sin\vartheta\Big(9v^2 + 4\sigma + 3u(u+2\bar{\eta}\Omega v)\Big)\Big] \qquad \text{(II.32)}\end{aligned}$$

and

$$\begin{aligned}\bar{g}_2 = \frac{1}{768\Omega^3}\Big[&-u\Big(153(u^2+v^2)^2 + 160\lambda^2 + 288\sigma(u^2+v^2) + 96\sigma^2\Big)\\ &+24\bar{\eta}\Omega v(u^2+v^2)(u^2+v^2+2\sigma)\\ &-3\Omega^2 u\Big(32\bar{\gamma}^2 + 48\bar{\gamma}\bar{\eta}(u^2+v^2) + 11\bar{\eta}^2(u^2+v^2)^2\Big)\\ &+24\bar{F}_0\cos\vartheta\Big(9u^2 + 4\sigma + 3v(v-2\bar{\eta}\Omega u)\Big)\\ &+24\bar{F}_0\sin\vartheta\Big(6uv + 4\bar{\gamma}\Omega + \bar{\eta}\Omega(5u^2-v^2)\Big)\Big]. \qquad \text{(II.33)}\end{aligned}$$

The second order averaged system is obtained by summing the Eqs. (II.30) and (II.32), that is $\dot{u} = \bar{f}_1 + \bar{g}_1$, respectively Eqs. (II.31) and (II.33), that is $\dot{v} = \bar{f}_2 + \bar{g}_2$. The resulting averaged system is more complex than the first order one that we obtained for the first instability lobe [cf. Eqs. (II.23) and (II.24)]. As such, we cannot find a simple equation for the steady-state amplitude response anymore [cf. Eq. (II.25)].

Nonetheless, interesting properties of the system can still be investigated. The slow flow equations of the linear system take the same form of Eqs. (II.10) and (II.11) and thus the stability boundary is determined by the same condition: $A = \sqrt{BC}$. In the present case A is still given by $A = \bar{\gamma}\Omega$, while B and C now read $B = \sigma + \lambda^2/12\Omega^2 - \sigma^2/4\Omega^2 - \bar{\gamma}^2/4$ and $C = -\sigma + 5\lambda^2/12\Omega^2 + \sigma^2/4\Omega^2 + \bar{\gamma}^2/4$. The equation for the stability boundary of the second Arnold tongue is given by

$$(\bar{\gamma}\Omega)^2 = \left(\sigma + \frac{\lambda^2}{12\Omega^2} - \frac{\sigma^2}{4\Omega^2} - \frac{\bar{\gamma}^2}{4}\right)\left(-\sigma + \frac{5\lambda^2}{12\Omega^2} + \frac{\sigma^2}{4\Omega^2} + \frac{\bar{\gamma}^2}{4}\right).$$

We can access the amplitude and phase of the motion of the full system by switching to polar coordinates, where $u = r\cos\phi$ and $v = r\sin\phi$.

The averaged system in polar coordinates (r, ϕ) reads:

$$\begin{aligned}\dot{r} = -\frac{1}{2\Omega}\Bigg[&\bar{\gamma}\Omega r + \frac{\bar{\eta}}{4}\Omega r^3 + \frac{\lambda^2}{2\Omega^2} r\cos\phi\sin\phi - \frac{\bar{\eta}}{16\Omega}r^5 - \frac{\bar{\eta}\sigma}{8\Omega}r^3 \\ &+ \frac{\bar{F}_0}{16\Omega}\cos(\vartheta-\phi)\left(\bar{\eta}r^2 - 4\bar{\gamma}\right) \\ &+ \frac{\bar{F}_0}{16\Omega^2}\sin(\vartheta-\phi)\left(3r^2 + 4(\sigma - 4\Omega^2)\right)\Bigg] \end{aligned} \tag{II.34}$$

and

$$\begin{aligned}\dot{\phi} = -\frac{1}{2\Omega}\Bigg[&-\sigma - \frac{3}{4}r^2 + \frac{\bar{\gamma}^2}{4} + \frac{\sigma^2}{4\Omega^2} + \frac{\lambda^2}{6\Omega^2} + \frac{3}{8}\bar{\gamma}\bar{\eta}r^2 + \frac{11}{128}\bar{\eta}^2 r^4 \\ &+ \frac{51}{128\Omega^2}r^4 + \frac{3\sigma}{4\Omega^2}r^2 + \frac{\lambda^2}{4\Omega^2}\cos 2\phi \\ &- \frac{\bar{F}_0}{16\Omega^2 r}\cos(\vartheta-\phi)\left[9r^2 + 4(\sigma - 4\Omega^2)\right] \\ &- \frac{\bar{F}_0}{16\Omega r}\sin(\vartheta-\phi)\left(4\bar{\gamma} + 5\bar{\eta}r^2\right)\Bigg]. \end{aligned} \tag{II.35}$$

The frequency response of the oscillator is found by setting $\dot{r} = \dot{\phi} = 0$ in Eqs. (II.34) and (II.35) and numerically solving them with respect to r and ϕ. The highest power in r appearing in this system of equations is of fifth order, similarly to the result for the first lobe [see Eq. (II.25)], which is of fifth order in $|\bar{X}|^2$. The resulting frequency response, displaying at most five branches for a given frequency Ω, is qualitatively similar to the one obtained for the first instability lobe [cf. Fig. II.6]. We will thus desist from showing the resulting responses with a new figure. For small values of λ pertaining to the stable regime, the response is Duffing-like, see Fig. II.4(a). For larger values of λ beyond the instability boundary the response radically changes and the double hysteresis becomes possible, see Fig. II.4(b).

II.8 Other nonlinearities

So far we have focused on specific nonlinearities affecting the dynamics of our system [see Eq. (II.18)]. However, the EOM of a general nonlinear system could contain additional nonlinear terms other than the cubic (Duffing) nonlinearity and the nonlinear damping. We consider here

the effect of nonlinear terms, constraining ourselves to terms of order not higher than the third. We thus add to our system all the missing combinations of cubic and quadratic terms, i.e. $\dot{x}^3$, $x\dot{x}^2$, x^2, $x\dot{x}$ and $\dot{x}^2$. This leads to the following EOM

$$m\ddot{x} + \gamma\dot{x} + m\omega_0^2\left(1 - \lambda\cos\omega_p t\right)x + \alpha x^3 + \eta x^2\dot{x} + \kappa x^2 + \mu x\dot{x} + \rho\dot{x}^2 + \nu x\dot{x}^2 + \xi\dot{x}^3 = F_0\cos\omega_f t. \tag{II.36}$$

By redefining time and length like we did in Sec. II.3, we can rewrite this equation in dimensionless form as

$$\ddot{z} + \bar{\gamma}\dot{z} + z^3 + \bar{\eta}z^2\dot{z} + (1 - \lambda\cos 2\Omega\tau)\,z + \bar{\kappa}z^2 + \bar{\mu}z\dot{z} + \bar{\rho}\dot{z}^2 + \bar{\nu}z\dot{z}^2 + \bar{\xi}\dot{z}^3 = \bar{F}_0\cos(\Omega\tau + \vartheta), \tag{II.37}$$

where we have focused again on the degenerate case $\omega_p = 2\omega$ and $\omega_f = \omega$, with $\omega \approx \omega_0$ and allowed for a phase difference ϑ between the two drives. The new dimensionless parameters are defined as $\bar{\kappa} \equiv \kappa/\omega_0\sqrt{m\alpha}$, $\bar{\mu} \equiv \mu/\sqrt{m\alpha}$, $\bar{\rho} \equiv \rho\omega_0/\sqrt{m\alpha}$, $\bar{\nu} \equiv \nu\omega_0^2/\alpha$ and $\bar{\xi} \equiv \xi\omega_0^3/\alpha$; the old ones are the same used in Eq. (II.19). We proceed as before by recasting Eq. (II.37) into the form (II.20) and (II.21), where $f(z, y, \tau)$ is now given by

$$f(z, y, \tau) = -\sigma z - \bar{\gamma}y - z^3 - \bar{\eta}z^2 y + \lambda\cos(2\Omega\tau)z - \bar{\kappa}z^2 - \bar{\mu}zy - \bar{\rho}y^2 - \bar{\nu}zy^2 - \bar{\xi}y^3 + \bar{F}_0\cos(\Omega\tau + \vartheta). \tag{II.38}$$

Here we introduced again the detuning parameter $\sigma = 1 - \Omega^2$. First order averaging and a careful regrouping of the terms reveal that the new terms do not fundamentally change the response of the system; rather they merely lead to a renormalization of the old nonlinear coefficients [cf. Eq. (II.19)]. The EOMs for the slow flow variables u and v, to first order averaging, are given by

$$\dot{u} = -\frac{1}{2\Omega}\left[\bar{\gamma}\Omega u + v\left(\sigma + \frac{\lambda}{2}\right) + \frac{3}{4}\bar{\alpha}_{\text{eff}}(u^2 + v^2)v + \Omega\frac{\bar{\eta}_{\text{eff}}}{4}(u^2 + v^2)u - \bar{F}_0\sin\vartheta\right], \tag{II.39}$$

$$\dot{v} = -\frac{1}{2\Omega}\left[\bar{\gamma}\Omega v + u\left(-\sigma + \frac{\lambda}{2}\right) - \frac{3}{4}\bar{\alpha}_{\text{eff}}(u^2 + v^2)u + \Omega\frac{\bar{\eta}_{\text{eff}}}{4}(u^2 + v^2)v + \bar{F}_0\cos\vartheta\right], \tag{II.40}$$

where $\bar{\alpha}_{\text{eff}} \equiv 1 + \Omega^2\bar{\nu}/3$ and $\bar{\eta}_{\text{eff}} \equiv \bar{\eta} + 3\bar{\xi}\Omega^2$. Note that this equations have exactly the same form of (II.23) and (II.24). The effect of the new terms is indeed fully absorbed into the renormalized coefficients $\bar{\alpha}_{\text{eff}}$ and $\bar{\eta}_{\text{eff}}$. Note also that only the two cubic terms $\dot{x}^3$ and $x\dot{x}^2$ appear in the first order result. The quadratic, symmetry-breaking[5], terms x^2, $x\dot{x}$ and $\dot{x}^2$ yield no contribution to first order averaging: even though they are of $\mathcal{O}(\varepsilon)$ their contribution starts at $\mathcal{O}(\varepsilon^2)$. Second order averaging unveils the effect of the remaining nonlinear terms and confirms what we concluded from the first order results. The effect of the new nonlinear terms can be incorporated into the previous nonlinearities, which are discussed in Sec. II.2, resulting in $\bar{\alpha}_{\text{eff}} = \bar{\alpha}_{\text{eff}}(\bar{\nu}, \bar{\xi}, \bar{\kappa}, \bar{\mu}, \bar{\rho})$ and $\bar{\eta}_{\text{eff}} = \bar{\eta}_{\text{eff}}(\bar{\eta}, \bar{\nu}, \bar{\xi})$. The explicit expressions for the second order corrections and the renormalized coefficients are too cumbersome and will not be shown here. To conclude, the addition of other nonlinear terms does not change the response of the system in any qualitative way. Its frequency-response is thus similar to the ones shown in Fig. II.4. The exact form, or even the bending direction, will however depend on the resulting values of the effective nonlinearities.

II.9 Conclusion and discussion

Nonlinearities naturally emerge in many physical systems and become ineluctable as the system size scales down. We have developed a force detection scheme that explicitly benefits from the nonlinearities. There is here a change of paradigm: the nonlinearities are no longer avoided, rather we take advantage of their interplay with parametric driving. In this chapter we uncover the details and mechanism behind our method for hysteretic force detection. In summary, the scheme exploits the peculiar double-hysteretic response of the nonlinear system, which is closely linked to a symmetry breaking between the phase states of the unforced oscillator. Recently, A. Eichler *et al.* [94] extended our work by adding intrinsic as well as readout noise to the nonlinear resonator. They proposed a parametric symmetry breaking transducer (PSBT) and showed that its performance is notably robust against readout noise. We thus believe that the proposed force detection scheme is particularly promising for experiments with MEMS and NEMS.

[5]The cubic terms preserve the symmetry between x and $-x$, while the quadratic terms break this symmetry.

We emphasize that the relevance of the simple model studied in this chapter is of rather general nature and goes way beyond the mechanical domain. We hence expect that the results we obtained and the conclusions we drawn will apply to all those systems that can be modeled by a driven nonlinear oscillator. One such example is the fundamental mode of a doubly clamped beam resonator, which is nothing but the system we used to experimentally demonstrate the existence of the double-hysteretic phenomenon. Besides this example, which is directly related to our work, its importance permeates into the real materials. In recent years, major technological advances led indeed to the possibility of observing nonlinear responses, which predominantly pertained to classical mechanical systems, in various crystals [95–97]. It has been possible, for instance, to observe the nonlinear response of optical phonons in Si-C using femtosecond laser pulses [95]. In this and other materials the behavior of the phonon fluctuation coordinate is described by an EOM similar to the one of the nonlinear PO studied in our work [see Eq. (II.18)]. We thus believe that the physics described in this chapter will apply to the description of phonon modes in such materials.

Particular appealing applications could extend to the area of strongly correlated materials, where the strong interactions between charge, spin, orbital, and lattice degrees of freedom (phonons) are key to the formation of a wide class of phenomena. These include, to name a few, charge-ordered phases, colossal magnetoresistance, ferroelectricity, half-metallicity, and more [98]. The phenomena observed in this chapter could be used in some of those systems where the nonlinear phononics is activated and controlled using strong lasers. It would be highly interesting to study if the rich behavior of the nonlinear system studied here manifests in real materials and what their effect on electronic correlations would be.

We remark that a field that has been partially probed during the past few years is the one of superconductivity, where transient superconductivity has been induced by engineering interesting nonlinear phononics dynamics [99]. Coherent interlayer transport in $YBa_2Cu_3O_{6+x}$ has been induced up to room temperature [100] and non-equilibrium high-temperature superconductivity has been reported in K_3C_{60} [101]. In the near future we expect that technological advances could lead to tunable materials via appropriate driving protocols.

An interesting future direction of research include the investigation

of the quantum analog of the present system subject to quantum fluctuations. This is achieved by coupling the system to a thermal reservoir. Important concepts like quantum heating, leading to quantum activation, and fluctuation-induced switching [102] are certainly intriguing in the present complex landscape, in which up to three coexisting stable states exist. These phenomena could be studied, for instance, within the framework developed by M. Dykman, see [61, 88, 102] and references therein.

III

Periodically driven and dissipative Dicke model

Great works are performed, not by strength, but by perseverance.

Samuel Johnson

A natural extension of the JC model discussed in the Introduction (cf. Sec. I.1.4) consists in filling the optical cavity with an ensemble of two-level atoms that couple identically to the quantized cavity mode. This model was introduced in the mid 1950s by R. H. Dicke [20] and is nowadays a paradigmatic example of collective behavior in light-matter systems [103, 104]. Later, in the 1970s Hepp and Lieb [105] showed that, in the thermodynamic limit, this system undergoes a continuous classical phase transition. Though, the system also admits a quantum phase transition (QPT) at a critical value of the atom-field coupling [106, 107].

The DM and its superradiant phase transition have been subject of intense experimental investigations [108–117]. The model is still of topical interest due to the possibility of realizing it in systems other than the original cavity QED setup. Two main approaches have been proposed in the last decade to realize an effective Dicke model in an open system scenario. Dimer *et al.* [118] considered a 4-level scheme, in which the atoms couple to the cavity through stimulated Raman emissions. Alternatively, Domokos and Ritsch [119] studied thermal atoms in an optical

cavity. When the intensity of the external pumping laser reaches a critical strength the atoms self-organize in a checkerboard pattern (see also Sec. IV). It is only in recent times that the Dicke phase transition has been experimentally realized [37] following the proposal advanced by Nagy *et al.* [120]. A light-matter coupling strong enough to trigger this transition has been achieved in a system formed by a BEC coupled to an optical cavity.

In this chapter we investigate the effect of parametric driving on the dissipative Dicke model. It was shown by Bastidas *et al.* [121] that the closed-system DM with parametric driving of the light-matter coupling displays a very rich nonequilibrium phase diagram. It hosts indeed a set of new nonequilibrium normal-superradiant QPTs. On the other hand, Chitra and Zilberberg [21] considered the effect of this periodic modulation on the open-system DM and they found that in addition to the normal phase (NP) and superradiant phase (SP), a new phase with pulsed superradiance exists in this nonequilibrium sysyem. The novel phase is called dynamical normal phase (D-NP) and emerges as a parametric instability of the driven NP. The present study is mostly inspired by the latter work. In the present chapter we want to build on this results and investigate the driven NP with special focus on its boundary with the D-NP.

The physics of closed quantum many-body systems as well as open, but at or near equilibrium, is well established. Fields such as quantum statistical physics offer powerful tools for their analysis [122, 123]. On the contrary, we are just starting to grasp the basic principles of nonequilibrium phenomena and nonequilibrium phase transitions. An attractive and controlled way of reaching far-from-equilibrium conditions is achieved by introducing a parametric modulation of one of the system parameters. The phase diagram found in Ref. [21] under the said conditions has been worked out within the framework of mean-field theory. To this end we will construct an effective Hamiltonian describing the linear fluctuations on top of the aforementioned mean-field solution. The far-from-equilibrium physics of the open system is probed using an EOM approach and a closed form formal solution for its dynamics is derived. Dissipation is treated in an exact manner, and not within the standard paradigm for dissipative systems, that is using the common Lindblad equation. This choice is motivated by the fact that in a periodically driven system thermal fluctuations may be time dependent

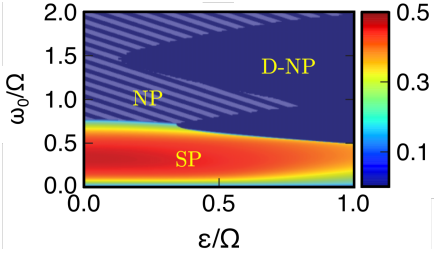

Figure III.1: Illustration of the nonequilibrium phase diagram of the parametrically driven Dicke model as a function of the atomic (or cavity) frequency, $\omega_c = \omega_a \equiv \omega_0$ [see Eq (III.1)] and parametric modulation strength ϵ. The values of the static coupling, λ_0, and dissipation rate are fixed, see [21]. Adapted from Ref. [21].

and hence their effect may not be correctly captured by static dissipation rates.

The chapter is structured as follows. In Sec. III.1 we briefly introduce the DM and pave the road for the investigation of the periodically driven and dissipative model, which we introduce in Sec. III.2. Using the equation-of-motion formalism we compute, in Sec. III.3, the time evolution of the system. Sec. III.4 is a sort of standalone part that motivates the developed EOM approach. The said technique allows us to determine the time evolution of several observables, which are presented in Sec. III.5. We also provide a comparison with the DM under the commonly used rotating wave approximation (RWA) in Sec. III.6. To conclude, we provide in Sec. III.7 a short summary and a final perspective of future possible directions of research.

The contents of this chapter are largely included in Reference [42].

III.1 The Dicke model

The DM [20] describes the interaction of N two-level systems cooperatively interacting with a single quantized mode of the radiation field. The Dicke Hamiltonian (setting $\hbar = 1$) reads

$$\hat{H}_S = \omega_c \hat{a}^\dagger \hat{a} + \omega_a \hat{J}_z + \frac{\lambda}{\sqrt{N}} (\hat{a}^\dagger + \hat{a}) (\hat{J}_+ + \hat{J}_-), \tag{III.1}$$

where ω_c is the frequency of the cavity mode, ω_a the atomic transition frequency and λ the light-matter coupling constant. The annihilation and creation operators of the photon mode are denoted by $\hat{a}$ and $\hat{a}^\dagger$, while the atoms are described by means of the collective operator $\hat{J}_k$, $k \in \{z, +, -\}$ [20]. Explicitly, they are given by

$$\hat{J}_\pm = \sum_{i=1}^{N} \hat{J}_\pm^{(i)} \quad \text{and} \quad \hat{J}_z = \sum_{i=1}^{N} \hat{J}_z^{(i)},$$

and satisfy the usual commutation relations[1] for angular momentum operators $[\hat{J}_+, \hat{J}_-] = 2\hat{J}_z$ and $[\hat{J}_z, \hat{J}_\pm] = \pm\hat{J}_\pm$. The ensemble of N two-level atoms is thus represented as a single $(2j+1)$ level system, i.e. a giant pseudospin[2]. The index j is the so-called Dicke's cooperation number.

The conserved parity $\hat{\Pi}$ associated with the DM, that is $[\hat{H}_S, \hat{\Pi}] = 0$, is given by

$$\hat{\Pi} = \exp\{i\pi\hat{N}\},$$

where $\hat{N} = \hat{a}^\dagger\hat{a} + \hat{J}_z + j$ is number operator related to the total number of excitation quanta in the system. Note that, depending on the value taken by $\hat{N}$, the parity $\hat{\Pi}$ will result in either +1 or -1. The Hamiltonian (III.1) possesses indeed a discrete $\mathbb{Z}_2$ symmetry associated with a change of sign of $\hat{a}$ and $\hat{J}_x$:

$$\hat{\Pi} : \ (\hat{a}, \hat{J}_x) \to \hat{\Pi}(\hat{a}, \hat{J}_x)\hat{\Pi}^\dagger = (-\hat{a}, -\hat{J}_x).$$

The discrete symmetry of the DM can be spontaneously broken, at zero temperature, at a critical value of the atom-field coupling $\lambda_c = \sqrt{\omega_c\omega_a}/2$. At this critical point the system undergoes a $\mathbb{Z}_2$-symmetry breaking QPT from a NP (for $\lambda < \lambda_c$) to a SP (for $\lambda > \lambda_c$), in which the ground state of the system displays a macroscopic occupation of the cavity mode and the atomic excited states are populated.

In this chapter we follow the approach of Emary and Brandes [107]. We restrict our attention to the sector of maximal pseudospin $j = N/2$ and introduce a Holstein-Primakoff representation [124] for the angular

[1] The commutator of two operators $\hat{a}$ and $\hat{b}$ is defined as $[\hat{a}, \hat{b}] = \hat{a}\hat{b} - \hat{b}\hat{a}$.

[2] The quantum number j, known as cooperation number, gives the maximal value of the angular momentum that is here fixed to $j = N/2$. Since $[\hat{H}_S, \hat{J}^2] = 0$, this value of the spin is conserved.

momentum algebra[3] in terms of bosonic operators $\hat{b}$, $\hat{b}^\dagger$. In the thermodynamic limit ($N \to \infty$) the present light-matter system turns into a so-called *giant quantum harmonic oscillator* problem [125]. The bosonized Hamiltonian, valid in the NP, obtained using the Holstein-Primakoff transformation (III.2) reads

$$\hat{H}_S = \omega_c \hat{a}^\dagger \hat{a} + \omega_a \hat{b}^\dagger \hat{b} + \lambda \left(\hat{a}^\dagger + \hat{a}\right)\left(\hat{b}^\dagger + \hat{b}\right). \tag{III.3}$$

This is the Hamiltonian of two coupled quantum HOs, one associated with the cavity field and the other with the pseudospin. Note that the effective Hamiltonian (III.3) describes the fluctuations about the vacuum cavity state and unexcited atoms. As such, it is only valid in the NP. Similarly, for the SP another effective Hamiltonian describing the fluctuations about the mean-field, or semiclassical, amplitudes can be found [107]. In this representation the total number of excitations is $\hat{N} = \hat{a}^\dagger \hat{a} + \hat{b}^\dagger \hat{b}$ and hence the parity operator is given by $\hat{\Pi} = \exp\{i\pi(\hat{a}^\dagger \hat{a} + \hat{b}^\dagger \hat{b})\}$.

III.2 The modulated Dicke model

The system under study is an ensemble of N two-level atoms interacting through dipole interaction with a single bosonic cavity mode. We consider here the atom-field coupling strength to be time-periodic. The Hamiltonian of the system has the following form (we set again $\hbar = 1$)

$$\hat{H}_S(t) = \omega_c \hat{a}^\dagger \hat{a} + \omega_a \hat{J}_z + \frac{\lambda(t)}{\sqrt{N}}\left(\hat{a}^\dagger + \hat{a}\right)\left(\hat{J}_+ + \hat{J}_-\right), \tag{III.4}$$

where the time-dependent coupling strength is a periodic function of the form $\lambda(t) = \lambda_0 + \epsilon \cos(2\Omega t)$. The phase diagram of the system described by the Hamiltonian (III.4) was studied within the framework of mean-field theory in Ref. [21] and is shown in Fig. III.1. The nonequilibrium phase diagram of the model displays three phases: NP, SP and D-NP. The latter emerges as a manifestation of parametric resonance. In this

[3] The Holstein-Primakoff representation can be used to write the components of the angular momentum operator $\hat{J}$ in terms of bosonic annihilation and creation operators $\hat{b}$, $\hat{b}^\dagger$. The operators $\hat{J}_k$, with $k \in \{z, +, -\}$, appearing in Eq. (III.4) can be expressed as

$$\hat{J}_+ = \hat{b}^\dagger \sqrt{N - \hat{b}^\dagger \hat{b}}, \quad \hat{J}_- = \sqrt{N - \hat{b}^\dagger \hat{b}}\, \hat{b}, \quad \hat{J}_z = \hat{b}^\dagger \hat{b} - N/2. \tag{III.2}$$

The operators $\hat{b}$, $\hat{b}^\dagger$ satisfy the standard commutation relations $[\hat{b}, \hat{b}^\dagger] = 1$.

work, we want to study how the instability of the NP to both the SP and the D-NP occurs. For this reason, in what follows we will focus on the driven NP. Using the standard Holstein-Primakoff representation [124] for the angular momentum algebra in terms of bosonic operators $\hat{b}$, $\hat{b}^\dagger$ and considering the thermodynamic limit ($N \to \infty$), leads to the following bosonized (exact) Hamiltonian for the driven normal phase[4]

$$\hat{H}_S(t) = \omega_c \hat{a}^\dagger \hat{a} + \omega_a \hat{b}^\dagger \hat{b} + \lambda(t)\left(\hat{a}^\dagger + \hat{a}\right)\left(\hat{b}^\dagger + \hat{b}\right). \tag{III.5}$$

The problem is thus reduced to the one of two harmonic oscillators with time-dependent coupling. Notice that, since we are not treating the atom-field coupling in the usual RWA, we are not bound to the weak-coupling regime[5].

The system described by Eq. (III.5) is coupled to two general baths modeled by a collection of harmonic oscillators. The two thermal baths are introduced to describe the cavity as well as the atomic dissipation. We consider in this work a global coupling bath, i.e. the case in which all the atoms couple to a single thermal bath. For the sake of methodological convenience, the two baths are taken to be independent but equal in detail; the main features of our results should also hold for inequivalent baths. The Hamiltonian of the total system reads

$$\hat{H}(t) = \hat{H}_S(t) + \hat{H}_B + \hat{H}_I,$$

where $\hat{H}_S(t)$ is given by Eq. (III.5) and

$$\begin{aligned} \hat{H}_B &= \hat{H}_{B_1} + \hat{H}_{B_2} \\ &= \sum_k \omega_k \hat{c}_k^\dagger \hat{c}_k + \sum_i \omega_i \hat{d}_i^\dagger \hat{d}_i, \end{aligned} \tag{III.6}$$

$$\begin{aligned} \hat{H}_I = &\sum_k g_k (\hat{a}^\dagger + \hat{a})(\hat{c}_k^\dagger + \hat{c}_k) \\ &+ \sum_i g_i (\hat{b}^\dagger + \hat{b})(\hat{d}_i^\dagger + \hat{d}_i), \end{aligned} \tag{III.7}$$

are the Hamiltonians of the two environments and their interaction with the system. The operators $\hat{c}_k$ and $\hat{c}_k^\dagger$ (resp. $\hat{d}_i$ and $\hat{d}_i^\dagger$) are the annihilation

[4] Upon entering the D-NP the derived effective Hamiltonian breaks down because, as was shown in Ref. [21], the system acquires a finite order parameter.

[5] The RWA is an approximation commonly used in quantum optics, in which the fast-oscillating terms in the Hamiltonian are neglected. It is often used to simplify problems and obtain analytic approximate solutions. Its validity is however bound to the weak-coupling regime.

and creation operators of the first (resp. second) bath, while g_k (resp. g_i) describes the interaction strength between the cavity (resp. the atoms) and the environments.

The present total system is decoupled by the introduction of normal modes (NMs), see Appendix A. In the present work we shall consider the case in which the frequencies of the cavity field and the level spacing of the atomic ensemble are identical, i.e. $\omega_c = \omega_a \equiv \omega_0$. The NM operators are then given by

$$\begin{aligned}\hat{A}_1 &= \frac{1}{\sqrt{2}}\left[S_1^+(\hat{a}+\hat{b}) + S_1^-(\hat{a}^\dagger+\hat{b}^\dagger)\right],\\ \hat{A}_2 &= \frac{1}{\sqrt{2}}\left[S_2^+(\hat{a}-\hat{b}) + S_2^-(\hat{a}^\dagger-\hat{b}^\dagger)\right],\end{aligned} \tag{III.8}$$

where $S_i^\pm = (\Omega_i \pm \omega_0)/(2\sqrt{\omega_0\Omega_i})$ [21, 126] and the NM frequencies are

$$\Omega_{1,2}^2(t) = \omega_0^2 \pm 2\lambda_0\omega_0 \pm 2\omega_0\epsilon\cos(2\Omega t). \tag{III.9}$$

The Hamiltonian of the uncoupled system, which consists of two POs [121], reads

$$\begin{aligned}\hat{H}_{\tilde{S}}(t) = \Omega_1(t)\big(\hat{A}_1^\dagger(t)\hat{A}_1(t) + 1/2\big)\\ + \Omega_2(t)\big(\hat{A}_2^\dagger(t)\hat{A}_2(t) + 1/2\big).\end{aligned} \tag{III.10}$$

Depending on the drive frequency, the two POs can exhibit parametric resonance and the instability lobe structures of the Mathieu oscillator discussed in Chpt. II. We now explicitly study the role of the baths. The environment and interaction Hamiltonians are transformed to

$$\begin{aligned}\hat{H}_{\tilde{B}} &= \hat{H}_{\tilde{B}_1} + \hat{H}_{\tilde{B}_2}\\ &= \sum_k \omega_k \hat{C}_k^\dagger\hat{C}_k + \sum_i \omega_i \hat{D}_i^\dagger\hat{D}_i,\end{aligned} \tag{III.11}$$

$$\begin{aligned}\hat{H}_{\tilde{I}}(t) = \sum_k \tilde{g}_k(t)\big(\hat{A}_1^\dagger(t) + \hat{A}_1(t)\big)\big(\hat{C}_k^\dagger + \hat{C}_k\big)\\ + \sum_i \tilde{g}_i(t)\big(\hat{A}_2^\dagger(t) + \hat{A}_2(t)\big)\big(\hat{D}_k^\dagger + \hat{D}_k\big),\end{aligned} \tag{III.12}$$

where $\tilde{g}_k(t) \equiv g_k\sqrt{\omega_0/\Omega_1(t)}$ and $\tilde{g}_i(t) \equiv g_i\sqrt{\omega_0/\Omega_2(t)}$. The relation between the real baths operators c_k, d_k and the NM operators $\hat{C}_k, \hat{D}_k$ is given by $\hat{C}_k = \frac{1}{\sqrt{2}}(\hat{c}_k + \hat{d}_k)$ and $\hat{D}_k = \frac{1}{\sqrt{2}}(\hat{c}_k - \hat{d}_k)$. Note that for the

system Hamiltonian both the NM frequencies and operators are now explicitly *time dependent*. We also want to point out that the interaction Hamiltonian, which initially was time-independent [cf. Eq. (III.7)], acquires now an explicit time dependence. This differs from previous works dealing with POs interacting with environments through a static interaction Hamiltonian [127, 128]. We note also that in the past the Feynman-Vernon influence functional formalism [129] has been used to investigate the dynamics of a single PO [127]. Here, we decided to use a simpler formalism based on the Heisenberg EOMs.

III.3 Time evolution

Typically, open systems are studied within the framework of density matrices and dissipation is treated in an approximate way. In the present investigation, instead of an approximate master equation for the reduced density matrix, we use the equation-of-motion approach to solve for the dynamics of the system plus reservoir. In this way, we can avoid possible pitfalls peculiar to time-dependent systems. Equations (III.10)-(III.12) show that in the NM picture each of the two POs only interacts with one of the two (NM) baths. We thus focus here on a single NM oscillator coupled to a NM reservoir.

In what follows, we investigate the time evolution of the first NM, but the very same procedure applies to the second one. For the sake of simplicity, we write its frequency as $\Omega_1(t) = \sqrt{\omega_0^2 + \phi(t)}$, cf. Eq. (III.9). The Heisenberg EOM[6] for the operators $\hat{A}_1$ and $\hat{C}_k$ read

$$\dot{\hat{A}}_1(t) = -i\Omega_1(t)\hat{A}_1 + \frac{\dot{\phi}(t)}{4\Omega_1^2(t)}\hat{A}_1^\dagger - i\sum_k \tilde{g}_k(t)\big(\hat{C}_k^\dagger + \hat{C}_k\big), \tag{III.13}$$

$$\dot{\hat{C}}_k(t) = -i\omega_k\hat{C}_k - i\tilde{g}_k(t)\big(\hat{A}_1^\dagger + \hat{A}_1\big). \tag{III.14}$$

We can remove the bath operators from the Eq. (III.13) – obtaining an effective time evolution equation for the operator $\hat{A}$ in terms of $\hat{C}_k(0)$ and $\hat{C}_k^\dagger(0)$ – by means of the formal solution of Eq. (III.14), which is given by

$$\hat{C}_k(t) = \hat{C}_k(0)\mathrm{e}^{-i\omega_k t} - i\int_0^t \tilde{g}_k(\tau)\big[\hat{A}_1(\tau) + \hat{A}_1^\dagger(\tau)\big]\mathrm{e}^{-i\omega_k(t-\tau)}\mathrm{d}\tau.$$

[6] In the Heisenberg picture, the time evolution of an operator $\hat{\mathcal{O}}$ is governed by the equation: $\frac{\mathrm{d}}{\mathrm{d}t}\hat{\mathcal{O}} = i[\hat{H}, \hat{\mathcal{O}}] + \frac{\partial}{\partial t}\hat{\mathcal{O}}$, which is known as the Heisenberg EOM.

Plugging it into Eq. (III.13) gives the following equation for the time evolution of the operator A_1

$$\dot{\hat{A}}_1(t) = -i\Omega_1(t)\hat{A}_1 + \frac{\dot{\phi}(t)}{4\Omega_1^2(t)}\hat{A}_1^\dagger - i\sum_k \tilde{g}_k(t)\left[\hat{C}_k(0)\mathrm{e}^{-i\omega_k t} + \hat{C}_k^\dagger(0)\mathrm{e}^{i\omega_k t}\right] - \frac{\omega_0}{\sqrt{\Omega_1(t)}}\int_0^t \frac{K(t-\tau)}{\sqrt{\Omega_1(\tau)}}\left[\hat{A}_1(\tau) + \hat{A}_1^\dagger(\tau)\right]\mathrm{d}\tau, \tag{III.15}$$

where $K(t) \equiv -2i\sum_k g_k^2 \sin(\omega_k t)$ is the memory kernel. The linearity of Eq. (III.15) implies a solution of the form [130]

$$\hat{A}_1(t) = G(t)\hat{A}_1(0) + L^*(t)\hat{A}_1^\dagger(0) + \hat{F}(t). \tag{III.16}$$

The time-dependent functions $G(t)$ and $L(t)$ are determined by the following integro-differential equations

$$\dot{G}(t) = -i\Omega_1(t)G(t) + \frac{\dot{\phi}(t)}{4\Omega_1^2(t)}L(t) - \frac{\omega_0}{\sqrt{\Omega_1(t)}}\int_0^t \frac{K(t-\tau)}{\sqrt{\Omega_1(\tau)}}\left[G(\tau) + L(\tau)\right]\mathrm{d}\tau, \tag{III.17}$$

$$\dot{L}(t) = i\Omega_1(t)L(t) + \frac{\dot{\phi}(t)}{4\Omega_1^2(t)}G(t) + \frac{\omega_0}{\sqrt{\Omega_1(t)}}\int_0^t \frac{K(t-\tau)}{\sqrt{\Omega_1(\tau)}}\left[G(\tau) + L(\tau)\right]\mathrm{d}\tau, \tag{III.18}$$

with initial conditions $G(0) = 1$ and $L(0) = 0$. Similarly, the operator $F(t)$ is determined by

$$\dot{\hat{F}}(t) = -i\Omega_1(t)\hat{F}(t) + \frac{\dot{\phi}(t)}{4\Omega_1^2(t)}\hat{F}^\dagger(t) - i\sum_k \tilde{g}_k(t)\left[\hat{C}_k(0)\mathrm{e}^{-i\omega_k t} + \hat{C}_k^\dagger(0)\mathrm{e}^{i\omega_k t}\right] - \frac{\omega_0}{\sqrt{\Omega_1(t)}}\int_0^t \frac{K(t-\tau)}{\sqrt{\Omega_1(\tau)}}\left[\hat{F}(\tau) + \hat{F}^\dagger(\tau)\right]\mathrm{d}\tau. \tag{III.19}$$

Using a Green's function approach [122, 130, 131], the solution of the last equation can be written as (see Appendix B)

$$\hat{F}(t) = \int_0^t \left[\Lambda_1(t,t') + \Lambda_2^*(t,t')\right]\sum_k \tilde{g}_k(t')\left[\hat{C}_k(0)\mathrm{e}^{-i\omega_k t'} + \hat{C}_k^\dagger(0)\mathrm{e}^{i\omega_k t'}\right]\mathrm{d}t'. \tag{III.20}$$

The two functions $\Lambda_1(t,t')$ and $\Lambda_2(t,t')$ are determined, for fixed t', by the following equations

$$\dot{\Lambda}_1(t,t') = -i\Omega_1(t)\Lambda_1(t,t') + \frac{\dot{\phi}(t)}{4\Omega_1^2(t)}\Lambda_2(t,t') - \frac{\omega_0}{\sqrt{\Omega_1(t)}}\int_{t'}^{t}\frac{K(t-s)}{\sqrt{\Omega_1(s)}}\big[\Lambda_1(s,t') + \Lambda_2(s,t')\big]\mathrm{d}s\,, \tag{III.21}$$

$$\dot{\Lambda}_2(t,t') = \frac{\dot{\phi}(t)}{4\Omega_1^2(t)}\Lambda_1(t,t') + i\Omega_1(t)\Lambda_2(t,t') + \frac{\omega_0}{\sqrt{\Omega_1(t)}}\int_{t'}^{t}\frac{K(t-s)}{\sqrt{\Omega_1(s)}}\big[\Lambda_1(s,t') + \Lambda_2(s,t')\big]\mathrm{d}s\,, \tag{III.22}$$

with the initial conditions $\Lambda_1(t,t) = -i$ and $\Lambda_2(t,t) = 0$. The time evolution of the initial coupled system described by Eqs. (III.5)-(III.7) is computed as follows. We first study the NMs, whose time evolution is fully determined by the Eqs. (III.16)-(III.22). Any physical observable, in the NM picture, can be found from Eq. (III.16) by taking the appropriate expectation values. Lastly, we can use the NM transformation shown in Eq. (III.8) to return to the original system. Since the full time evolution of the operators are now known, we can calculate both equal and unequal time correlations using this formalism.

In what follows we assume that the system and the reservoir are *initially uncorrelated*. For example, under this assumption, the time evolution of the expectation value of the NM occupation number $N_1(t) \equiv \langle \hat{A}_1^\dagger(t)\hat{A}_1(t)\rangle$, is given by[7]

$$N_1(t) = \big(|G(t)|^2 + |L(t)|^2\big)\langle \hat{A}_1^\dagger(0)\hat{A}_1(0)\rangle + |L(t)|^2 + 2\,\mathrm{Re}\left\{L(t)G(t)\langle \hat{A}_1(0)\hat{A}_1(0)\rangle\right\} + \langle \hat{F}^\dagger(t)\hat{F}(t)\rangle. \tag{III.23}$$

We further assume both baths to be in *thermal equilibrium* at the same temperature T, that is $\rho_{B_k}(0) = \exp(-\beta\hat{H}_{B_k})/\,\mathrm{Tr}\{\exp(-\beta\hat{H}_{B_k})\}$, with $\hat{H}_{B_k}$ given by Eq. (III.6) and $\beta = 1/k_BT$. In order to properly describe dissipation, and obtain irreversible dynamics, we further assume a *continuous distribution of bath modes*. Under these assumptions the bath correlation function for the first NM, given by $\langle \hat{F}^\dagger(t)\hat{F}(t)\rangle = \mathrm{Tr}\{\rho_{\tilde{B}_1}(0)\hat{F}^\dagger(t)\hat{F}(t)\}$,

[7] We have used here the canonical commutation relations for the NMs at $t = 0$. Using Eq. (III.8) it can be shown that they match the ones for the original operators $\hat{a}$ and $\hat{b}$ and read $[A_k, A_k^\dagger] = 1$, with $k = 1, 2$.

takes the following form (see Appendix B)

$$\langle \hat{F}^\dagger(t)\hat{F}(t)\rangle = \int_0^t \mathrm{d}t' \int_0^t \mathrm{d}t'' \frac{\omega_0 K_T(t'-t'')}{\sqrt{\Omega_1(t')\Omega_1(t'')}} \times \big[\Lambda_1^*(t,t') + \Lambda_2(t,t')\big]\big[\Lambda_1(t,t'') + \Lambda_2^*(t,t'')\big]. \quad \text{(III.24)}$$

Here $K_T(t)$ denotes the temperature-dependent noise kernel appearing in the Caldeira-Leggett model [132] and is given by

$$K_T(t) = \int_0^\infty J(\omega)\big[\coth(\beta\omega/2)\cos(\omega t) - i\sin(\omega t)\big]\mathrm{d}\omega, \quad \text{(III.25)}$$

where $J(\omega) \equiv \sum_k g_k^2 \delta(\omega - \omega_k)$ is the spectral density of the environmental coupling. We would like to stress the fact that for the later purpose of computing the entanglement between the atoms and the cavity mode we need *all* the NM correlation functions, not only $\langle \hat{A}_1^\dagger(t)\hat{A}_1(t)\rangle$ shown above. This also means that we need all the bath correlation functions, which in the present non-RWA treatment are all nonvanishing. This is in sharp contrast to the RWA case, where the only nonvanishing bath correlation functions are $\langle \hat{F}^\dagger(t)\hat{F}(t)\rangle$ and $\langle \hat{F}(t)\hat{F}^\dagger(t)\rangle$. We will provide further details later in Sec. III.6.

III.4 Non-Markovian master equation

In Sec. III.3 a significant effort has been made to properly deal with dissipation. Here we want to motivate this choice through a comparison with the standard Lindblad approach, which generally describes Markovian dynamics [133–136]. To this end we compute here the exact time-convolutionless (TCL) non-Markovian master equation [137–140] for the reduced density matrix of "our system". Since the two NM evolve independently (cf. Sec. III.3), we consider here as "our system" a single NM, i.e. a single PO. Note that in this section, instead of re-quantizing the system using the time-dependent NM frequency (cf. Appendix A), we define the latter operators with respect to the static model (i.e. $\phi(t) = 0$). The Hamiltonian of the system thus reads

$$\hat{H}_S(t) = \left(\omega_0 + \frac{\phi(t)}{2\omega_0}\right)\hat{a}^\dagger\hat{a} + \frac{\phi(t)}{4\omega_0}\left(\hat{a}^{\dagger 2} + \hat{a}^2\right), \quad \text{(III.26)}$$

while the bath and interaction Hamiltonians are as before [cf. Eqs. (III.6) and (III.7)].

The exact TCL non-Markovian master equation for the reduced density matrix of the system, $\hat{\rho}_S$, obtained after integrating out the baths degrees of freedom, has the following form:

$$\begin{aligned}\frac{\mathrm{d}}{\mathrm{d}t}\hat{\rho}_S(t) =& -i[\hat{H}_S(t)+\Delta\hat{H}_S(t),\hat{\rho}_S(t)]\\ &-\gamma_1(t)\big(\{\hat{a}^\dagger\hat{a},\hat{\rho}_S(t)\}-2\hat{a}\hat{\rho}_S(t)\hat{a}^\dagger\big)\\ &-\gamma_2(t)\big(\{\hat{a}\hat{a}^\dagger,\hat{\rho}_S(t)\}-2\hat{a}^\dagger\hat{\rho}_S(t)\hat{a}\big)\\ &-\gamma_3(t)\big(\{\hat{a}\hat{a},\hat{\rho}_S(t)\}-2\hat{a}\hat{\rho}_S(t)\hat{a}\big)\\ &-\gamma_3^*(t)\big(\{\hat{a}^\dagger\hat{a}^\dagger,\hat{\rho}_S(t)\}-2\hat{a}^\dagger\hat{\rho}_S(t)\hat{a}^\dagger\big),\end{aligned} \tag{III.27}$$

where $\Delta\hat{H}_S(t)=\Delta\omega(t)\hat{a}^\dagger\hat{a}+\Delta\phi^*(t)\hat{a}^{\dagger 2}+\Delta\phi(t)\hat{a}^2$ and $\{\cdot,\cdot\}$ denotes the anti-commutator[8]. The coefficients $\gamma_1(t)$ and $\gamma_2(t)$ commonly refer to dissipation and fluctuations due to back-reactions between system and bath, while $\gamma_3(t)$ relates to two-photon processes [135]. For the sake of shortness we only present here the final result for the TCL master equation for $\hat{\rho}_S$; further details can be found in the Appendix C.

The unknown parameters appearing in the TCL non-Markovian master equation (III.27) can be fixed through a comparison with the Heisenberg EOMs. Repeating the previous computations (cf. Sec. III.3) we get the following equations for the time evolution of $G(t)$ and $L(t)$

$$\begin{aligned}\dot{G}(t) =& -i\left(\omega_0+\frac{\phi(t)}{2\omega_0}\right)G(t)-i\frac{\phi(t)}{2\omega_0}L(t)\\ &-\int_0^t K(t-\tau)\big[G(\tau)+L(\tau)\big]\mathrm{d}\tau,\end{aligned} \tag{III.28}$$

$$\begin{aligned}\dot{L}(t) =& \;i\left(\omega_0+\frac{\phi(t)}{2\omega_0}\right)L(t)+i\frac{\phi(t)}{2\omega_0}G(t)\\ &+\int_0^t K(t-\tau)\big[G(\tau)+L(\tau)\big]\mathrm{d}\tau,\end{aligned} \tag{III.29}$$

with initial conditions $G(0)=1$ and $L(0)=0$. Similarly, the operator

[8]The anti-commutator of two operators $\hat{a}$ and $\hat{b}$ is defined as $\{\hat{a},\hat{b}\}=\hat{a}\hat{b}+\hat{b}\hat{a}$.

$F(t)$ is determined by

$$\begin{aligned}\dot{\hat{F}}(t) = &-i\left(\omega_0 + \frac{\phi(t)}{2\omega_0}\right)\hat{F}(t) - i\frac{\phi(t)}{2\omega_0}\hat{F}^\dagger(t)\\ &- i\sum_k g_k\left[\hat{c}_k(0)\mathrm{e}^{-i\omega_k t} + \hat{c}_k^\dagger(0)\mathrm{e}^{i\omega_k t}\right]\\ &- \int_0^t K(t-\tau)\left[\hat{F}(\tau) + \hat{F}^\dagger(\tau)\right]\mathrm{d}\tau. \end{aligned} \tag{III.30}$$

In order to determine the sought parameters we compute the dynamics of the physical observables $\langle\hat{a}\rangle$, $\langle\hat{a}^2\rangle$ and $\langle\hat{a}^\dagger\hat{a}\rangle$ using the Heisenberg EOMs and comparing the results to those of the master equation. We start with the former. From the Eq. (III.16), with the simple replacement $\hat{A}_1 \leftrightarrow \hat{a}$ for the present case, we see that

$$\begin{bmatrix} \hat{a}(0) \\ \hat{a}^\dagger(0) \end{bmatrix} = W^{-1}(t)\begin{bmatrix} G^*(t) & -L^*(t) \\ -L(t) & G(t) \end{bmatrix}\begin{bmatrix} \hat{a}(t) - \hat{F}(t) \\ \hat{a}^\dagger(t) - \hat{F}^\dagger(t) \end{bmatrix},$$

where we have defined $W(t) = |G(t)|^2 - |L(t)|^2$. This equation allows us to write $\dot{\hat{a}}(t)$ as

$$\dot{\hat{a}}(t) = \varphi(t)\left[\hat{a}(t) - \hat{F}(t)\right] + \chi(t)\left[\hat{a}^\dagger(t) - \hat{F}^\dagger(t)\right] + \dot{\hat{F}}(t),$$

where we have introduced the following parameters:

$$\begin{aligned}\varphi(t) &= \left[\dot{G}(t)G^*(t) - \dot{L}^*(t)L(t)\right]W^{-1}(t),\\ \chi(t) &= \left[\dot{L}^*(t)G(t) - \dot{G}(t)L^*(t)\right]W^{-1}(t).\end{aligned}$$

The expectation value of the bath operator, $\langle\hat{F}^{(\dagger)}\rangle$, vanishes in the general case of reservoir modes not in a coherent state, which implies that

$$\frac{\mathrm{d}}{\mathrm{d}t}\langle\hat{a}(t)\rangle = \varphi(t)\langle\hat{a}(t)\rangle + \chi(t)\langle\hat{a}^\dagger(t)\rangle. \tag{III.31}$$

Similarly, using Eq. (III.16) for $\hat{a}$ and Eq. (III.31) for $\dot{\hat{a}}$, we obtain the time evolution of $\hat{a}(t)\hat{a}(t)$ and $\hat{a}^\dagger(t)\hat{a}(t)$. Their expectation values are given by

$$\begin{aligned}\frac{\mathrm{d}}{\mathrm{d}t}\langle\hat{a}(t)\hat{a}(t)\rangle = &\,2\varphi(t)\left[\langle\hat{a}(t)\hat{a}(t)\rangle - \langle\hat{F}(t)\hat{F}(t)\rangle\right] + 2\chi(t)\langle\hat{a}^\dagger(t)\hat{a}(t)\rangle\\ &- \chi(t)\langle\hat{F}^\dagger(t)\hat{F}(t) + \hat{F}(t)\hat{F}^\dagger(t)\rangle + \frac{\mathrm{d}}{\mathrm{d}t}\langle\hat{F}(t)\hat{F}(t)\rangle + \chi(t),\end{aligned} \tag{III.32}$$

and

$$\frac{\mathrm{d}}{\mathrm{d}t}\langle\hat{a}^\dagger(t)\hat{a}(t)\rangle = \frac{\dot{W}(t)}{W(t)}\left[\langle\hat{a}^\dagger(t)\hat{a}(t)\rangle - \langle\hat{F}^\dagger(t)\hat{F}(t)\rangle\right] + \frac{\mathrm{d}}{\mathrm{d}t}\langle\hat{F}^\dagger(t)\hat{F}(t)\rangle + 2\,\mathrm{Re}\left\{\chi^*(t)\langle\hat{a}(t)\hat{a}(t)\rangle\right\} - 2\,\mathrm{Re}\left\{\chi^*(t)\langle\hat{F}(t)\hat{F}(t)\rangle\right\}. \tag{III.33}$$

On the other hand, the master equation (III.27) gives the following result for time evolution of $\langle\hat{a}(t)\rangle$:

$$\frac{\mathrm{d}}{\mathrm{d}t}\langle\hat{a}(t)\rangle = \mathrm{Tr}\{\hat{a}\frac{\mathrm{d}}{\mathrm{d}t}\hat{\rho}_S\} = -\langle\hat{a}\rangle\left[\gamma_1 - \gamma_2 + i\big(\omega_0 + \frac{\phi(t)}{2\omega_0} + \Delta\omega\big)\right] - 2i\langle\hat{a}^\dagger\rangle\Big(\frac{\phi(t)}{4\omega_0} + \Delta\phi^*\Big). \tag{III.34}$$

Similarly we obtain

$$\frac{\mathrm{d}}{\mathrm{d}t}\langle\hat{a}(t)\hat{a}(t)\rangle = -2\langle\hat{a}\hat{a}\rangle\left[\gamma_1 - \gamma_2 + i\big(\omega_0 + \frac{\phi(t)}{2\omega_0} + \Delta\omega\big)\right] - 2\gamma_3^* - 4i\langle\hat{a}^\dagger\hat{a}\rangle\Big(\frac{\phi(t)}{4\omega_0} + \Delta\phi^*\Big) - 2i\Big(\frac{\phi(t)}{4\omega_0} + \Delta\phi^*\Big). \tag{III.35}$$

and

$$\frac{\mathrm{d}}{\mathrm{d}t}\langle\hat{a}^\dagger(t)\hat{a}(t)\rangle = 2i\langle\hat{a}\hat{a}\rangle\Big(\frac{\phi(t)}{4\omega_0} + \Delta\phi\Big) - 2i\langle\hat{a}^\dagger\hat{a}^\dagger\rangle\Big(\frac{\phi(t)}{4\omega_0} + \Delta\phi^*\Big) - 2\langle\hat{a}^\dagger\hat{a}\rangle\big(\gamma_1 - \gamma_2\big) + 2\gamma_2. \tag{III.36}$$

A direct comparison of the Eqs. (III.31)-(III.36) leads to the following expressions for the parameters of the master equation (III.27):

$$\gamma_1(t) = \gamma_2(t) - \frac{\dot{W}(t)}{2W(t)},$$

$$2\gamma_2(t) = \frac{\mathrm{d}}{\mathrm{d}t}\langle F^\dagger(t)F(t)\rangle - \frac{\dot{W}(t)}{W(t)}\langle F^\dagger(t)F(t)\rangle - \chi^*(t)\langle F(t)F(t)\rangle - \chi(t)\langle F^\dagger(t)F^\dagger(t)\rangle,$$

$$2\gamma_3^*(t) = 2\varphi(t)\langle F(t)F(t)\rangle + 2\chi(t)\langle F^\dagger(t)F(t) + F(t)F^\dagger(t)\rangle - \frac{\mathrm{d}}{\mathrm{d}t}\langle F(t)F(t)\rangle,$$

$$\Delta\omega(t) = i\varphi(t) - i\frac{\dot{W}(t)}{2W(t)} - \omega_0 - \frac{\phi(t)}{2\omega_0},$$

$$\Delta\phi^*(t) = \frac{i}{2}\chi(t) - \frac{\phi(t)}{4\omega_0}.$$

For the PO defined in Eq. (III.26), the coefficients $\gamma_1(t)$, $\gamma_2(t)$ and $\gamma_3(t)$ are shown in Fig. III.2. We consider two values of the drive amplitude: one where the system is far from the parametric instability and the other where the system is close to the parametric instability (see e.g. stability lobes in Chpt. II). One can see that, even after many driving periods, the time-dependent coefficients of the TCL master equation (III.27) display an oscillatory behavior. This is in strong contrast with the standard Lindblad approach, where the dissipation rates appearing in the master equation are constants. Note also that the latter equation only contains terms in which creation and annihilation operators come in pairs, i.e. it only contains the terms proportional to γ_1 and γ_2 [cf. Eq. (III.27)]. The constant dissipation rates appearing in the Lindblad equation for both drive amplitudes are approximately given by $\gamma_1 \approx 0.001$ and $\gamma_2 \approx 0.0009$. At low drive amplitudes, it is reasonable to ignore the oscillations and use the standard time-independent dissipation rates. This is however not the case for higher values of parametric modulation, cf. Fig. III.2, where we note that the oscillation amplitudes build up and make them not negligible. Clearly, these terms cannot be neglected in any correct treatment of the dissipation as this may qualitatively affect the behaviour of the system. This motivates our approach, developed in Sec. III.3, to properly and quantitatively deal with dissipation in the present time-dependent system.

III.5 Cavity fluctuations and entanglement

In this section, we will discuss our results for the DM when it is parametrically driven from the NP. We will focus on both instabilities: the symmetry breaking to SP as well as the parametric instability to the D-NP. The spectral densities of the two baths are taken of the (same) Ohmic form $J(\omega) = \gamma\omega/\pi$, where γ is a dimensionless parameter that controls the strength of the system-bath interaction. For the subsequent investigation, we focus on the case of high-temperature thermal baths. This allows us to move a step forward in the analytical treatment of Eqs. (III.17)-(III.22). Later, we will review the same formalism for the DM in the RWA, which matches the quantum optics realization in a fast rotating frame. In the high-temperature case, the memory kernel [cf. Eq. (III.15)] and the temperature-dependent kernel [Eq. (III.25)] take the form $K(t) = 2i\gamma\delta'(t)$ and $K_T(t) = 2k_BT\gamma\delta(t)$, respectively. We remark

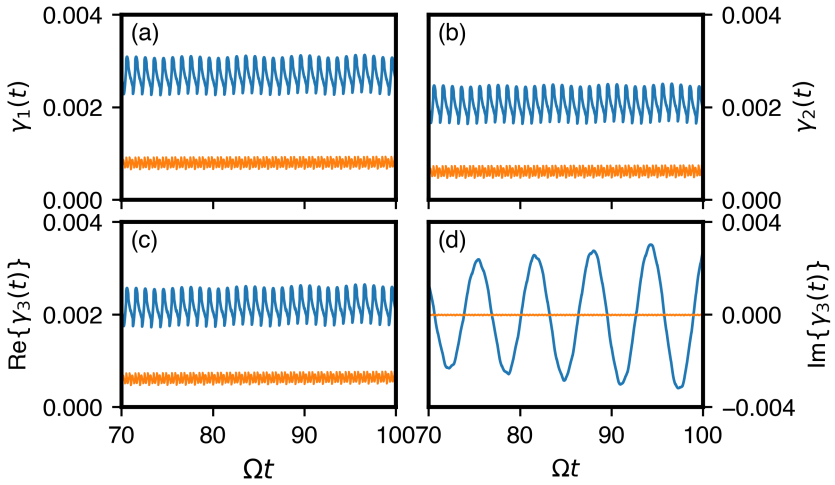

Figure III.2: Long-time behavior of the coefficients (a) $\gamma_1(t)$, (b) $\gamma_2(t)$, (c) $\mathrm{Re}\{\gamma_3(t)\}$, (d) $\mathrm{Im}\{\gamma_3(t)\}$ of the TCL master equation (III.27) for an ohmic bath at temperature $\bar{T} = 10$ and system-bath coupling strength $\gamma = 0.0002$. The excitation strength is $\bar{\epsilon} = 0.03$ (blue curves) and $\bar{\epsilon} = 0.001$ (orange curves), while the frequency, $\bar{\omega}_0 = 0.99$, is the same in all plots. For the Lindblad equation the constant dissipation rates are approximately given by $\gamma_1 \approx 0.001$ and $\gamma_2 \approx 0.0009$.

at this point that, contrarily to standard expectations, quantum features do survive in this limit. This claim will be discussed in detail later when we present the results for the entanglement.

All the results presented below are expressed in terms of dimensionless parameters. Measuring time in units of Ω, i.e. $\bar{t} = \Omega t$, leads to the following dimensionless parameters $\bar{\omega}_0$, $\bar{\lambda}$, $\bar{\epsilon} = \omega_0/\Omega$, λ/Ω, ϵ/Ω. The temperature is measured in terms of $T_0 = \hbar\omega_0/k_B$, which leads to the dimensionless temperature $\bar{T} = T/T_0$. Since we only work with these scaled parameters we drop the overbars for the sake of convenience.

III.5.1 Cavity fluctuations: NP-to-SP

As we anticipated above, the static DM exhibits a QPT at a critical value of the atom-field coupling strength (cf. Sec. III.1). Upon approaching the critical point the excitation number of the incoherent photons, $\langle \hat{a}^\dagger \hat{a} \rangle$, and the atom field, $\langle \hat{b}^\dagger \hat{b} \rangle$, diverge. The goal here is to investigate the dy-

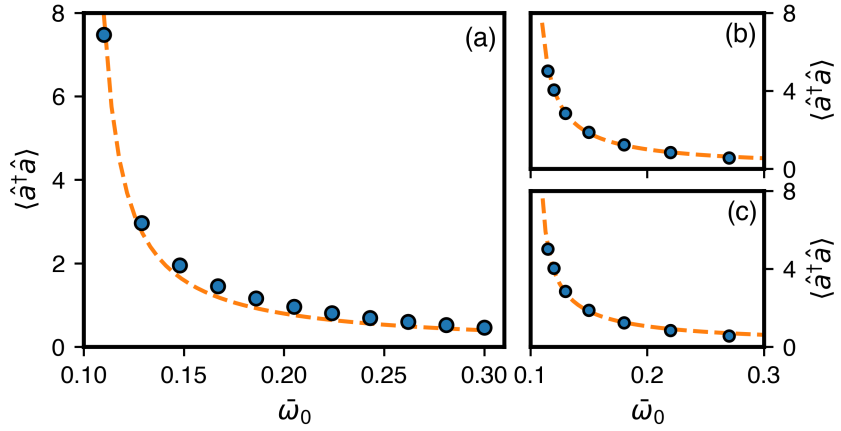

Figure III.3: Excitation number of the cavity fluctuations in the steady-state upon approaching the SP (blue circles). (a) A very small value of $\bar{\epsilon} = 0.0001$ has been fixed, together with $\lambda = 0.05$, and $\bar{\omega}_0$ decreased until very close to the NP-SP phase boundary. The critical point lies at $\bar{\omega}_0^{\text{crit}} \approx 0.1$. Fluctuations continuously diverge at the critical point with exponent 1 (orange dashed line). For higher values of $\bar{\epsilon}$, 0.001 in (b) and 0.005 in (c), fluctuations diverge with different exponents: 0.87 in (b) and 0.75 in (c).

namics of the excitation number of the cavity fluctuations with particular interest to its dependence on the parameters of the parametric drive: $\bar{\omega}_0$ and $\bar{\epsilon}$.

First, we look at the NP-SP boundary (see Fig. III.1), i.e. we fix the strength of the parametric modulation[9], $\bar{\epsilon} \approx 0$, and decrease the atomic (or cavity) frequency, $\bar{\omega}_0$. This corresponds to a vertical cut in the Fig. III.1. We can clearly see that the fluctuations increase upon approaching the SP and continuously diverge at the critical point with exponent 1 [see Fig. III.3(a)]. In the figure the circles correspond to the bare numerical results, while the dashed line to a fit

$$\langle \hat{a}^\dagger \hat{a} \rangle \propto (\bar{\omega}_0 - \bar{\omega}_0^{\text{crit}})^{-\xi}, \tag{III.37}$$

where $\bar{\omega}_0^{\text{crit}}$ corresponds to the NP-SP boundary and $\xi = 1$. Note that here we did not obtain the well-known exponent for the ground state of

[9]Here $\bar{\epsilon}$ has been fixed to the very small value 0.0001. The case of ϵ being strictly zero is not well-defined in the way our dimensionless parameters are defined (see above).

the DM, which is 1/2, but rather the steady-state result, in accordance with [141]. This is due to the fact that here, under the out-of-equilibrium conditions of driving, we are not exploring the ground-state physics of the system. We expect that the observed criticality will hold true at finite temperature and at zero temperature, where the quantum noise of the zero-temperature environment will still promote the steady-state scenario (cf. [141]). Interestingly, when moving along the NP-SP boundary (see Fig. III.1) the behavior of the cavity fluctuations at the critical point is modified. For larger values of driving strengths we obtain indeed different critical exponents: $\xi = 0.87$ for $\bar{\epsilon} = 0.001$ and $\xi = 0.75$ for $\bar{\epsilon} = 0.005$ [see Figs. III.3(b) and (c), respectively]. Here, parametric driving opens the door to a very rich nonequilibrium phase diagram, where the criticality of the system can be continuously changed. We found indeed a drive dependent critical exponent.

III.5.2 Cavity fluctuations: NP-to-D-NP

Parametric modulation of the light-matter coupling has a drastic effect on the stability of the NP: it was indeed shown to generate a parametric instability [21] to a new phase of matter, the D-NP. Having found such an intriguing physics for the phase transition between NP and SP, we would like to further explore the phase diagram of this out-of-equilibrium system. In order to investigate the NP-to-D-NP instability, we fix now the frequency $\bar{\omega}_0$ to some value and vary the driving strength $\bar{\epsilon}$ towards the D-NP phase boundary (see Fig.III.5).

Figure III.4 shows the full time evolution of the excitation number of the cavity fluctuations, $\langle \hat{a}^\dagger \hat{a} \rangle$, upon increasing $\bar{\epsilon}$ (from the bottom upwards in each panel). This figure refers to the case in which dissipation is absent. The upper panels, i.e. (a) and (b), correspond to a cut along $\bar{\omega}_0 = 0.93$, while the bottom ones to $\bar{\omega}_0 = 1.07$. We can connect this two cases with the previous discussion of the NM (cf. Sec. III.2); for $\bar{\omega}_0 = 0.93$ (resp. $\bar{\omega}_0 = 1.07$) the D-NP boundary coincide with the second (resp. first) NM becoming unstable. In the driven NP, the cavity fluctuations show an oscillatory behavior consisting of fast oscillations with a modulated amplitude. The period of the fast oscillations is approximately π, which corresponds to the periodic modulation appearing in Eq. (III.4). On the contrary, the complex beat structure arises from a combination of Floquet driving – this leads to an involved dynamics even for a single NM – and the superposition of the two NMs. Altogether this results in

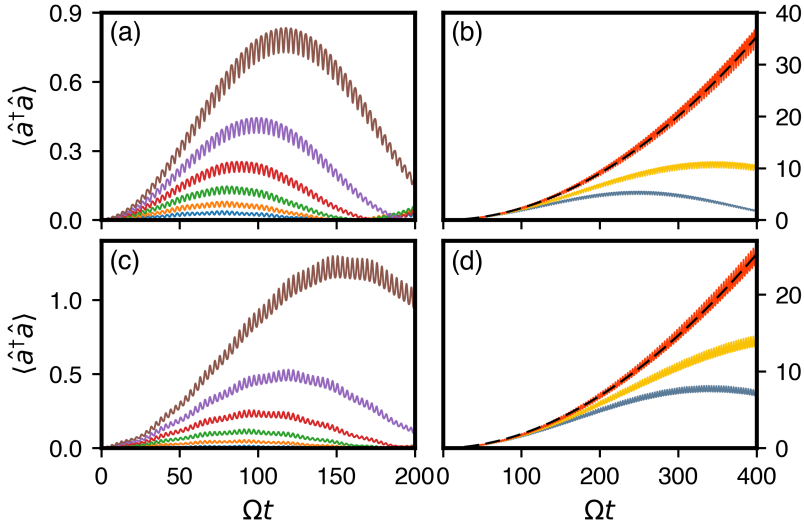

Figure III.4: Cavity fluctuations dynamics in the *absence* of dissipation. The left panels refer to driving strengths ϵ far from the D-NP boundary, while the right ones to driving strengths close to the boundary. The upper panels correspond to the frequency cut $\bar{\omega}_0 = 0.93$ and the bottom ones to $\bar{\omega}_0 = 1.07$. The different excitation strengths $\bar{\epsilon}$ are (from the bottom upwards): 0.01, 0.015, 0.02, 0.025, 0.03, 0.035 in (a), 0.043, 0.044, 0.045 in (b), 0.005, 0.01, 0.015, 0.02, 0.025, 0.03 in (c) and 0.0345, 0.035, 0.0355 in (d). In (b) and (d) the dashed black line on top of the diverging fluctuations shows a fit $\propto \bar{t}^{\alpha}$, with $\alpha = 1.97$ in (b) and 1.89 in (d).

a highly complex behavior of the time dependent fluctuations observed in Fig. III.4. Increasing the strength of the parametric drive leads to a higher number of excitations, as seen in Figs. III.4(a) and (c). Moreover, the larger the amplitude of the parametric modulation, the longer the quasi-period of the beat structure. When approaching the D-NP boundary this quasi-period diverges, and the cavity fluctuations grow without bound [see Figs. III.4 (b) and (d)]. These two panels show the time evolution of $\langle \hat{a}^\dagger \hat{a} \rangle$ for three values of $\bar{\epsilon}$ imminent to the D-NP, the last of which lies on the phase boundary and shows a polynomial growth [see Figs. III.4 (b) and (d), red curves]. The black dashed line corresponds to a fit

$$\langle \hat{a}^\dagger \hat{a} \rangle \propto \bar{t}^{\alpha}, \tag{III.38}$$

in which α depends on the exact position $(\bar{\omega}_0, \bar{\epsilon})$ in the parameter space.

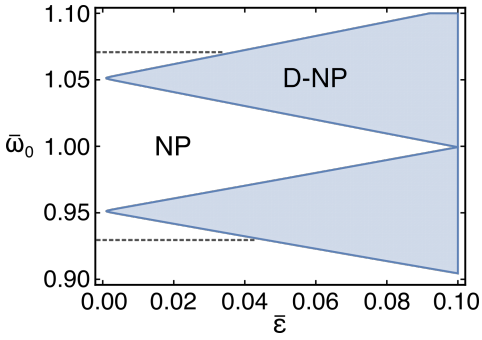

Figure III.5: Nonequilibrium phase diagram of the parametrically driven Dicke model as a function of the frequency, $\bar{\omega}_0$ and modulation strength $\bar{\epsilon}$. The static coupling is $\bar{\lambda} = 0.05$ and the system-bath coupling strength $\gamma = 0.0001$. The grey dashed lines indicate the frequency cuts discussed in the main text. Compared to Fig. III.1, the present phase diagram corresponds to a zoom around the tips of the D-NP. The SP lies further down to lower values of $\bar{\omega}_0$ (cf. Fig. III.1).

In the two cases shown above, we found $\alpha = 1.97$ in (b) and 1.89 in (d). The transition from the NP to the D-NP is therefore characterized by fluctuations that diverge following a polynomial growth ($\propto \bar{t}^{\alpha}$) with driving-dependent coefficient (α).

The corresponding results for a system that is weakly-interacting[10] with a thermal bath are shown in Fig. III.6. As for the dissipationless case, increasing values of $\bar{\epsilon}$ are shown from the bottom upwards in each panel and the same two values of $\bar{\omega}_0$ have been chosen. The difference is that here, as opposed to Fig. III.4, the left and right panels correspond to the same values of modulation strength, but compare two different temperatures: $\bar{T} = 10$ (left panels) and $\bar{T} = 20$ (right panels). Note that, even though the field amplitude $\langle \hat{a} \rangle$ exhibits a decaying behavior [as dictated by Eq. (III.15)], the number of the incoherent photons $\langle \hat{a}^{\dagger} \hat{a} \rangle$ does not. On the contrary, it still shows oscillations, as in Fig. III.4, but it tends to the number of excitation quanta of the reservoir modes. Both figures III.4 and III.6 seem to indicate that the cavity fluctuations are greatly

[10]Here we only consider the case in which the system-bath interaction is very weak, i.e. the dimensionless parameter $\gamma \ll 1$. This is not a limitation of our approach as we did not consider the interaction in the standard rotating-wave approximation, rather it is motivated by the results for the atom-field entanglement presented below.

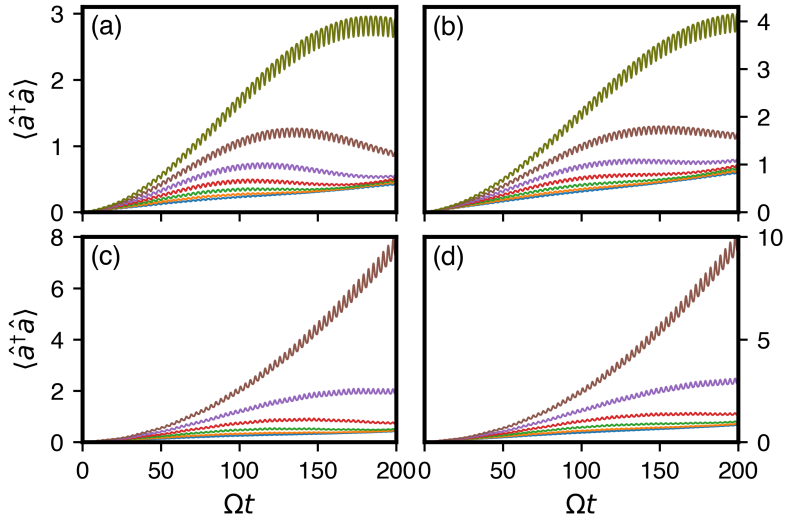

Figure III.6: Cavity fluctuations dynamics in the *presence* of dissipation. The left panels refer to the temperature $\bar{T} = 10$ and the right ones to $\bar{T} = 20$, while the system-bath coupling strength, $\gamma = 0.0001$, is the same for all the curves. The upper panels correspond to the frequency cut $\bar{\omega}_0 = 0.93$ and the bottom ones to $\bar{\omega}_0 = 1.07$. When comparing left to right panels the same color correspond to the same excitation strength. The different excitation amplitudes $\bar{\epsilon}$ are (from the bottom upwards): 0.01, 0.015, 0.02, 0.025, 0.03, 0.035, 0.04 in (a) and (b), while in (c) and (d) the upper most curve ($\bar{\epsilon} = 0.04$) is missing.

affected by the parameters ($\bar{\omega}_0$, $\bar{\epsilon}$), rather than by the bath temperature $\bar{T}$. This being said, we will see in what follows that the latter plays a crucial role in the fate of the entanglement dynamics.

The results obtained so far for the cavity fluctuations indicate that the nonequilibrium phases of the periodically modulated DM are connected by a very different critical behavior. On the one hand, the phase boundary between the NP and the SP is characterized by a divergence of the excitation number of the incoherent photons, $\langle \hat{a}^\dagger \hat{a} \rangle$, in the steady state. Remarkably, the criticality of the system can be tuned by the action of the periodic modulation. On the other hand, when we approach the phase boundary of D-NP, the cavity fluctuations transition from bounded to unbounded at the critical point, where they grow polynomially in time. Notably, the growing rate of the incoherent photons depends on the

driving parameters, i.e. $\alpha = \alpha(\bar{\omega}_0, \bar{\epsilon})$ in Eq. (III.38).

III.5.3 Entanglement dynamics

Quantum entanglement is most probably the characteristic trait of quantum mechanics and one of the most prominent differences between the classical and the quantum theory. It is not only of great importance at a fundamental level, for questions like the emergence of classicality from quantum mechanics [142], but it is also a central resource for quantum information processing [143]. It is indeed at the heart of quantum teleportation, cryptography as well as quantum computing [144]. Hence, the understanding of how the coupling to an environment and periodic driving influence the dynamical behavior of entanglement is of significant importance.

The total Hamiltonian [Eq. (III.10)-(III.12)] is bilinear in the system operators, which ensures that Gaussian states remain Gaussian during the time evolution [145]. These states are nowadays routinely prepared and easily controlled in many quantum optical experiments. Furthermore, some experimental transformations performed on quantum states are also Gaussian, i.e. they preserve the Gaussian nature of states [146]. Hence, restricting our attention to these kind of states does not have to be perceived as artificial, rather of current interest.

As is well known, Gaussian states are fully characterized by the real and symmetric $2N \times 2N$ covariance matrix (CM) $\Gamma_{jk} = \frac{1}{2}\langle \hat{R}_j \hat{R}_k + \hat{R}_k \hat{R}_j \rangle - \langle \hat{R}_j \rangle \langle \hat{R}_k \rangle$, where we have defined the vector of canonical operators $\hat{\mathbf{R}} \equiv (\hat{x}, \hat{p}_x, \hat{y}, \hat{p}_y)$. We denote the field position and momentum operators by $\hat{x} = (\hat{a}^\dagger + \hat{a})/\sqrt{2\omega_0}$ and $\hat{p}_x = i\sqrt{\omega_0/2}\,(\hat{a}^\dagger - \hat{a})$ and the atomic operators by $\hat{y} = (\hat{b}^\dagger + \hat{b})/\sqrt{2\omega_0}$ and $\hat{p}_y = i\sqrt{\omega_0/2}\,(\hat{b}^\dagger - \hat{b})$. With the help of the three real 2×2 matrices $\mathbf{A}$, $\mathbf{B}$ and $\mathbf{C}$ the CM $\mathbf{\Gamma}$ can be conveniently expressed in the following block form

$$\mathbf{\Gamma} = \begin{pmatrix} \mathbf{A} & \mathbf{C} \\ \mathbf{C}^\top & \mathbf{B} \end{pmatrix}. \tag{III.39}$$

The two blocks $\mathbf{A}$ and $\mathbf{B}$ contain the autocorrelations within the field mode ($\hat{a}$) and the atomic mode ($\hat{b}$), while $\mathbf{C}$ contains the cross-correlations between them. As anticipated in Sec. III.3, we work in the NM picture and transform back to the original system at the end. For this reason, we need to relate the two pictures. Specifically, the CM for the real operators

can be directly obtained from the one for the NMs through a symplectic transformation. Similarly to what we did above, we introduce the vector of canonical NM operators $\hat{\mathbf{R}}' \equiv (\hat{X}_+, \hat{P}_+, \hat{X}_-, \hat{P}_-)$ and the CM for the NMs as $\Gamma'_{jk} = \frac{1}{2}\langle \hat{R}'_j \hat{R}'_k + \hat{R}'_k \hat{R}'_j \rangle - \langle \hat{R}'_j \rangle \langle \hat{R}'_k \rangle$. The vector of canonical operators and the CM for the real and NM coordinates are then related by the equations $\hat{\mathbf{R}}' = \mathbf{S}\hat{\mathbf{R}}$ and $\mathbf{\Gamma}' = \mathbf{S}\mathbf{\Gamma}\mathbf{S}$, where the symplectic transformation matrix $\mathbf{S}$ is given by

$$\mathbf{S} = \frac{1}{\sqrt{2}} \begin{pmatrix} \mathbb{I}_2 & \mathbb{I}_2 \\ \mathbb{I}_2 & -\mathbb{I}_2 \end{pmatrix}.$$

A particularly suitable measure of entanglement for Gaussian states is the logarithmic negativity[11] [149]. It is defined as

$$E_N = \max\{0, -\log(2\tilde{\nu}_-)\}, \tag{III.40}$$

where $\tilde{\nu}_-$ is the smallest symplectic eigenvalue[12] of the partial transpose CM $\tilde{\mathbf{\Gamma}}$. A simple expression for the symplectic eigenvalues $\tilde{\nu}_\mp$ can be found in terms of the $Sp(4,\mathbb{R})$ invariants $\tilde{\Delta}(\mathbf{\Gamma}) \equiv \det(\mathbf{A}) + \det(\mathbf{B}) - 2\det(\mathbf{C})$ and $\det(\mathbf{\Gamma})$ and reads [149, 151]:

$$2\tilde{\nu}_\mp^2 = \tilde{\Delta}(\mathbf{\Gamma}) \mp \sqrt{\tilde{\Delta}(\mathbf{\Gamma})^2 - 4\det(\mathbf{\Gamma})}. \tag{III.41}$$

In what follows, we assume the system to be in a separable initial Gaussian state, in which the two modes are prepared in their single-mode squeezed vacuum states with CM given by

$$\mathbf{\Gamma} = \frac{1}{2} \begin{pmatrix} c & s & 0 & 0 \\ s & c & 0 & 0 \\ 0 & 0 & c & s \\ 0 & 0 & s & c \end{pmatrix},$$

where $c = \cosh(r)$ and $s = \sinh(r)$, with r the so-called squeezing parameter. In short, a single-mode squeezed state is the state of a single oscillator that has any of the quadratures with variance below $1/2$. Single-mode squeezed vacuum states additionally satisfy the condition for the

[11] This measure of entanglement is based on the Peres-Horodecki criterion for separability [147, 148]. It states that a bipartite quantum state is separable if and only if its partial transposed state is positive.

[12] Due to Williamson theorem [150] any real symmetric positive-definite matrix, such as the CM, can be brought to Williamson normal form – or diagonal form – via symplectic transformations, i.e. preserving the canonical commutation relations.

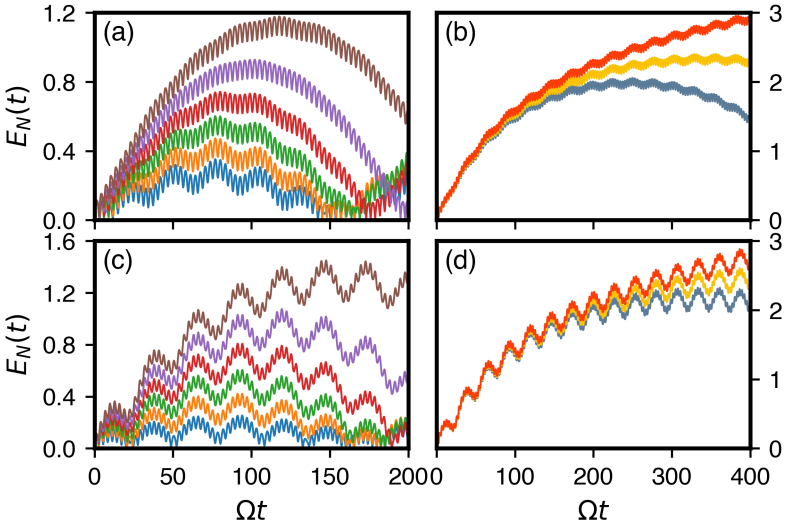

Figure III.7: Atom-field entanglement dynamics in the *absence* of dissipation. Shown is the logarithmic negativity E_N as a function of time for an initial vacuum state (separable). The left panels refer to driving strengths ϵ far from the D-NP boundary, while the right ones to driving strengths close to the boundary. All the parameters are as in Fig. III.4.

vacuum state, i.e. that the product of the position and momentum variances is $1/4$. For an unsqueezed vacuum state $r = 0$ and the CM reduces to $\mathbf{\Gamma} = \frac{1}{2}\mathbb{I}$.

The time evolution of the atom-field entanglement, measured through the logarithmic negativity [Eq. (III.40)], is shown in Fig. III.7. For the moment, we consider the case in which there is no dissipation. One can see that entanglement between the cavity mode and the atoms can be generated from an initially separable state ($r = 0$). This feature has been also observed for two coupled harmonic oscillators [152–154]. However, through a parametric driving of the atom-field coupling higher values of logarithmic negativity can be achieved, cf. Fig. III.7(a) and (c). In general, larger modulation strengths $\bar{\epsilon}$ (from the bottom upwards in each panel) lead to stronger entanglement. As before, the upper and lower panels correspond to the two frequency cuts $\bar{\omega}_0 = 0.93$ and $\bar{\omega}_0 = 1.07$, respectively (see Fig. III.5). When it is not subject to dissipation, the

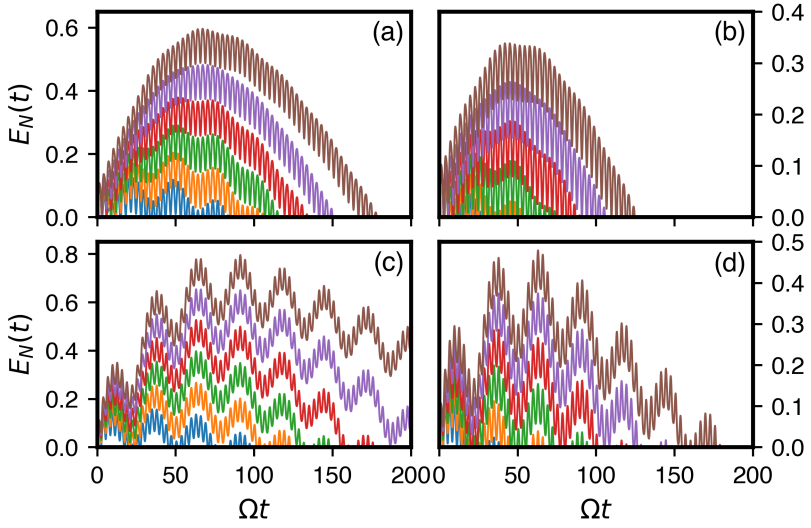

Figure III.8: Atom-field entanglement dynamics in the *presence* of dissipation. Shown is the logarithmic negativity E_N as a function of time for an initial vacuum state (separable). The left panels refer to the temperature $\bar{T} = 10$ and the right ones to $\bar{T} = 20$, while the system-bath coupling strength, $\gamma = 0.0001$, is the same for all the curves. The upper panels correspond to the frequency cut $\bar{\omega}_0 = 0.93$ and the bottom ones to $\bar{\omega}_0 = 1.07$. When comparing left to right panels the same color correspond to the same excitation strength. The different excitation strengths $\bar{\epsilon}$ are (from the bottom upwards): 0.01, 0.015, 0.02, 0.025, 0.03, 0.035.

system can sustain a finite entanglement for arbitrarily long times. Similarly to the cavity fluctuations (see Fig. III.4), the entanglement dynamics shows an oscillatory behavior in which fast oscillations are combined with a beat structure [see Fig. III.7(a) and (c)]. Upon approaching the D-NP boundary the quasi-period of the amplitude modulation grows and diverges upon hitting the phase boundary [see Fig. III.7(b) and (d)]. It is worth noting that, for parameter values close to the D-NP, the system can sustain a considerable entanglement despite containing many excitations quanta [see Fig. III.4(b) and (d)].

A drastic change occurs when the system is coupled to a thermal bath, as shown by the Fig. III.8. Though interacting with a reservoir, the atom-field coupling – especially due to its periodic modulation – still generates entanglement between the two subsystems. Despite that,

we find that the driven NP is characterized by disentanglement at finite times (sudden death), cf. Fig. III.8. This behavior – unlike decoherence, which is asymptotic in time [135, 136] – has also been observed in other systems [155–158]. This is due to the competing effects of the environment, which tries to kill entanglement, and those of the coupling plus parametric drive, which can generate entanglement. Figure III.8 demonstrates that this antagonism is always won by the thermal baths. The parametric modulation of the atom-field coupling can however delay this fate. As one can see from Fig. III.8, the entanglement can be sustained for longer times on increasing the value of the modulation strength $\bar{\epsilon}$ (higher values are shown from the bottom upwards in each panel). For parameter values in the proximity of the D-NP boundary the disentanglement time can be pushed to very large values and, when touching the phase boundary, an oscillatory behavior around a finite value is observed.

We remark that, in the past few years Ref. [128] and others have discussed the generation of steady-state entanglement at high temperatures in a system of two dissipative oscillators with parametric modulation of their coupling. This rather surprising result led to numerous discussions about using periodic driving to sustain quantum effects at high temperature, i.e., parametric driving can substantially shift the quantum-classical crossover to much higher temperatures. This scenario is however fictitious because the system would be populated by an ever-increasing number of excitation quanta [see Fig. III.4 and III.6, (b) and (d)]; it could hence only be sustained for a short time interval before the system collapses. However, we should stress that in our system a phase transition to the D-NP occurs. In order to make a conclusive statement on whether entanglement can be sustained or not, one would need a different point of departure. At finite temperatures, we expect that no asymptotic entanglement will survive as one approaches the NP-SP phase boundary.

To get a deeper understanding of the physics underlying this periodically driven system, we consider now the problem from another point of view: the Weyl-Wigner (or so-called phase space) representation of the density matrix. Usually, in quantum mechanics we work *either* with probability densities in position *or* in momentum space. The Wigner function, introduced by Wigner in the 1930s, was born as an attempt to have a function that displays *both* probability distributions simulta-

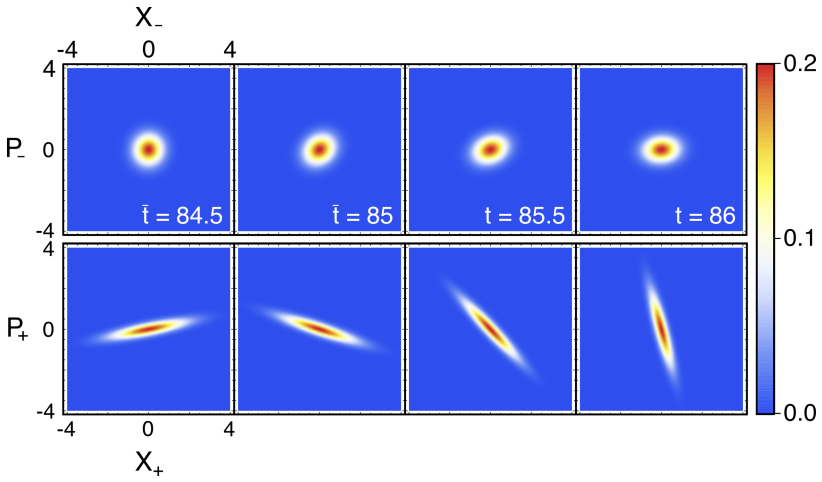

Figure III.9: Dynamics (from left to right) of the Wigner function of the first (lower panels) and second (upper panels) normal mode. The parameters are the same used in Fig. III.4(a) and III.7(a), brown curves. The four panels show the time evolution of $W(\mathbf{R}_\pm)$ [see Eq. (III.42)] following the dynamics of a short-period oscillation (time interval from 84.5 to 86 time units).

neously [159]. Said in simple terms, it plays the role of a probability distribution of phase space variables. We need to stress the fact that, due to the uncertainty principle, a phase space representation of quantum mechanics is intricate. Being indeed not strictly positively defined, it is often referred to as a quasi-probability distribution. We refrain here from giving a thorough introduction on this topic and limit ourselves to an essential introduction. There is a fairly extensive literature that can be consulted by the interested reader [160–162].

We use now the concept just introduced to investigate the dynamics of the two NMs in the generalized phase space introduced above, i.e. defined by X_+, P_+, X_-, and P_-. The Wigner function of a Gaussian state takes the following simple form in terms of phase space quadratues

$$W(\mathbf{R}_\pm) = \frac{\mathrm{e}^{-\mathbf{R}_\pm^\top \boldsymbol{\Gamma}_\pm^{-1} \mathbf{R}_\pm}}{\pi^2 \sqrt{\det \boldsymbol{\Gamma}_\pm}}, \tag{III.42}$$

where $\mathbf{R}_\pm = (X_\pm, P_\pm)$ are the NM phase-space coordinates for the first (+) and second (-) NM and $\boldsymbol{\Gamma}_\pm$ the corresponding CM. Here $\mathbf{R}_\pm^\top$ denotes

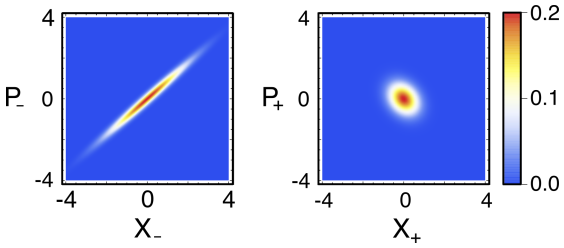

Figure III.10: Wigner function of the first (right panel) and second (left panel) normal mode for a fixed time ($\bar{t} = 87.5$). The parameters are the same used in Fig. III.4(b) and III.7(b), brown curves.

the traspose of $\mathbf{R}_{\pm}$. Note that in Eq. (III.42) we omitted the first moments (i.e. $\langle \mathbf{R}_{\pm} \rangle = 0$) [cf. Eq. (III.39) and text below]. The dynamics of the Wigner functions of the two NMs is illustrated in Fig. III.9 for the same parameter values used in Fig. III.4(a) and III.7(a), brown curves. This corresponds to parameters close to the lower instability lobe (cf. Fig. III.5). We can clearly see that the second NM (upper panels) remains very localized during the time evolution, with squeezing almost absent. What we observe instead for the first NM (lower panels) is a sizable squeezing. We remind that initially the system is in a separable state and the entanglement is zero, which corresponds to both modes being unsqueezed (i.e. circles in the way they are presented in Fig. III.9). While the second NM is barely modified, the first one displays strong squeezing and thus entanglement of the real modes (i.e. atoms and field). During the time evolution the Wigner function of this NM elongates along a dynamical axis that rotates at a frequency that matches the fast oscillations seen in the entanglement dynamics (see Fig. III.7). In Fig. III.10, we show the Wigner function, for a fixed time, for parameters close to the upper instability lobe (cf. Fig. III.5). The time evolution of $W(\mathbf{R}_{\pm})$ is similar to the one shown in Fig. III.9, therefore it will not be shown again. However, in this case the roles are exchanged: while the first NM (right panel) remains nearly unsqueezed for all times, the second NM (left panel) displays strong squeezing. Hence, we can conclude that the entanglement behavior found above (cf. Figs. III.7 and III.8) is mainly dictated by the NM that is on the verge of instability.

After examining the dynamics of the entanglement and getting some insights into its origin, we would like to digress a moment and turn our

attention to a fundamental question. Not long ago physicists started investigating the possible connection between criticality and entanglement [163]. A short, subjective, and surely not exhaustive list of remarkable results is the following. It has been argued that the critical point of a quantum lattice system is signalled by the lattice being maximally entangled [164]. An entanglement jump in a spin-half model, which was measured through the ground state concurrence, indicated the occurrence of a first-order quantum phase transition [165]. Furthermore, the concurrence of the ground state was shown to exhibit a cusplike singularity at the critical point [166]. Still, a conclusive answer to this fundamental issue has not been found yet. For instance, in Ref. [167] a discontinuity in the first derivative of ground-state concurrence occurs even though the system does *not* undergo a quantum phase transition. That said, there is still the belief that criticality and entanglement are intimately related, but the potential use of concurrence as a detection tool has been ruled out. Other measures of entanglement could potentially do the job.

Going back to our system, we observed that the entanglement dynamics – expressed in terms of logarithmic negativity – is sensitive to the phase boundary between the NP and the D-NP both when dissipation is absent and present. In the first case, the bounded oscillatory behavior peculiar to the driven NP turns into monotonously increasing (on average, neglecting the fast oscillations) as one approaches the instability boundary. In the dissipative case, though we have permanent disentanglement at finite times, the transition to the D-NP is flagged by the development of nonzero stationary entanglement.

To conclude, even though we shed some light on the nature of the transition between the NP and the D-NP, further investigations are necessary. To fully understand how entanglement varies across this out-of-equilibrium transition from the NP to the D-NP, one needs indeed to approach the critical boundary from both sides. The method developed in the present chapter, however, only allows us to study the driven NP. Generalizations of our EOM approach are required to study the dynamical properties of the new nonequilibrium D-NP. We leave this as an outlook for future work. Lastly, we would like to draw the attention to the choice of high-temperature thermal baths. This is by no means a limitation of the method, rather a practical choice dictated by an easier numerical implementation of the equations. The same method could be used to study the low temperature regime as well as the full non-Markovian

dynamics of the system.

III.6 Dicke model in rotating wave approximation

The DM is often studied using the RWA, where the counter-rotating terms appearing in Eq. (III.5) are neglected and the Hamiltonian reads [168]

$$\hat{H}_S(t) = \omega_c \hat{a}^\dagger \hat{a} + \omega_a \hat{b}^\dagger \hat{b} + \lambda(t)\left(\hat{a}^\dagger \hat{b} + \hat{b}^\dagger \hat{a}\right). \tag{III.43}$$

We couple again the system to two independent baths, as in Eq. (III.6), but now we assume the system and reservoirs to be coupled in RWA, that is

$$\hat{H}_I = \sum_k g_k(\hat{a}^\dagger \hat{c}_k + \hat{a}\hat{c}_k^\dagger) + \sum_i g_i(\hat{b}^\dagger \hat{d}_i + \hat{b}\hat{d}_i^\dagger). \tag{III.44}$$

The present system is decoupled by much easier Bogoliubov transformations than those employed before [cf. Eq. (III.8)]. Again, we focus here on the symmetric case, i.e. $\omega_c = \omega_a \equiv \omega_0$. In this case, the NM frequencies are given by

$$\Omega_{1,2}^2(t) = \omega_0 \pm \lambda(t), \tag{III.45}$$

and the NM operators for the system and baths are, respectively

$$\begin{aligned} \hat{A}_1 &= \frac{1}{\sqrt{2}}(\hat{a} + \hat{b}), \quad \hat{A}_2 = \frac{1}{\sqrt{2}}(\hat{a} - \hat{b}), \\ \hat{C}_k &= \frac{1}{\sqrt{2}}(\hat{c}_k + \hat{d}_k), \quad \hat{D}_k = \frac{1}{\sqrt{2}}(\hat{c}_k - \hat{d}_k). \end{aligned} \tag{III.46}$$

Note that the transformations for the system only involve two operators each. This is in contrast to Eq. (III.8), where each transformation involved four operators. We also stress that the NM transformations became *time independent* now. The Eqs. (III.46) leads to the following Hamiltonian of the uncoupled system

$$\hat{H}_{\tilde{S}}(t) = \Omega_1(t)\hat{A}_1^\dagger \hat{A}_1 + \Omega_2(t)\hat{A}_2^\dagger \hat{A}_2\,, \tag{III.47}$$

where the excitation energies are given by Eq. (III.45). The baths and interaction Hamiltonians are transformed to

$$\begin{aligned}\hat{H}_{\tilde{B}} &= \hat{H}_{\tilde{B}_1} + \hat{H}_{\tilde{B}_2} \\ &= \sum_k \omega_k \hat{C}_k^\dagger \hat{C}_k + \sum_i \omega_i \hat{D}_i^\dagger \hat{D}_i, \end{aligned} \tag{III.48}$$

$$\hat{H}_{\tilde{I}} = \sum_k g_k (\hat{A}_1^\dagger \hat{C}_k + \hat{A}_1 \hat{C}_k^\dagger) + \sum_i g_i (\hat{A}_2^\dagger \hat{D}_k + \hat{A}_2 \hat{D}_k^\dagger). \tag{III.49}$$

As opposed to Eq. (III.12), where both the NM operators $\hat{A}_k^{(\dagger)}$ and the coupling strengths $\tilde{g}_k$ were explicitly time dependent, the interaction Hamiltonian (III.49) is now time independent.

III.6.1 Time evolution

As it was the case before, the Hamiltonians (III.47)-(III.49) show that in the NM picture the system separates into two subsystems, whose dynamics is independent of each other. Hence, we focus again on a single NM oscillator, the first one, coupled to a NM reservoir. The starting point are once again the Heisenberg EOM for the operators $\hat{A}_1$ and $\hat{C}_k$, which read

$$\dot{\hat{A}}_1(t) = -i\Omega_1(t)\hat{A}_1 - i\sum_k g_k \hat{C}_k, \tag{III.50}$$

$$\dot{\hat{C}}_k(t) = -i\omega_k \hat{C}_k - i g_k \hat{A}_1. \tag{III.51}$$

The next step consists in integrating Eq. (III.51) and substitute it in (III.50), which gives the following equation for the system NM

$$\begin{aligned}\dot{\hat{A}}_1(t) = -i\Omega_1(t)\hat{A}_1 - i\sum_k g_k \hat{C}_k(0) \mathrm{e}^{-i\omega_k t} \\ - \sum_k g_k^2 \int_0^t \hat{A}_1(\tau) \mathrm{e}^{-i\omega_k(t-\tau)} \mathrm{d}\tau.\end{aligned}$$

Now it is where the derivation begins to take a different path than that pursued in Sec. III.3. We switch here to a rotating frame given by $\hat{A}_1(t) = \hat{\mathcal{A}}_1(t)\mathrm{e}^{-i\omega_0 t}$. The resulting EOM for $\hat{\mathcal{A}}_1$ is given by

$$\begin{aligned}\dot{\hat{\mathcal{A}}}_1(t) = -i\lambda(t)\hat{\mathcal{A}}_1(t) - i\sum_k g_k \hat{C}_k(0) \mathrm{e}^{-i(\omega_k-\omega_0)t} \\ - \sum_k g_k^2 \int_0^t \hat{\mathcal{A}}_1(\tau) \mathrm{e}^{-i(\omega_k-\omega_0)(t-\tau)} \mathrm{d}\tau,\end{aligned} \tag{III.52}$$

where we have used the expression for the excitation energy [see Eq. (III.45)]. We devote now our attention to the last term in Eq. (III.52). We consider a continuous distribution of bath modes by introducing the spectral density $J(\omega)$[13]. After the change of variables $t' = t - \tau$ we obtain

$$-\int_0^t \mathrm{d}t' \int_0^\infty \mathrm{d}\omega J(\omega)\hat{\mathcal{A}}_1(t-t')\mathrm{e}^{-i(\omega-\omega_0)t'}.$$

This is the point where we make the *Markov approximation* [135, 136], i.e. we assume here that the system-bath interaction-induced self-correlations within the environment are much smaller than the time scale for significant changes in the system. Under this approximation $\hat{\mathcal{A}}_1(t-t')$ can be replace by $\hat{\mathcal{A}}_1(t)$ and extracted from the integral. The last expression thus simplifies to[14]: $-(\gamma + i\Delta\omega)\hat{\mathcal{A}}_1(t)$. The two parameters γ and $\Delta\omega$ have been defined as

$$\begin{aligned} \gamma &= \pi J(\omega_0), \\ \Delta\omega &= \mathcal{P}\int_0^\infty \frac{J(\omega)}{\omega_0 - \omega}\mathrm{d}\omega. \end{aligned} \tag{III.53}$$

III

Lastly, transforming back to the non-rotating frame we obtain the following EOM for the operator $\hat{A}_1$:

$$\begin{aligned} \dot{\hat{A}}_1(t) = &-i\big(\Omega_1(t) + \Delta\omega\big)\hat{A}_1(t) - \gamma\hat{A}_1(t) \\ &- i\sum_k g_k\hat{C}_k(0)\mathrm{e}^{-i\omega_k t}. \end{aligned} \tag{III.54}$$

While γ is responsible for dissipation in Eq. (III.54), the term $\Delta\omega$, known as *Lamb shift*, provides an energy shift. Since we are here interested in the effect of dissipation we will incorporate $\Delta\omega$ into a renormalized system frequency ω_0^{ren}. From now on we will however stick to ω_0 for the sake of notational simplicity.

In order to find a solution to this equation we proceed in the same way we did in Sec. III.3. Due to its simple form – more precisely, due to

[13] We recall its definition: $J(\omega) = \sum_k g_k^2\delta(\omega - \omega_k)$, cf. Sec. III.3.

[14] Here we have used that

$$\lim_{t\to\infty}\int_0^t \mathrm{d}t'\mathrm{e}^{-i(\omega-\omega_0)t'} = \pi\delta(\omega-\omega_0) + i\frac{\mathcal{P}}{\omega_0-\omega},$$

where $\mathcal{P}$ denotes the Cauchy principal value. Clearly the equality sign must be understood in the sense of distributions.

the absence of its Hermitian conjugate in Eq. (III.54) – we use here the following simple ansatz [cf. Eq. (III.16)]

$$\hat{A}_1(t) = G(t)\hat{A}_1(0) + \hat{F}(t). \tag{III.55}$$

The same procedure employed above leads to the following equations for the time-dependent function $G(t)$ and operator $\hat{F}(t)$

$$\dot{G}(t) = -i\Omega_1(t)G(t) - \gamma G(t), \tag{III.56}$$

$$\dot{\hat{F}}(t) = -i\Omega_1(t)\hat{F}(t) - \gamma\hat{F}(t) - i\sum_k g_k C_k(0)\mathrm{e}^{-i\omega_k t}, \tag{III.57}$$

with the initial condition $G(0) = 1$. The Eq. (III.57) for the operator $\hat{F}$ has the following formal solution

$$\hat{F}(t) = \sum_k g_k C_k(0)\int_0^t \Lambda(t,t')\mathrm{e}^{-i\omega_k t'}\mathrm{d}t', \tag{III.58}$$

where the function $\Lambda(t,t')$ is determined, for fixed t', by the following differential equation

$$\dot{\Lambda}(t,t') = -i\Omega_1(t)\Lambda(t,t') - \gamma\Lambda(t,t'), \tag{III.59}$$

with the initial condition $\Lambda(t,t) = -i$.

Our strategy to tackle the time evolution of any observable related to the initial system, which is defined by Eqs. (III.43) and (III.44), is the same one we already used in Sec. III.3. We first study the NMs, whose time evolution is fully determined by the Eqs. (III.55)-(III.59). Any physical observable, in the NM picture, can be found from Eq. (III.55) by taking the appropriate expectation values. Lastly, we return to the original system using the transformations (III.46).

In what follows we opt for the same assumptions used for the non-RWA case studied in Sec. III.3. We assume the system and reservoir to be initially uncorrelated, which gives the following expression for the time evolution of the expectation value of the NM occupation number [cf. Eq. (III.23)]:

$$\begin{aligned} N_1(t) &= \langle \hat{A}_1^\dagger(t)\hat{A}_1(t)\rangle \\ &= |G(t)|^2\langle \hat{A}_1^\dagger(0)\hat{A}_1(0)\rangle + \langle \hat{F}^\dagger(t)\hat{F}(t)\rangle. \end{aligned} \tag{III.60}$$

We note that the formal expression for $N_1(t)$ in the RWA can be obtained from the one of the non-RWA case [see Eq. (III.23)] by setting L to zero.

We stress that this only works at the formal level and it follows from the simpler form of the ansatz (III.55) with respect to (III.16). The actual RWA results are however *not* found by the setting L to zero in the non-RWA ones. The function G and the operator $\hat{F}$ are governed by *different* EOMs and will, in general, have a different time evolution. As for the derivation of the non-RWA bath correlation function [see Eq. (III.24)] we assume both baths to be in thermal equilibrium at the same temperature T. This, together with the fact that the transformations between the real and NM baths remained unaltered between the RWA and non-RWA cases, allows us to use again Eq. (V.9). On the other hand – in accordance with the treatment hitherto followed – we invoke again the RWA approximation and obtain the following expression for the last term appearing in Eq. (III.60)

$$\langle \hat{F}^\dagger(t)\hat{F}(t)\rangle = 2\gamma n(\omega_0, T)\int_0^t |\Lambda(t,t')|^2\,\mathrm{d}t',$$

where γ is defined as in (III.53) and $n(\omega_0, T)$ gives the mean number of bath modes at frequency ω_0 in thermal equilibrium at temperature T (see Appendix B). The only nonvanishing bath correlation function that remains is $\langle \hat{F}(t)\hat{F}^\dagger(t)\rangle$ and is explicitly given by

$$\langle \hat{F}(t)\hat{F}^\dagger(t)\rangle = 2\gamma\big(n(\omega_0, T)+1\big)\int_0^t |\Lambda(t,t')|^2\,\mathrm{d}t'.$$

Note that in the present RWA case $\langle \hat{F}(t)\hat{F}(t)\rangle$ and $\langle \hat{F}^\dagger(t)\hat{F}^\dagger(t)\rangle$ are both zero. This was not the case in the non-RWA case, where all the bath correlation functions are nonvanishing. The reason for that can be seen by looking at the formal solutions for the operator $\hat{F}$ in both cases, i.e. by comparing Eq. (III.20) with (III.58). While the expression for $\hat{F}$ in RWA only contains the annihilation operators $C_k(0)$, in the non-RWA case it contains both annihilation as well as creation operators $C_k^\dagger(0)$. As a consequence, when computing bath correlation functions the nonvanishing terms $\langle C_k^\dagger(0)C_{k'}(0)\rangle$ and $\langle C_k(0)C_{k'}^\dagger(0)\rangle$ always appear. This is clearly not the case in the RWA.

III.7 Conclusion and discussion

Light-matter systems are the ideal platform to study the combined effect of interactions, dissipation and driving. While interactions and dissi-

pations are intrinsically part of the system, some sort of driving is necessary to obtain interesting physics. In this context, parametric driving furnished the framework for the observation of a great variety of new phenomena. Specifically, in the DM the periodic modulation of the atom-field coupling results in a very rich nonequilibrium phase diagram, where parametric resonance gives rise to a novel phase that has no counterpart in the undriven case. Here, we have studied the phase diagram of this system and found several interesting features. We observed indeed that the criticality of the NP-SP phase boundary can be tuned using parametric driving: the critical exponent of the static system (1, for the steady-state scenario) can be continuously reduced on increasing the driving strength. On the contrary, the phase boundary that separated the NP from the D-NP is characterized by a dynamical divergence of the excitation number of the incoherent photons.

The driven-dissipative DM unveils also a fascinating entanglement dynamics. When the system is not coupled to an environment a finite entanglement between the cavity field mode and the atoms can be sustained in the driven NP. The amount of entanglement is affected by the strength and frequency of the periodic modulation. While in the driven NP the atom-field entanglement displays a bounded oscillatory behavior, it transitions to monotonously increasing on approaching the phase boundary. All of this changes dramatically in the presence of dissipation. When the system weakly interacts with a thermal environment, entanglement can still be generated from initially separable states, but only for a finite time. In the dissipative system scenario the atoms and field disentangle in finite times (sudden death). This behavior clearly distinguishes from the one of decoherence, which is usually asymptotic in time. Changing perspective to the phase-space representation of quantum mechanics allowed us to understand that the entanglement generation is mostly due to the squeezing of the NM on the verge of the instability.

The formalism developed in this chapter has proved very useful in the analysis of the driven NP. In the future, it would be very interesting to extend this formalism to successfully describe the driven SP, which would provide a complete characterization of the phase transition between the NP and the SP. We expect the physics of the driven SP to be different than that of the driven NP due to the underlying different nature of the respective phases of the static Dicke model: the SP is ergodic,

while the NP is not [107, 169]. Likewise, one would also need a trustworthy description of the D-NP. We believe that, in principle, the EOM approach developed here can be generalized to also study the D-NP, provided one has a good starting description of the excitation Hamiltonian. The method can also be applied to other models of interest in the field of quantum optics like the driven Lipkin-Meshkov-Glick model with parametric driving [170] or the DM subject to an external driving field. Further interesting directions include the study of the influence of non-Markovian baths on such dissipative phase transitions. The formalism developed here provides a rigorous framework to approach these interesting problems.

IV

Parametric instabilities of a BEC in a cavity

Never make a calculation before you know the answer.

John Wheeler's motto

THE Dicke-Hepp-Lieb superradiant phase transition hosted by the Dicke model (DM) was predicted in 1973 [20, 105]. However, due to fundamental and technological reasons, it was experimentally observed only a few years ago in a weakly interacting cold bosonic gas coupled to a high finesse optical cavity [37, 43]. In this system the internal electronic degrees of freedom of the two-level systems are replaced by transitions between atomic momentum states and superradiance manifests itself via the spontaneous formation of a lattice supersolid [44].

In view of the above, the cold atom system appears as the natural candidate to further explore the physics of the periodically driven DM studied in Chapter III. Interactions between the atoms and dissipation due to photon losses through the cavity mirrors naturally occur in it. Moreover, easy implementations of parametric modulations in a wide range of frequencies makes it the perfect realistic system in which to study the influence of drive, interactions as well as dissipation. Concretely, in the experimental setup of the Esslinger group [37, 43] the effective atom-field coupling strength can be tuned by varying the amplitude of a pump

laser. A parametric modulation of this coupling, as discussed in Chapter III, can therefore be achieved by changing the intensity of the pump laser periodically in time around a static value.

In the previous chapter we studied the impact of parametric driving in the idealized DM and we discussed the new phases emerging due to many-body parametric resonance. Here, we would like to investigate the realistic model of an interacting Bose gas coupled to a cavity and subject to a modulation of the laser pump amplitude to see how parametric resonance emerges in this system and how heating manifests in real systems. As this involves studying a quantum many-body problem with time dependence, we resort to numerical methods. We thus exploit the capabilities of a powerful numerical method, the Multi-Configurational Time-Dependent Hartree method for indistinguishable particles (MCTDH-X), to investigate the dynamics of a Bose-Einstein condensate (BEC) coupled to an optical cavity, where the light-matter coupling is parametrically modulated. As opposed to Ref. [21], where the phase diagram of the driven-dissipative DM is obtained via mean-field analysis and in steady-state, we obtain here the phase diagram of the cavity-BEC system for experimentally achievable time scales and beyond this approximation.

The chapter is structured as follows. We present the model describing a driven-dissipative cavity-BEC system in Sec. IV.1 and outline how the given setup maps to the DM in the static case. In Sec. IV.2, we introduce the emergence of a many-body dynamical phase which has no counterpart in the equilibrium setting. We will clarify that the parameter space in which it appears can be inferred from the appearance of the D-NP in the modulated DM. By mapping the cavity-BEC system to the periodically driven DM (cf. Chpt. III) we provide indeed an analytical understanding of the numerically obtained phase boundaries. These are in good agreement with the theoretical predictions. We also fully characterize the phases and the heating characteristics in all these phases in Sec. IV.3. We found that the heating signals the breakdown of the mapping to the DM, whose validity is questioned in Sec. IV.4. This mapping starts to crumble when entering the new nonequilibrium phase. Lastly, in Sec. IV.5 we outline some interesting results obtained in related problems of multicomponent quantum gases as well as the emergence of strongly correlated phases of matter in these systems. We conclude by summarizing the main findings of this work and providing a final per-

spective of possible future research directions in Sec. IV.6.

The contents of this chapter are largely included in References [45] and [171, 172].

IV.1 Model

The BEC comprises N interacting atoms and is dispersively coupled to a high-finesse optical cavity with a single mode of frequency ω_c, see Fig. IV.1(a). The atoms of the BEC have a transition frequency ω_a and are coherently driven by a transverse pump laser of frequency ω_p. In the dispersive-coupling regime, if the atoms are strongly detuned in the rotating frame, i.e., $\Delta_a = \omega_p - \omega_a$ is large, one can adiabatically eliminate the excited atomic levels [173] to obtain the following effective Hamiltonian for the coupled cavity-BEC system in the rotating frame:

$$\mathcal{H}_{\mathrm{BEC}} = \int \mathrm{d}^3 r\, \hat{\Psi}^\dagger(\mathbf{r},t) \left\{ -\frac{\hbar^2}{2m}\nabla^2 + V_{\mathrm{trap}}(\mathbf{r}) + \frac{U}{2}\hat{\Psi}^\dagger(\mathbf{r},t)\hat{\Psi}(\mathbf{r},t) \right\} \hat{\Psi}(\mathbf{r},t)$$
$$+ \int \mathrm{d}^3 r\, \hat{\Psi}^\dagger(\mathbf{r},t) \left\{ \frac{\hbar}{\Delta_a} \left[h^2(\mathbf{r},t) + g^2(\mathbf{r})\hat{a}^\dagger\hat{a} + h(\mathbf{r},t)g(\mathbf{r})(\hat{a}+\hat{a}^\dagger) \right] \right\} \hat{\Psi}(\mathbf{r},t)$$
$$- \hbar\Delta_c \hat{a}^\dagger\hat{a}. \tag{IV.1}$$

The atoms in the BEC are described by bosonic field operators $\hat{\Psi}^{(\dagger)}(\mathbf{r},t)$ while $\hat{a}^\dagger$ and $\hat{a}$ describe the cavity mode. All operators obey bosonic commutation relations. For the sake of computational simplicity, in the following we restrict ourselves to the one-dimensional problem along the cavity axis x. The atoms are subjected to a harmonic trapping potential $V_{\mathrm{trap}}(x) = m\omega_x^2 x^2/2$ and interact through contact interactions with the strength $U = 4\pi\hbar^2 a/m$ where a is the s-wave scattering length and m the mass of the atom [59, 123, 174]. The atoms are driven by a transverse pump field described by the mode-function $h(\mathbf{r},t) = h(z,t) = \eta_p(t)\cos kz$ while the cavity mode function is $g(\mathbf{r}) = g(x) = g_0 \cos kx$. Here η_p is the pump rate, k the wavelength of the light and g_0 the atom-cavity coupling. The last two terms in the Hamiltonian describe the atom-cavity interaction. The $g^2(\mathbf{r})$ term arises directly from the cavity mode function while the $h(\mathbf{r},t)g(\mathbf{r})$-term results from the interference between cavity and pump fields.

For static pump amplitudes a mean-field analysis for large N and $V_{\mathrm{trap}}(\mathbf{r}) = 0$ using the Gross-Pitaevskii equation shows a $\mathbb{Z}_2$-symmetry

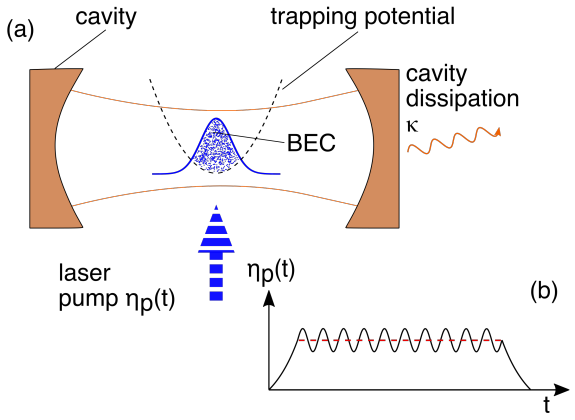

Figure IV.1: (a) A BEC in a transversely pumped dissipative cavity, subject to an external harmonic potential of frequency ω_x. (b) Laser pump profile $\eta_p(t)$, comprising a ramp-up, a sinusoidally modulated plateau, and a ramp-down.

breaking transition; as the pump power increases, the system goes from a normal phase (NP) with no photons in the cavity to a superradiant phase (SP), where the cavity field is a coherent state [37, 120, 173]. In the SP, the atoms spontaneously self-organize into either an even or an odd lattice structure with a spacing $\lambda = \frac{2\pi}{k}$ [37], cf. Fig. IV.2. Note that, in the two-dimensional experimental setup, the entrance into the SP is accompanied by the formation of a checkerboard lattice potential inside the cavity [37]. In our one-dimensional simulation, the system minimizes its energy when either all the atoms are localized at the maxima or minima of this periodic potential; this translates into two lattice configurations associated with a broken $\mathbb{Z}_2$ symmetry of the untrapped system, denoted by *even* or *odd* lattice. Note also that the self-organization has been proposed even in the absence of a cavity [175]. The relevant order parameter to describe this phase transition is $\Theta \equiv \langle\psi|\cos kx|\psi\rangle$: $\Theta = 0$ in the NP and $\Theta \neq 0$ in the SP. The quantity Θ – by definition it measures the overlap between the atomic wave function and the $\cos kx$ mode profile – essentially counts the population imbalance between odd and even lattice sites in the SP [37].

The same physics is well-described by a mapping to the DM Hamiltonian, with the internal electronic degrees of freedom of the atoms re-

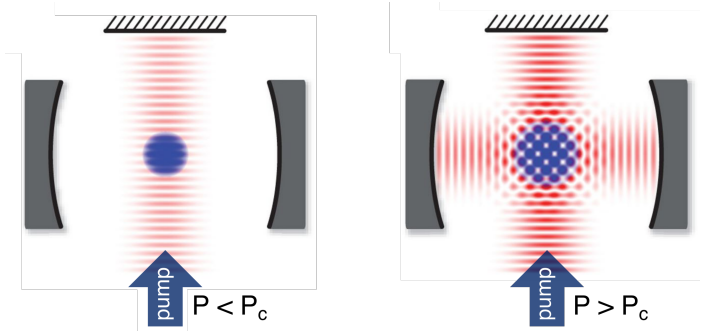

Figure IV.2: The self-organization transition of the cavity-BEC system. When the strength of the pump laser is below threshold (left), denoted by P_c, the system is in a unordered state and light is scattered incoherently in the cavity. Above threshold (right), the atoms self-organize. Adapted from Ref. [37].

placed by transitions between momentum states. It is here assumed that only the lowest $\pm k$-modes of the atoms are populated [37, 120]. The main idea is to expand the field operator $\hat{\Psi}$ in terms of the lowest-energy state ψ_0 and the excited state ψ_1, to which ψ_0 couples through the photons that scatter from the pump field into the cavity mode [37]. At the level of a single atom, this process can be seen as follows. An atom in the ground state $|p_x\rangle = |0\rangle$, i.e. characterized by zero momentum (along the cavity axis x), can reach one of the excited states $|p_x\rangle = |\pm k\rangle$ when scattering with a photon coming from the laser field [37]. The derivation of the Dicke Hamiltonian is obtained by inserting the expansion $\hat{\Psi} = \psi_0\hat{c}_0 + \psi_1\hat{c}_1$, with $\hat{c}_0$ and $\hat{c}_1$ bosonic operators, into the many-body Hamiltonian[1] (IV.1) and introducing a Schwinger representation as: $\hat{J}_- = \hat{c}_0^\dagger\hat{c}_1$, $\hat{J}_+ = \hat{c}_1^\dagger\hat{c}_0$ and $\hat{J}_z = (\hat{c}_1^\dagger\hat{c}_1 - \hat{c}_0^\dagger\hat{c}_0)$, where $J_\pm$ and J_z satisfy the standard angular-momentum commutation relations. This leads to the following Hamiltonian [37]

$$\hat{H} = \omega\hat{a}^\dagger\hat{a} + \omega_a\hat{J}_z + \frac{\lambda}{\sqrt{N}}\left(\hat{a}^\dagger + \hat{a}\right)\left(\hat{J}_+ + \hat{J}_-\right) + \frac{U_0}{4}\left(\hat{J}_z + \frac{N}{2}\right), \tag{IV.2}$$

[1] We stress again the fact that the trapping potential as well as the potential arising from the standing-wave pump field are here ignored (see Ref. [37]).

where constant terms have been omitted. One can clearly see that, apart from the term appearing in the second line, this is nothing but the Dicke Hamiltonian [cf. Eq. (III.1)]. The last term can indeed be neglected for parameters close to the NP-SP boundary, i.e. as long as the system is not in the deeply organized phase[2]. In the cavity-BEC realization, the atomic level spacing ω_a that appears in the Hamiltonian (IV.2) corresponds to the energy difference between the momentum states, i.e. $\omega_a = \hbar^2 k^2/m$. The frequency of the cavity field is given by $\omega = -\Delta_c + NU_0/2$, with $U_0 = g_0^2/\Delta_a$ encoding the light shift of a single maximally-coupled atom [37]. The atom-field coupling strength can be tuned by varying the amplitude of the transverse pump laser and reads $\lambda = \eta_p\sqrt{N}/2$ [37].

After having presented the static cavity-BEC system and the way in which it realizes the DM, we now illustrate the effects of adding a periodic modulation of the laser pump. In the system described by the Hamiltonian (IV.1) we thus consider a time-dependent pump amplitude in the plateau [see Fig. IV.1 (b)] given by

$$\eta_p(t) = \eta_p^0\big(1 + \alpha \sin\left(2\pi t/T\right)\big). \tag{IV.3}$$

We will demonstrate that this periodic drive leads to a new phase of matter. We explicitly include the cavity dissipation and we consider system parameters which describe the experimental system studied in Refs. [37, 43] (see Appendix D). For the system under consideration, the cavity dynamics follows that of the atoms closely, because the detuning Δ_a is much larger than the other energy scales. This is known as the dispersive-coupling regime, in which the atomic excitations are heavily suppressed, and is the one realized in the experiment [37]. The equation of motion obeyed by the cavity field is given by [176] (see also Appendix E):

$$\frac{\partial}{\partial t}\hat{a} = \left[i\Delta_c - \frac{i}{\Delta_a}\int \mathrm{d}x\, \hat{\rho}(x) g^2(x) - \kappa\right]\hat{a} - \frac{i}{\Delta_a}\int \mathrm{d}x\, \hat{\rho}(x) h(t) g(x), \tag{IV.4}$$

where κ is the dissipation rate. All other quantities are defined as in Eqs. (IV.1) and (IV.3). In the approach used for our investigation, the cavity is assumed to be in a coherent state with no cavity fluctuations.

[2]This would require the retention of higher momentum states and hence break the approximation based on the truncation of the Hilbert space to only contain the two lowest momentum states. The two approximations are therefore consistent with each other (cf. Ref. [37])

The operator $\hat{a}$ is hence replaced by its expectation value $\langle \hat{a} \rangle \equiv a$ in the equations of motion. Under this condition, the cavity population obeys the following dissipative EOM with a rate κ (cf. Appendix E):

$$\frac{\partial}{\partial t} a = i\big[\Delta_c a - U_0 \mathcal{B} a - \Theta \eta_p(t)\big] - \kappa a, \tag{IV.5}$$

where $\mathcal{B}$ is the so-called bunching parameter and is defined as $\mathcal{B} = \langle \psi | \cos^2 kx | \psi \rangle$. In this equation the atomic density distribution enters through Θ and $\mathcal{B}$; the dynamical evolution of the atoms is then studied using the MCTDH-X [56, 177–179] (see Sec. I.4 for details), which has been very successful in describing the dynamics of bosonic systems [56, 57, 178–181]. Here, for the first time, we apply the method to a periodically driven many-body system coupled to an optical cavity. All things considered, we stress that the atoms are treated within the MCTDH-X approach and, as such, physics beyond that of the mean-field approximation is retained. On the contrary, the cavity field is only described by a complex field amplitude and thus fluctuations are not included.

IV.2 Many-body parametric resonance

Before running the simulations for the periodically driven system, we benchmarked the numerical method by studying the static system. We reproduced the undriven (η_p, Δ_c)-phase diagram obtained in Ref. [37], cf. Fig. IV.3. We remark that the parameters used for all our simulations agree with the experimental setup of the Esslinger's realization [37] and are listed in Appendix D. In the rest of the chapter all the results will be in terms of dimensionless variables as explained therein. We used the time-dependent transverse pump protocol illustrated in Fig. IV.1(b) (see red dashed line) with the modulation amplitude $\alpha = 0$ in Eq. (IV.3). At time $t = 0$, the cavity is decoupled from the BEC in the trap.

The pump strength $\eta_p(t)$ is ramped up until it approaches a constant value η_p^0. In this plateau region we then obtain either the NP, where $\Theta = 0$ (see Fig. IV.3, top right), or the SP where $\Theta \neq 0$ (see Fig. IV.3, bottom right). For the case studied here, even when the atoms self-organize – either in the even or odd lattice – a substantial fraction of the atoms is still in the condensate. This aspect will be further explored in Sec. IV.5. For $N = 1000$ particles, converged results[3] are obtained using $M = 1$

[3] What is meant here is the numerical converge of the MCTDH-X.

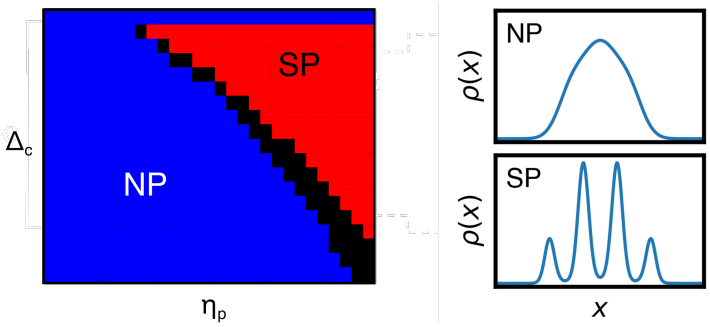

Figure IV.3: Phase diagram of the static cavity-BEC setup (left) and representative density profiles (right) for parameter values belonging to the NP (top figure) and SP (bottom figure).

orbital in the MCTDH-X approach. Contributions from $M > 1$ orbitals are negligible. For this $M = 1$ case, MCTDH-X corresponds to the mean-field solution obtained using the time-dependent Gross-Pitaevskii equation [59]. We also verified that our results recover the scaling invariance under $N \to N'$ provided [173]

$$g_0 \to \sqrt{\frac{N}{N'}} g_0, \quad U \to \frac{N}{N'} U, \quad \eta_p^0 \to \sqrt{\frac{N}{N'}} \eta_p^0 .$$

We now discuss a non-zero modulation α and assess the nature of the parametrically driven system when it is driven starting either from the NP or from the SP. For a fixed detuning $\Delta_c = -2\pi \cdot 10.08\,\text{MHz}$, we select two representative points close to the NP-SP phase boundary of the static pump simulations (see inset in Fig. IV.4). The chosen values are $\eta_p^{0,\text{NP}} = 2\pi \cdot 3.28\,\text{kHz}$ for the NP and $\eta_p^{0,\text{SP}} = 2\pi \cdot 4.79\,\text{kHz}$ for the SP (cf. orange stars in the inset). Similarly other pairs of points across the SP-NP phase transition lead to analogous results. Note that α is chosen to be small enough, so that the instantaneous $\eta_p(t)$ never crosses the static phase boundaries. In the course of this thesis we have encountered the phenomenon of parametric resonance both in classical (cf. Sec. II) and in quantum systems (cf. Sec. III). We have seen that it emerges whenever the modulation frequency hits the resonance condition $\omega_p = 2\omega_0/n$ (n integer), where ω_p indicates the driving frequency and ω_0 the natural frequency of the undriven system. In the same spirit, the modulating

frequency $\omega \equiv 2\pi/T$ is here chosen to be close to twice the gap to the lowest polaritonic excitation in the system; this corresponds to the case in which parametric driving is most effective. Note that in view of the driven DM discussed in Sec. III, the polaritons – this is a technical name used in this field – are nothing but the normal modes. The approximate polaritonic gap is determined by mapping the driven cavity-BEC to the DM, see Appendix F. We obtain two polaritonic modes for each phase [107]: a very high energy branch, $\epsilon_+^{\mathrm{NP/SP}}$ proportional to Δ_c, and a low energy branch $\epsilon_-^{\mathrm{NP/SP}}$ proportional to the atomic recoil energy $2E_r = \frac{\hbar^2 k^2}{m}$,

$$(\epsilon_-^{\mathrm{NP}})^2 \approx E_r^2\left[1 - (\eta_p^0/\eta_{p,c})^2\right], \tag{IV.6}$$

$$(\epsilon_-^{\mathrm{SP}})^2 \approx E_r^2\left[(\eta_p^0/\eta_{p,c})^4 - 1\right]. \tag{IV.7}$$

The energy of the lower polaritonic branch goes to zero at the QPT where $\eta_p \to \eta_{p,c}$ (see inset in Fig. IV.4). In what follows, in order to study the impact of parametric driving on the cavity-BEC system we simulate its full time-evolution as a function of the modulation period T and strength α starting from both NP and SP. We will demonstrate that both phases show a parametric instability to a different phase of matter.

The results for the phase diagram of the modulated cavity-BEC system as a function of the drive amplitude α and period T are summarized in Fig. IV.4. The phase boundaries have been obtained by evaluating the order parameter Θ. While in the NP it is very small, where deviations from zero are due to the confining harmonic potential, and in the SP it has a sizable finite value, the behavior is very different in the new dynamical phase. In this novel phase, Θ shows an oscillatory behavior with approximately zero mean; deviations can be again traced back to trap contributions. In the same figure, we have also superimposed a color plot of the time averaged energy profile, in which the black regions indicate no heating while the coloured tiles indicate heating. In the upper panel, corresponding to driving from the NP, the phase boundary, obtained from the evaluation of Θ, is indicated with a white dashed line. The energy of the BEC substantially increases only for higher values of α. For the lower panel the transition from low to high energy zones coincides with the phase boundary obtained from Θ. Both phase diagrams show the emergence of a many-body parametric resonance: the static phases display parametric instability lobes – reminiscent of Arnold lobes for Mathieu oscillators – for certain resonant values of T [69, 70]. This is

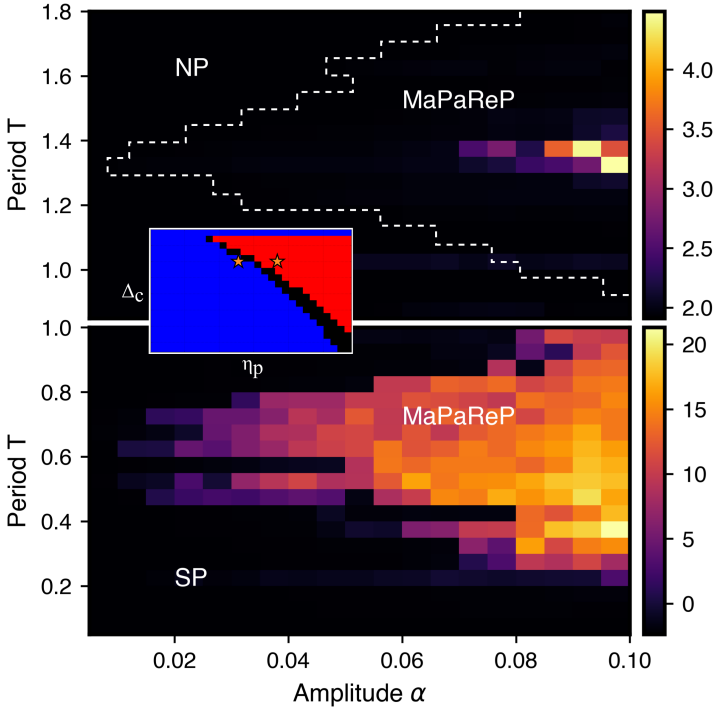

Figure IV.4: Phase diagrams of the parametrically driven BEC in a cavity as a function of the drive amplitude α and period T. The BEC is made of $N = 1000$ bosons. They are superimposed on the average heating of the system. The inset shows the undriven phase diagram and the stars indicate the chosen values of η_p^0. All quantities shown are dimensionless, see Appendix D.

IV

related to the fact that in the DM, polaritonic excitations are effectively described by the physics of two coupled POs, see Appendix F. We anticipate here that for certain thermalizing regions in the phase diagram, however, the mapping to the DM breaks down, as higher momentum states are populated, cf. Sec. IV.4 (see also Ref. [180]). As the parameters (T, α) are varied, the underlying undriven NP/SP becomes unstable and the system transitions to a new phase which we term the many-body parametric resonance phase (MaPaReP). As anticipated above, in this phase the order parameter $\Theta(t)$ shows oscillatory behavior in time with zero mean (excluding trap contributions). We would like to draw atten-

tion to the new name introduced here (i.e. the MaPaReP) for a phase that resembles the D-NP discussed in Sec. III. At its heart the MaPaReP could be seen as a manifestation of the D-NP and the driven DM provides an approximate understanding of it. However the phase addressed here appears in the context of a complex, interacting many-boson system and is more complicated than the D-NP. In the present study, we go beyond the oscillatory nature of the coherent photon emissions inferred in Ref. [21] and characterize the new phase by an unexpected dynamical superlattice switching where only a fraction of the atoms participate. Also, we will see in Sec. IV.4 that on entering the MaPaReP the DM fails to fully characterize the physics of the cavity-BEC system, i.e. the mapping to the DM does not provide a satisfactory description anymore [cf. Eq. (IV.2)].

The instability lobes seen in Fig. IV.4 differ greatly from the standard Arnold lobes for POs described by the Mathieu equation[4] [68]. The reason for this simply lies in the different functional form of the parametric modulation: it given by a simple cosine function for the Mathieu case, and by more complicated expressions in the present case, cf. Appendix F. While the frequencies at which Arnold tongues appear only depend on the periodicity of the Floquet drive, their exact shape depends on the precise functional form of the driving term. The periods around which the Arnold lobes of the cavity-BEC system are centered can be calculated as follows. In both phases, the dynamics is essentially governed by a classical Hill equation [69], see also Appendix F,

$$\ddot{x} + \gamma\dot{x} + [\epsilon_-^{\mathrm{NP/SP}}(t)]^2 x = 0, \tag{IV.8}$$

where γ is some effective damping and $\epsilon_-^{\mathrm{NP/SP}}(t) \equiv \epsilon_-^{\mathrm{NP/SP}}(\eta_p(t))$. For the sake of completeness, we show here the explicit expression for $\epsilon_-^{\mathrm{NP}}(t)$ (see also Appendix F), which reads

$$\left(\epsilon_-^{\mathrm{NP}}\right)^2 = \omega_a^2 - 4\frac{\omega_a}{\omega_c}\left(\mu_0 + \alpha\cos(2\Omega t)\right)^2.$$

A similar expression for $\epsilon_-^{\mathrm{SP}}(t)$ is shown in the Appendix F. The parametric resonance condition is determined by $\epsilon_-^{\mathrm{NP/SP}}(t=0)/\omega = n/2$, $n \in \mathbb{N}_0$ whereas the structure of the instability lobes is determined by the detailed form of $(\epsilon_-^{\mathrm{NP/SP}})$. The many-body resonance periods in our

[4]The standard Mathieu equation is simply a special case of Eq.II.1, which we studied in relation to the classical oscillator, where the is no external forcing term.

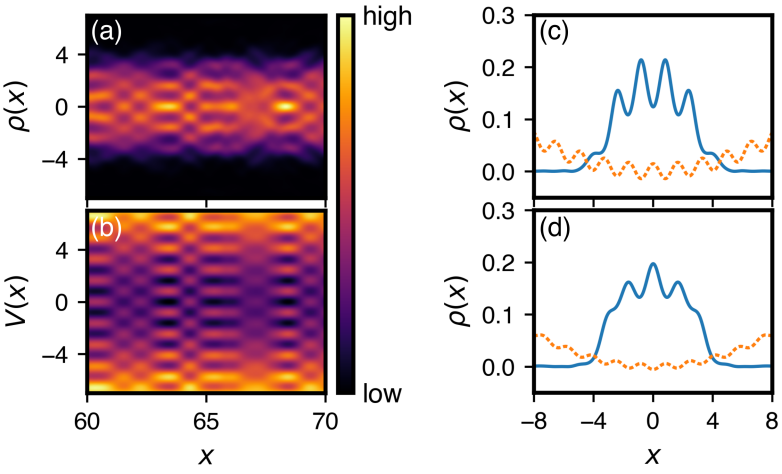

Figure IV.5: Time-evolution of the normalized density $\rho(x,t)$ (a) and the self-consistent one-body potential $V(x,t)$ (b) for a time-interval pertaining to the modulated plateau region for the many-body parametric resonance phase (MaPaReP). The maximum value reached by $\rho(x,t)$ is 0.296. The right panels show snapshots of the atomic density $\rho(x,t)$ (solid blue line) and one-body potential $V(x,t)$ (dashed orange line) seen by the atoms for times in which the BEC is mostly localized on the even (c) and odd sites (d) of the periodic lattice. The drive causes atoms of the BEC oscillate in time between even and odd sites of the periodic lattice in the MaPaReP. A unit of time corresponds to $0.63\,\mathrm{ms}$, while a unit of length to $0.48\,\mu\mathrm{m}$ (see Appendix D).

simulations are in good agreement with this simple resonance condition for $n = 1$, which predicts $T \approx 1.3$ and $T \approx 0.65$ when the system is driven starting from the NP or the SP. The resulting lobes are the first instability lobes, and the complex lobe shape in the SP case is qualitatively captured by Eq. (IV.8). Higher values of the cavity dissipation κ were found to smoothen the shape of the MaPaReP lobe and shift it to higher values of driving strength α. This is in accordance with the results from the stability analysis of Eq. (IV.8) for corresponding values of γ.

IV.3 Nature of the new phase

Insights into the nature of the different phases can be gained by an analysis of the time-evolved density $\rho(x,t)$ and the effective one-body potential $V(x,t)$ seen by the atoms (see Fig. IV.5). In the NP, the trapped BEC has a Gaussian-like profile (see Fig. IV.3, top right), $\Theta(t) \approx 0$ and $\rho(x,t)$ shows minimal changes as a function of time. In the SP, the atoms occupy the sites of the even or the odd lattice (see Fig. IV.3, bottom right) and Θ shows an oscillatory behavior with nonzero mean [cf. Fig. IV.6(b) light blue line]. In the modulated plateau region, cf. Fig. IV.1(b), the atoms remain in the lattice configuration chosen before the pump modulation was turned on. In the MaPaReP, however, the atoms and their potential systematically oscillate between the even and the odd lattice configurations [see Fig. IV.5(c) and (d)], hinting at a complex dynamical particle reconfiguration. As expected from the general solutions of Mathieu-like equations [69, 70], both the density and the one-body potential oscillate in time *not* at the underlying driving frequency (see Fig. IV.5), but rather *aperiodically*. We see that the lattice contribution to the effective potential seen by the atoms goes to zero at the point where the atoms transition between the even and the odd lattice.

We now discuss the stability of the different phases to heating, which is endemic to periodically driven interacting systems. In the NP and SP, the energy per particle oscillates (aperiodically) in time, but its time average stays constant [see Fig. IV.6(c) and (d)]. This suggests that the cavity-BEC system – even though it is an interacting system – does not absorb sufficient energy from the drive to counteract the dissipation. Therefore, for experimentally relevant timescales, the system does not heat up in the parametrically driven NP and SP. This hints towards the existence of a generalized Gibbs ensemble [182, 183] describing the NP and SP. In the MaPaReP, the system tends to heat up. The heating across the entire phase is illustrated by the coloured tiling of the phase diagrams in Fig. IV.4. Remarkably, the MaPaReP obtained from the NP (upper panel of Fig. IV.4) has minimal heating as compared to the MaPaReP obtained from the SP; it displays pre-thermalization-like plateaus where the average energy is approximately constant [see thick solid curve in Fig. IV.6(c)] and Θ shows a smooth oscillatory behavior. As the amplitude of the drive is gradually increased, the width of the plateaus shrinks and the condensate thermalizes more quickly. This rather stable behav-

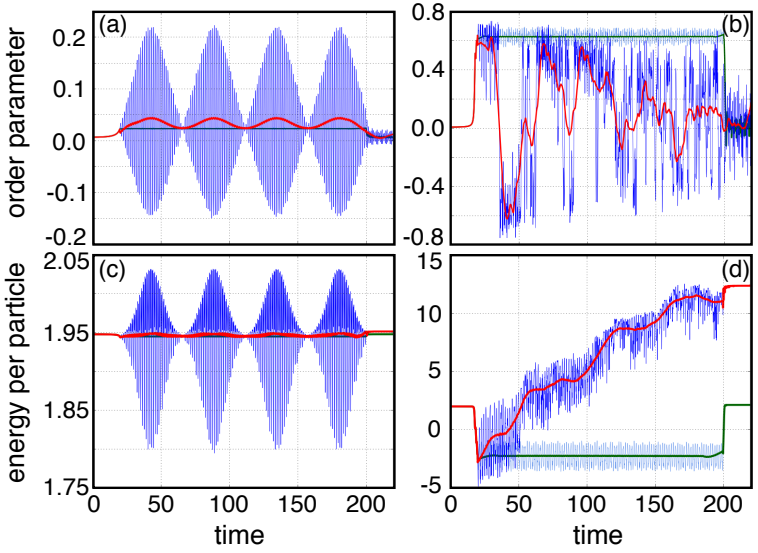

Figure IV.6: Time evolution of the order parameter (upper panels) and energy (lower panels) for a system driven from the NP (left panels) and SP (right panels). Thin lines represent the raw data, while running averages are marked as thick solid lines. Each panel features one time-evolution in the modulated NP or SP and another one in the corresponding MaPaReP at higher periods. The driving parameters α and T are $(0.005, 1.6)$ (light line) and $(0.05, 1.35)$ (dark line) for the left panels, and $(0.04, 1.6)$ (light line) and $(0.096, 1.6)$ (dark line) for the right panels. In the driven NP we note that the amplitude of the oscillations in the raw energy curve is very small and hence they are covered by their running average (thick dark line). All quantities shown are dimensionless, see Appendix D.

ior of the MaPaReP makes it easy to observe experimentally. The time scale over which the system absorbs energy depends crucially on the static pump rate η_p^0, the amplitude α and the period T.

In contrast to the gradual heating characteristics exhibited in the MaPaReP when driven from the NP, the MaPaReP obtained from the SP shows a much stronger thermalization (increase of about 500% in the considered time interval) to a trivial high temperature state [see Fig. IV.6(d)]. This fact could come from the underlying ergodic nature of the superradiant phase [107, 169], which is not shared by the normal phase. We also remark that within the present mean-field treatment of

the cavity field [cf. Eq. (IV.5)] we do not capture possible cooling effects induced by cavity fluctuations [119, 184]. This could prevent the activation of additional channels for cooling and could affect the overall heating rate of the system. However, we believe that the impact of cooling will be insufficient to stop the effects of parametric driving observed here. The corresponding order parameter Θ shows the even to odd lattice reconfigurations, but is increasingly noisy. The jump from the non-heating (SP) to the heating behavior (MaPaReP) is sharp, suggesting a first-order phase transition. We find that the energy in the MaPaReP averaged over a period initially increases linearly with time despite the cavity dissipation. The heating in the MaPaReP heralds the breakdown of the mapping to the DM, as the system populates other momentum states beyond the integrable subspace of the $\pm k$ momentum states, cf. Sec. IV.4 (see also Ref. [180]). Dissipation shifts the phase boundaries of the MaPaReP analogously to POs and affects the thermalization rate, but it does not change the qualitative features of the system within that phase. Similarly, different values of the cavity-atom coupling g_0 only affect the resonance condition of the instability lobes [37], shifting them vertically, but do not qualitatively change their physical picture. To summarize, heating profiles of the dissipative cavity-BEC system show an intriguing parametrically-induced crossover between an effective integrability (where the system does not heat up) and non-integrability (where the system heats up).

IV.4 Beyond the Dicke model

In Sec. IV.2, we have used the mapping between the cavity-BEC system and the DM (see Appendix F) to explain our numerical results. However, we should bear in mind that this is an approximation and is only valid as long as the two-level description of the BEC is adequate. Even if at its heart the physics of the cold atoms system is the one of the driven DM, which in turn is described by the physics of two POs, it retains a larger complexity than the toy model. We thus expect our system to show richer physics than that of the DM.

In light of these considerations, we investigate now the validity of the two-level picture in momentum space for the many-body parametric resonance phase (MaPaReP). Only in the regimes where the two-level description is valid the problem can be mapped to an effective paramet-

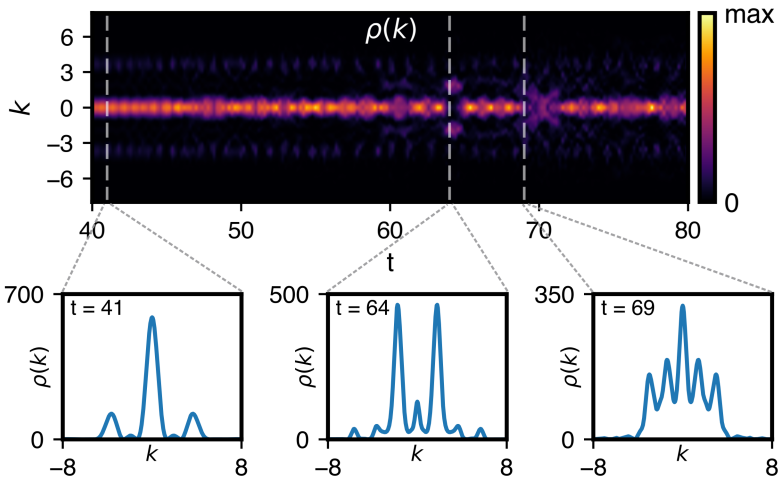

Figure IV.7: Illustration of the breakdown of the two-level picture in momentum space. Shown is the time-evolution of the momentum density $\rho(k,t)$ for times where the pump power is modulated in the many-body parametric resonance phase. The condensate was driven starting from the (static) SP with fixed parameters $\eta_p^{0,\mathrm{SP}} = 2\pi \cdot 4.54\,\mathrm{kHz}$ and $\Delta_c = -2\pi \cdot 10.08\,\mathrm{MHz}$. Snapshots for three different representative times ($t = 41, 64, 69$) are shown. The time-evolution is characterized by the emergence of peaks around multiples of $\pm k_c/2$ and later at arbitrary positions, signalling a self-interference of the condensate. All quantities shown are dimensionless, see Appendix D.

IV

rically driven DM. A breakdown of the two-level description therefore implies the appearance of physics beyond that of the DM.

In both the NP and SP, the underlying physics is well-approximated by a truncation of the description of the atoms to only contain the two lowest momentum states [37, 120, 185]. In the NP, the momentum density $\rho(k,t)$ displays a single peak at $k = 0$, while in the SP it shows two additional peaks at $k = \pm k_c$, where $k_c \approx 3.8$ is the quasimomentum of the spontaneously generated periodic potential. This value of the wave vector has been chosen to match the experimental setup [37].

The two-level picture remains approximately valid for a sizable region in the MaPaReP; the situation changes for certain thermalizing regions, where higher k-modes appear and the two-level picture breaks down. This is illustrated in Fig. IV.7, where we plot the time evolution of

$\rho(k,t)$ for times where the pump power us modulated in the MaPaReP [cf. Fig. IV.1(b)]. Before the periodic modulation starts the system is undriven, i.e. $\alpha = 0$ in Eq. (IV.3), and located in the SP region with parameters $\eta_p^{0,\mathrm{SP}} = 2\pi \cdot 4.54\,\mathrm{kHz}$ and $\Delta_c = -2\pi \cdot 10.08\,\mathrm{MHz}$. Shortly after the laser modulation starts, apart from the large peak at $k = 0$ corresponding to a flat density, $\rho(k,t)$ shows two sizable side-peaks at $k = \pm k_c$ and emerging peaks at $k = \pm k_c/2$ (see Fig. IV.7, left panel). At a later time, $\rho(k,t)$ displays sizable peaks around $k = 0, \pm k_c/2$ and smaller peaks at $k = \pm k_c, \pm 3k_c/2$ (see Fig. IV.7, middle panel). Even later, $\rho(k,t)$ develops additional peaks at momenta which are *not* integer multiples of $\pm k_c/2$, signalling a self-interference of the condensate. The increasing population of states beyond momenta $\pm k_c$ clearly indicates the inadequacy of the two-level description and hence the breakdown of the mapping to the Dicke model in the MaPaReP.

IV.5 Other aspects of cavity-BEC systems

We will now give a short overview of two projects in cold atomic gases that we contributed to as collaborators. We limit ourselves to explain the problem we studied and show the main results. The interested reader can find additional details in Refs. [171, 172].

In Ref. [171], we investigate weakly-interacting bosons in a high-finesse optical cavity. Similarly to the system studied in this chapter, the atoms are confined in the cavity through a harmonic potential and subject to laser pumping. This system is known to realize the superradiant phase transition of the DM discussed earlier. Moreover, recent studies showed that the SP can be further divided into two phases [186]: a self-organized superfluid (SSF) and a self-organized Mott insulator (SMI) phase. In our study, we provide an in-depth investigation of the transitions found in this system.

In Ref. [172], we consider again a laser-pumped one-dimensional BEC trapped by an external confinement harmonic potential, but made of two-component bosons (a spinor BEC). We find that for moderate pump powers the atoms self-organize, experiencing a transition from a NP to a SP. For larger pump powers, the system enters the fragmented superradiant phase identified by Lode and Bruder [180]. Remarkably, the fragmentation is accompanied by a progressive polarization of the ultracold atomic gas.

For more details about these two works, see Ref. [171] and [172].

IV.5.1 SSF-SMI transition of a BEC in a cavity

The cavity-BEC system treated here is the same one considered so far in this chapter, apart from the absence of a periodic modulation of the laser pump amplitude, that is $\alpha = 0$ in Eq. (IV.3). For parameter values close to the self-organization transition (see inset in Fig. IV.4) the system realizes the well-known superradiant phase transition of the DM [37]. Here we investigate a much wider parameter regime and explore the very rich physics governing the cavity-BEC system.

The Hamiltonian of the system, corresponding to the one-dimensional static version of (IV.1), is explicitly given by

$$\begin{aligned}\mathcal{H} = &\int \mathrm{d}x\, \hat{\Psi}^\dagger(x) \left\{ \frac{\hat{p}^2}{2m} + V_{\mathrm{trap}}(x) + \frac{U}{2}\hat{\Psi}^\dagger(x)\hat{\Psi}(x) \right\} \hat{\Psi}(x) \\ &+ \frac{\hbar}{\Delta_a} \int \mathrm{d}x\, \hat{\Psi}^\dagger(x) g^2(x) \hat{a}^\dagger \hat{a}\, \hat{\Psi}(x) \\ &+ \frac{\hbar}{\Delta_a} \int \mathrm{d}x\, \hat{\Psi}^\dagger(x) h(t) g(x) (\hat{a} + \hat{a}^\dagger) \hat{\Psi}(x) \\ &- \hbar \Delta_c \hat{a}^\dagger \hat{a}. \end{aligned} \tag{IV.9}$$

We made small changes in the notation used in Ref. [171] in order to preserve the consistency of the present thesis [cf. Eq. (IV.1)].

The approach we take here is fundamentally different than the one employed so far in this chapter. In Sec. IV.1, we replaced the operator $\hat{a}$ by a complex number a, which corresponds to a mean-field treatment of the cavity field [see Eq. (IV.5)]. Here instead, we adiabatically eliminate the fast mode of the cavity field by setting $\partial_t \hat{a} = 0$ in Eq. (IV.4), which corresponds to treating the cavity in its steady-state. In this case one obtains the following expression for cavity field operator:

$$\hat{a} = \frac{\frac{1}{\Delta_a} \int \mathrm{d}x\, \hat{\rho}(x) h(t) g(x)}{\Delta_c - \frac{1}{\Delta_a} \int \mathrm{d}x\, \hat{\rho}(x) g^2(x) + i\kappa}.$$

We remark that this treatment corresponds to the so-called *bad cavity* limit, in which the decay of the cavity field is much faster than the atomic motion [176]. In the present approximation, the cavity effectively provides an infinite-range two-body interaction potential between the

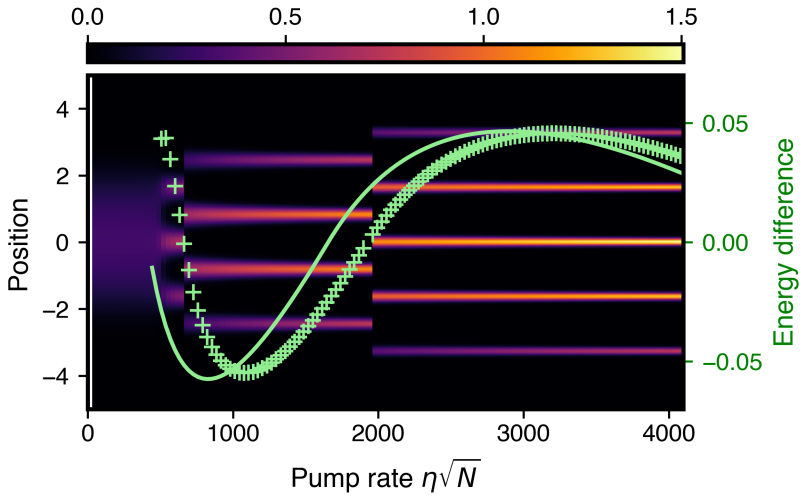

Figure IV.8: Switching between two lattice configurations in the ground state of the coupled cavity-BEC system. Shown is the density $\rho(x)$ as a function of the (normalized) laser pump rate. Superimposed are the numerical (green crosses) and analytical (green line) results for the energy difference between the lattice configurations. A positive energy difference favors a lattice with an odd number of peaks, while a negative energy difference an even lattice. See Ref. [171] for further details on the used parameter values.

atoms [187], and can be seen by inserting the found expression for the steady-state cavity field operator into the Hamiltonian (IV.9). The last three lines of this equation then simplify and lead to the following long-range interaction Hamiltonian

$$\mathcal{H}_{\mathrm{lr}} = \int \mathrm{d}x\mathrm{d}x'\, \hat{\Psi}^{\dagger}(x)\hat{\Psi}^{\dagger}(x')V_{\mathrm{lr}}\hat{\Psi}(x')\hat{\Psi}(x),$$

with the interaction potential $V_{\mathrm{lr}} \propto \cos(kx)\cos(kx')$.

One of the main findings of this work is shown in Fig. IV.8. It shows the density $\rho(x)$ of the BEC as a function of the scaled pump rate. The behavior of the system at low pump powers is now familiar to the reader. The system, initially in the NP with a Thomas-Fermi density profile, self-organizes into a lattice (SP). An important remark is here necessary. In this transition, the system goes from a superfluid NP to a self-organized, but still superfluid, SP. Note also that in our system the discrete $\mathbb{Z}_2$ sym-

metry of the DM is weakly broken due to the presence of the external trapping potential (cf. Sec. IV.1). As the pump rate increases further, the system, still self-organized, enters a Mott insulator phase and switches back and forth between the two configurations of the broken $\mathbb{Z}_2$ symmetry. By mapping the cavity-BEC system to the Bose-Hubbard (BH) model, we computed the energy difference between the different lattice configurations. This is shown by the green line in Fig. IV.8 and compared to the numerical result (green crosses). The BH model also correctly predicts that, as the pump rate increases, the number of density peaks will increase one at a time, accompanied by a switching of the lattice configuration.

The other main result that we will mention in this thesis is summarized in Fig. IV.9. It shows the momentum space density $\rho(k)$ as a function of the scaled pump rate for $N = 50$ [see Fig. IV.9(a)] and $N = 100$ [see Fig. IV.9(b)] particles. At low pump rates the NP-SP transition at $\eta\sqrt{N} \approx 500$ is clearly discernible, where $\rho(k)$ first characterized by a single narrow peak at $k = 0$ develops then additional peaks at $k = \pm k_c$. At higher pump rates, $\eta\sqrt{N} \approx 750$ for $N = 50$ and $\eta\sqrt{N} \approx 900$ for $N = 100$, the superfluidity is lost and the satellite peaks at $k = \pm k_c$ disappear. The system has transitioned from a SSF to a SMI phase. The height of the central peak of the momentum space density $\rho(k = 0)$, resp. its full width at half maximum (FWHM), shown as green dots, resp. light blue crosses in Fig. IV.9, provide important measures of superfluidity of the system [22, 186, 188, 189]. Fig. IV.9 reports a previously unseen reentrance of superfluid features in the Mott insulating phase. This happens at $\eta\sqrt{N} \approx 950$ for $N = 50$ and $\eta\sqrt{N} \approx 1050$ for $N = 100$ and is detectable in $\rho(k = 0)$ as well as in its FWHM. In Ref. [171], we argue that this reentrance is due to bosons moving from inner to outer peaks and emerges as a competition between the on-site repulsive interaction, governed by the pump rate, and the harmonic trapping potential.

IV.5.2 Two-component BEC in a cavity

The spinor BEC, made of N interacting atoms, is dispersively coupled to a high-finesse optical cavity, see Fig. IV.10. The setup constitutes a so-called double Λ configuration and is the same introduced in Ref. [190]. However, we go beyond [190] and include in our study interactions and correlations between the atoms as well as an external trapping potential.

The cavity-BEC system is described by a (position-space) Hamilto-

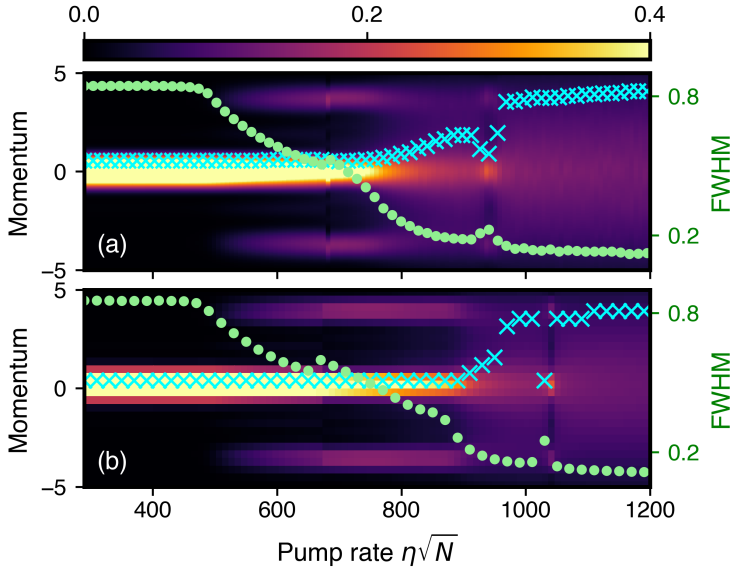

Figure IV.9: Tracing the self-organization transitions of a trapped BEC in a cavity. The momentum space density $\rho(k)$ is depicted as a function of the (normalized) laser pump rate. Superimposed are the height of the central peak $\rho(k=0)$ (green dots) and its FWHM (light blue crosses). See Ref. [171] for further details on the used parameter values.

nian of the form (I.22), with the only exception that the one-body $\hat{h}(\mathbf{r}_i, t)$ and the two-body Hamiltonian $\hat{W}(\mathbf{r}_i - \mathbf{r}_j, t)$ are now replaced by the matrices $\hat{\mathbf{h}}(\mathbf{r}_i, t)$ and $\hat{\mathbf{W}}(\mathbf{r}_i - \mathbf{r}_j, t)$ in order to accommodate the spinor nature of the BEC. The first part of the Hamiltonian, for a one-dimensional BEC, reads

$$\hat{\mathbf{h}}(x,t) = \sum_{\xi=\uparrow,\downarrow} \big[-\frac{1}{2}\partial_x^2 + V_\xi(x,t) \big] \mathbb{I}^\xi \mathbb{I}^{\xi,\top} + \mathbf{V}_{\text{cavity}}(x,t),$$

where $V_\xi(x,t)$ is the confinement potential, $\mathbf{V}_{\text{cavity}}(x,t)$ a cavity-mediated term and $\mathbb{I}^\xi$, with $\xi = \uparrow, \downarrow$, denotes the unit vector in the space of components. In the present work, we consider an identical parabolic confinement potential for both components of the atomic cloud, i.e. $V_\uparrow(x) = V_\downarrow(x) = x^2/2$. The action of the cavity photons on the atoms is described

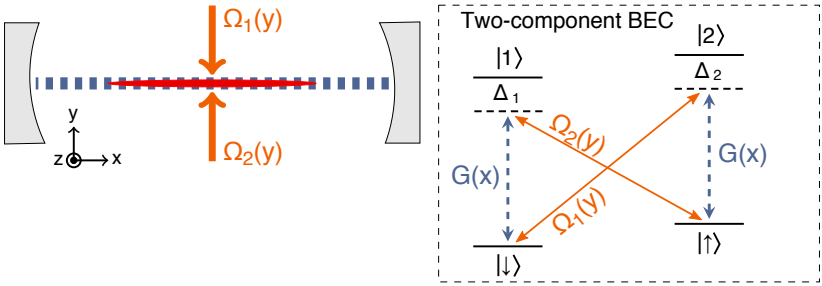

Figure IV.10: A BEC in a high-finesse optical cavity, transversely pumped by *two* lasers that couple to the transitions between the atomic states $|\downarrow\rangle$ and $|2\rangle$ and between $|\uparrow\rangle$ and $|1\rangle$ with Rabi frequencies Ω_1 and Ω_2, respectively. The coupling to the cavity is given by $G(x) = g_0 \cos k_c x$, with k_c the cavity wave vector. The pumps and the cavity are far-red-detuned from the atomic transition.

by the potential

$$\mathbf{V}_{\text{cavity}}(x) = \begin{pmatrix} V^{\uparrow\uparrow}_{\text{cavity}}(x) & V^{\uparrow\downarrow}_{\text{cavity}}(x) \\ V^{\downarrow\uparrow}_{\text{cavity}}(x) & V^{\downarrow\downarrow}_{\text{cavity}}(x) \end{pmatrix},$$

where $V^{\uparrow\uparrow}_{\text{cavity}}(x)$ and $V^{\downarrow\downarrow}_{\text{cavity}}(x)$ modify the one-body potential $V_\xi(x,t)$, while $V^{\uparrow\downarrow}_{\text{cavity}}(x) = V^{\downarrow\uparrow}_{\text{cavity}}(x)$ provide a cavity-mediated coupling between the two components. In the two-body interparticle interaction $\hat{\mathbf{W}}(x - x')$, we only consider contact interparticle interactions of atoms within the same component and neglect those between atoms in different ones. The exact functional form of all these terms can be found in [172].

The main results of this work are summarized in Fig. IV.11. We start the simulation with a BEC sitting at the bottom of the harmonic trap. The condensate is in the NP (cf. Sec. IV.1 and IV.2) and its (space) density is Gaussian-shaped [see Fig. IV.11(a)-(c)]. Accordingly, the momentum space density displays a peak at zero momentum, without any additional peaks [see Fig. IV.11(d)]. Upon increasing the pump power, the BEC transitions to a SP (cf. inset in Fig. IV.4), in which the atoms spontaneously self-organize into a periodic structure. The NP-SP transition is associated with a strong increase of the cavity field amplitude [see Fig. IV.11(g)]. The new phenomenon is here the clear appearance of polarization of the two-component BEC. Increasing the pump power

beyond the SP transition, the atomic ground state polarizes, eventually becoming fully ↑-polarized [see Fig. IV.11(b) and (c)]. The polarization[5] of the BEC as a function of the pump power η is explicitly shown in Fig. IV.11(i). Interestingly, the polarization of the atomic ground state comes along with a progressive fragmentation[6] of the condensate, see Fig. IV.11(h). The behavior of the ↑ component of the BEC is thus reminiscent of the fragmented superradiance found in Ref. [180]. We would like to conclude the discussion by noting that when the system enters the state of fragmented superradiance the standard two-level description in momentum space ceases to correctly describe the physics of the system. This is clearly shown in Fig. IV.11(d), where the momentum space density develops a rich structure not explained by the said picture.

IV.6 Conclusion and discussion

We have investigated the full time evolution of a BEC coupled to a dissipative optical cavity and subjected to a time-dependent transverse pumping laser power. This study is clearly inspired by the findings in Ref. [21] (see also Chpt. III), as well as the prospect of being easily realized in current experimental setups [37, 43, 44]. We show that in addition to the static normal and superradiant phases, parametric driving leads to the formation of a new many-body parametric resonance phase (MaPaReP), where the atoms switch quasiperiodically between the even- and odd-symmetric configurations. Such oscillations, absent in the undriven system, herald the breakdown of the system's mapping to the Dicke model. The boundaries of this dynamical phase are delineated by Arnold instability lobes (cf. Sec. II and III). Their existence is related to the phenomenon of parametric resonance already found in classical (cf. Sec. II) and quantum systems (cf. Sec. III). In this case the oscillators (addressed as polaritons above) correspond to the two NMs derived for the driven DM. The driven NP and SP are resistant to heating, while the

[5]We quantify the polarization by looking at the fraction of atoms in the ↑ component, i.e.

$$P = \frac{1}{N}\int \mathbb{I}^{\uparrow}\rho(x)\mathrm{d}x.$$

[6]The fragmentation is quantified by the fraction of atoms that does not correspond to the largest eigenvalue, denoted by n_1, of the reduced one-body density matrix, that is $F = 1 - n_1/N$.

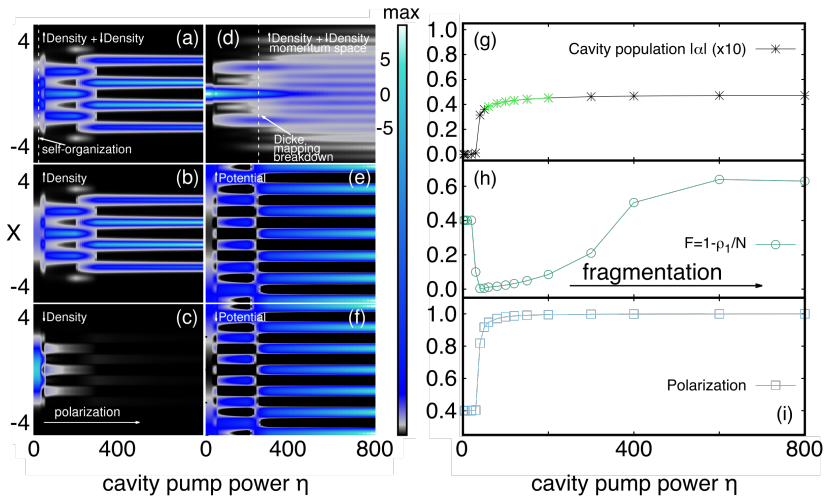

Figure IV.11: Left: self-organization and polarization of a two-component BEC in a cavity. (a) Total, (b) ↑-component, and (c) ↓-component densities as a function of the cavity pump power η. (d) Total momentum density and (e), resp. (f), cavity-modified potential $V_{\uparrow}(x) + V^{\uparrow\uparrow}_{\text{cavity}}(x)$, resp. $V_{\downarrow}(x) + V^{\downarrow\downarrow}_{\text{cavity}}(x)$. Right: cavity population (g), fragmentation (h), and polarization (i) of two-component bosons in a cavity. See Ref. [172] for further details on the used parameter values.

MaPaReP shows pre-thermalization and eventually thermalizes fully despite the presence of dissipation. In the present study, we observed that heating in the MaPaReP is stronger when obtained from the SP. This fact could come from the underlying ergodic nature of the superradiant phase [107, 169], which is not shared by the normal phase.

In the wider context of light-matter interactions and Floquet systems as a new frontier in condensed matter physics, our work makes a realistic prediction for a new phase of matter (the MaPaReP) in interacting Floquet systems. Furthermore, our work is a successful illustration of the MCTDH-X as applied to Floquet systems and highlights the power of this numerical method for dealing with interacting many-body systems. We believe that in the future it can be widely used in different fields of research.

Taking a step back, when comparing the analytical approach used in Chapter III and the numerical one used in this chapter we realize

that they are complementary. The former fully characterizes the driven NP and describes the fluctuations around the vacuum cavity state and the unexcited atomic ensemble. However, the validity of this analytical treatment is limited to the driven NP and cannot be used to explore the D-NP. On the contrary, the MCTDH-X allowed us to investigate the full phase diagram of the parametrically driven cavity-BEC system. Its drawback is that the cavity field is treated within the paradigm of mean-field theory and therefore fluctuations are inaccessible. Also, the very interesting entanglement dynamics between the atoms and the light field that was found in Chpt. III cannot be studied. This allows us to infer what a possible future direction of research could be; it would indeed be very interesting to extend the present approach to perform simulations in which the time-evolution also contains the cavity fluctuations.

To conclude, we collaborated to two other projects – not involving Floquet driving – that led to very interesting results. In the first one we considered the static cavity-BEC system described above and focused on the SP, which can be further divided into two phases: a self-organized superfluid (SSF) and a self-organized Mott insulator (SMI) phase. In the approach used here, the cavity effectively provides an infinite-range two-body interaction potential between the atoms. Instead, in the investigation proposed in this thesis the cavity potential was considered in such a way that it modifies the one-body potential appearing in the Hamiltonian. We demonstrate that when the pump rate reaches a high enough value the system is self-organized and enters a Mott insulator phase, where it switches back and forth between two lattice configurations. In the second one, we deal with a BEC made of two-component bosons. For large values of the pump laser field, the condensate first self-organises (NP to SP transition) and later enters a fragmented superradiant phase along with a progressive polarization of the ultracold atomic gas.

An interesting direction for future studies, which comes as a natural extension of our work, is the examination of the fermionic Dicke model. With the MCTDH-X it should be possible to investigate the phenomenon of fermionic superradiance in a system of ultracold (spinless) fermions in a transversely pumped cavity. Even more intriguing is the comparison between the physics of the said model under the effect of parametric driving and the bosonic one addressed in this thesis.

V

Conclusions and outlook

The scientist does not study nature because it is useful; he studies it because he delights in it, and he delights in it because it is beautiful. If nature were not beautiful, it would not be worth knowing, and if nature were not worth knowing, life would not be worth living.

Henri Poincaré

THE overarching topic of this thesis is the manifestation of parametric resonance in classical and quantum systems. The general framework is hence the one of physical phenomena far from equilibrium.

For a classical oscillator, even though the phenomenon of parametric resonance is eliminated by nonlinearities, the Arnold tongues of the linear system still play an important role. The system retains indeed a "memory" of the underlying instability boundary, across which its dynamical behavior changes qualitatively. Based on this observation, we developed a force detection scheme that explicitly exploits the interplay between nonlinearities and parametric drive. At a more fundamental level, we showed that the force detection scheme is based on a degeneracy lifting between parametric phase states induced by a periodic external force. Additionally, we also contributed to its first experimental realization using an experimental setup that consists in a doubly clamped steel string. Subsequent research proposed to use the same system as

a parametric symmetry breaking transducer and claimed that it is very robust against readout noise.

Parametric driving in quantum system is attracting more and more attention due to the prodigious number of out-of-equilibrium phenomena that do not have equilibrium counterparts. In the case of the Dicke model, which is the emblematic example of system exhibiting light-matter collective behavior, parametric driving of the atom-field coupling leads to a rich extension of the well-known static phase diagram. It was indeed shown that a new phase with complex phase boundaries emerges as a manifestation of many-body parametric resonance. A central insight provided by this thesis is the exploration of the very intriguing physics that emerges along the phase boundaries. The criticality of the usual transition between the normal and superradiant phase of the static model can be continuously modified by the nonequilibrium condition induced by the periodic drive. We found indeed that the divergence of the cavity fluctuations on approaching the phase boundary between the normal and superradiant phase depends on the driving parameters. Oppositely, the phase boundary between the normal and the dynamical normal phase is characterized by cavity fluctuations that diverge (polynomially) in time. The entanglement between the cavity field and the atoms also shows a very interesting behavior. While it display a bounded dynamics in the driven normal phase, it transitions to monotonously increasing on approaching the phase boundary. Another key result of our analysis concerns the effect of dissipation on the fate of entanglement. In the driven normal phase, we found entanglement sudden death, which can be retarded by the counteraction of the parametric drive. Furthermore, we showed that the entanglement generation that occurs starting from an initially separable state is mediated by the squeezing of the polariton – or normal mode – on the verge of the instability.

Realizing the Dicke phase transition is a formidable task due to the challenging problem of reaching the regime of strong coupling and it has been elusive for a long time. Few years ago it was finally observed in a weakly interacting cold bosonic gas coupled to a high-finesse optical cavity. In this realization the light-matter coupling strength can be tuned over a vast range by varying the amplitude of a pump laser. A parametric modulation of this coupling, in the same spirit of the modulated Dicke model discussed above, can therefore be achieved by changing the

intensity of the pump laser periodically in time around a static value. In the last part of this dissertation we studied the realistic model of an interacting Bose gas coupled to a cavity and subject to a modulation of the laser pump amplitude to see how parametric resonance emerges in this system. While the Dicke model considers the interaction between a field mode and the collection of many noninteracting two-level systems, the realistic system considered here is made of interacting Bosons. The fundamental problem of heating in driven open quantum systems is still an open question. A main result of our analysis shows that in addition to the static normal and superradiant phases, parametric driving leads to the formation of a new many-body parametric resonance phase (MaPaReP) where the atoms switch quasiperiodically between the even- and odd-symmetric lattice configurations. By mapping the system to the driven Dicke model we identified the boundaries of this phase of matter with the Arnold instability lobes of the corresponding normal modes. Remarkably, while the driven NP and SP are resistant to heating, the MaPaReP shows pre-thermalization and eventually thermalizes fully despite the presence of dissipation. Also, we showed that the MaPaReP is characterized by a mild heating when obtained from the normal phase, but by vigorous heating when obtained from the superradiant phase. We connected this result with the underlying ergodic nature of the superradiant phase as opposed to the normal phase.

Another intriguing result is obtained for the same cold atom system used in the previous study. Here we changed perspective though. The parametric driving is removed and the focus is on the deep superradiant phase. We discussed before that the system transitions from the normal to the superradiant phase on increasing the amplitude of the pump laser. This phase, characterized by the self-organization of the condensate, is a superfluid phase; it is thus called self-organized superfluid phase. As the pump rate increases further, the system, still self-organized, enters a Mott insulator phase (called self-organized Mott insulator phase) and switches back and forth between two lattice configurations corresponding to the broken $\mathbb{Z}_2$ symmetry of the untrapped system. Notably, for a specific pump amplitude we observed a reentrance of superfluid features in the Mott insulating phase. By mapping the cavity-BEC system to the Bose-Hubbard, we argued that this reentrance is due to bosons jumping from inner to outer peaks and emerges as a competition between the on-site repulsive interaction and the harmonic trapping potential. This

work highlighted the nontrivial role played by the trapping potential in cold atom experiments.

In the end, we considered a laser-pumped one-dimensional Bose-Einstein condensate made of two-component bosons. At low pump amplitudes, the system undergoes the well-known transition from the normal phase to the superradiant phase. However, for larger pump powers the system enters a fragmented superradiant phase accompanied by a progressive polarization of the spinor gas.

Appendix

A Normal mode transformations

Similarly to the static case [107] we first introduce position and momentum operators for the system operators

$$\hat{x} = \frac{1}{\sqrt{2\omega_0}}\left(\hat{a}^\dagger + \hat{a}\right), \quad \hat{p}_x = i\sqrt{\frac{\omega_0}{2}}\left(\hat{a}^\dagger - \hat{a}\right), \tag{V.1}$$

$$\hat{y} = \frac{1}{\sqrt{2\omega_0}}\left(\hat{b}^\dagger + \hat{b}\right), \quad \hat{p}_y = i\sqrt{\frac{\omega_0}{2}}\left(\hat{b}^\dagger - \hat{b}\right). \tag{V.2}$$

In terms of these operators the Hamiltonian (III.5) reads

$$\hat{H}_S(t) = \frac{1}{2}\left(\omega_0^2\hat{x}^2 + \hat{p}_x^2 + \omega_0^2\hat{y}^2 + \hat{p}_y^2\right) + 2\omega_0\lambda(t)\hat{x}\hat{y}. \tag{V.3}$$

Similarly to (V.1) and (V.2), we introduce position $(\hat{q}_{1,k}, \hat{q}_{2,k})$ and momentum $(\hat{p}_{1,k}, \hat{p}_{2,k})$ operators for the baths operators. The bath and interaction Hamiltonians then become

$$\begin{aligned}\hat{H}_B &= \frac{1}{2}\sum_k \omega_k^2\hat{q}_{1,k}^2 + \hat{p}_{1,k}^2 + \frac{1}{2}\sum_i \omega_i^2\hat{q}_{2,i}^2 + \hat{p}_{2,i}^2,\\ \hat{H}_I &= \sum_k 2g_k\sqrt{\omega_0\omega_k}\,\hat{x}\hat{q}_{1,k} + \sum_i 2g_i\sqrt{\omega_0\omega_i}\,\hat{y}\hat{q}_{2,i}.\end{aligned} \tag{V.4}$$

The total system can be fully separated by means of the following NM transformation $\hat{X}_\pm = (\hat{x} \pm \hat{y})/\sqrt{2}$ for the system and $\hat{\Pi}_k^\pm = (\hat{q}_{1,k} \pm \hat{q}_{2,k})/\sqrt{2}$ for the baths. Using these operators the system and interac-

tion Hamiltonians [see Eqs. (V.3) and (V.4)] read

$$\hat{H}_S(t) = \frac{1}{2}\left(\Omega_1^2(t)\hat{X}_+^2 + \hat{P}_+^2 + \Omega_2^2(t)\hat{X}_-^2 + \hat{P}_-^2\right),$$
$$\hat{H}_I(t) = \sum_k 2g_k\sqrt{\omega_0\omega_k}\,\hat{X}_+\hat{\Pi}_k^+ + \sum_i 2g_i\sqrt{\omega_0\omega_i}\,\hat{X}_-\hat{\Pi}_i^-,$$

A

where $\Omega_{1,2}(t)$ are given by Eq. (III.9) and $\hat{P}_\pm$ are the NM momentum operators corresponding to $\hat{X}_\pm$. Lastly, the Hamiltonians (III.10)-(III.12) are found by re-quantizing the system using the following NM operators

$$\hat{A}_1(t) = \frac{1}{\sqrt{2\Omega_1(t)}}\left(\Omega_1(t)\hat{X}_+ + i\hat{P}_+\right),$$
$$\hat{A}_2(t) = \frac{1}{\sqrt{2\Omega_2(t)}}\left(\Omega_2(t)\hat{X}_- + i\hat{P}_-\right),$$
$$\hat{C}_k = \frac{1}{\sqrt{2\omega_k}}\left(\omega_k\hat{\Pi}_k^+ + i\hat{\rho}_k^+\right),$$
$$\hat{D}_k = \frac{1}{\sqrt{2\omega_k}}\left(\omega_k\hat{\Pi}_k^- + i\hat{\rho}_k^-\right),$$

where $\hat{\rho}_k^\pm$ are the NM momentum operators corresponding to $\hat{\Pi}_k^\pm$. Putting these transformations together leads to the Bogoliubov transformations between the bosons $(\hat{a}, \hat{b}) \leftrightarrow (\hat{A}_1, \hat{A}_2)$, cf. Eq. (III.8), and $(\hat{c}_k, \hat{d}_k) \leftrightarrow (\hat{C}_k, \hat{D}_k)$.

B Solution for $\hat{F}(t)$

The EOM for the operators $\hat{F}(t)$ and $\hat{F}^\dagger(t)$ can be solved by means of a Green's function approach. We set

$$\hat{\mathbf{v}}(t) = \int_0^t \mathbf{\Lambda}(t,t')\hat{\mathbf{B}}(t')\mathrm{d}t' \,, \tag{V.5}$$

where $\hat{\mathbf{v}}(t) = (\hat{F}(t), \hat{F}^\dagger(t))^\top$, $\hat{\mathbf{B}}(t) = (\hat{B}(t), -\hat{B}^\dagger(t))^\top$ with $B(t)$ being the inhomogeneous term appearing in Eq. (III.19) and given by $\hat{B}(t) = \sum_k \tilde{g}_k(t)[\hat{C}_k(0)\mathrm{e}^{-i\omega_k t} + \hat{C}_k^\dagger(0)\mathrm{e}^{i\omega_k t}]$. Differentiating Eq. (V.5) with respect to t, together with the initial condition $\mathbf{\Lambda}(t,t) = -i\mathbb{I}_2$, leads to the following equation

$$\begin{aligned}\int_0^t \dot{\mathbf{\Lambda}}(t,t')\hat{\mathbf{B}}(t')\mathrm{d}t' = \mathbf{M}(t)\int_0^t \mathbf{\Lambda}(t,t')\hat{\mathbf{B}}(t')\mathrm{d}t' \\ - \int_0^t\int_0^s \tilde{\mathbf{K}}(t,s)\mathbf{\Lambda}(s,t')\hat{\mathbf{B}}(t')\mathrm{d}t'\mathrm{d}s \,,\end{aligned} \tag{V.6}$$

where

$$\tilde{\mathbf{K}}(t,s) = \tilde{K}(t,s)\begin{pmatrix} 1 & 1 \\ -1 & -1\end{pmatrix},$$

with $\tilde{K}(t,s) \equiv \omega_0 K(t-s)/\sqrt{\Omega_1(t)\Omega_1(s)}$ and

$$\mathbf{M}(t) = \begin{pmatrix} -i\Omega_1(t) & \dot{\phi}(t)/4\Omega_1^2(t) \\ \dot{\phi}(t)/4\Omega_1^2(t) & i\Omega_1(t)\end{pmatrix}.$$

The last term appearing in Eq. (V.6) can be transformed to

$$\begin{aligned}&\int_0^t\int_0^s \tilde{\mathbf{K}}(t,s)\mathbf{\Lambda}(s,t')\hat{\mathbf{B}}(t')\mathrm{d}t'\mathrm{d}s \\ &= \iint_{\mathbb{R}^2} \tilde{\mathbf{K}}(t,s)\mathbf{\Lambda}(s,t')\hat{\mathbf{B}}(t')\,\mathbb{1}_{\{0\le t'\le t,\, t'\le s\le t\}}\mathrm{d}s\mathrm{d}t' \\ &= \iint_{\mathbb{R}^2} \tilde{\mathbf{K}}(t,x+y)\mathbf{\Lambda}(x+y,x)\hat{\mathbf{B}}(x)\,\mathbb{1}_{\{0\le x\le t,\, 0\le y\le t-x\}}\mathrm{d}x\mathrm{d}y \\ &= \int_0^t\int_0^{t-x} \tilde{\mathbf{K}}(t,x+y)\mathbf{\Lambda}(x+y,x)\hat{\mathbf{B}}(x)\mathrm{d}y\mathrm{d}x,\end{aligned}$$

where $\mathbb{1}_{\{\cdot\in A\}}$ is the standard indicator function[1]. Here we have first used Fubini's theorem and then the substitution $(t',s) = (x, x+y)$. This

[1] The indicator function of a subset A of a set X is simply a function $\mathbb{1}_{\{\cdot\in A\}} : X \to \{0,1\}$ defined as $\mathbb{1}_{\{x\in A\}} \equiv 1$ if $x \in A$ and 0 if $x \notin A$.

result can be used to rewrite Eq. (V.6) as

$$\int_0^t \Big[\dot{\mathbf{\Lambda}}(t,x) - \mathbf{M}(t)\mathbf{\Lambda}(t,x) + \int_0^{t-x} \tilde{\mathbf{K}}(t,x+y)\mathbf{\Lambda}(x+y,x)\mathrm{d}y\Big]\hat{\mathbf{B}}(x)\mathrm{d}x = 0\,. \tag{V.7}$$

Since Eq. (V.7) has to be valid for every t, and since $\hat{\mathbf{B}}(x)$ can be, a priori, any (non-zero) operator-valued function, it follows that the time evolution of $\mathbf{\Lambda}(t,t')$ is governed by the following equation

$$\dot{\mathbf{\Lambda}}(t,t') - \mathbf{M}(t)\mathbf{\Lambda}(t,t') + \int_{t'}^{t} \tilde{\mathbf{K}}(t,s)\mathbf{\Lambda}(s,t')\mathrm{d}s = 0\,. \tag{V.8}$$

B

Note that $\mathbf{\Lambda}(s,t') = 0$ for $s < t'$ and it is equal to $-i\mathbb{I}_2$ for $s = t'$. In Eq. (V.8) the various times are therefore ordered according to $0 \leq t' \leq s \leq t$. At the end, using the fact that $\mathbf{\Lambda}(t,t')$ has the following form

$$\mathbf{\Lambda}(t,t') = \begin{pmatrix} \Lambda_1(t,t') & -\Lambda_2^*(t,t') \\ \Lambda_2(t,t') & -\Lambda_1^*(t,t') \end{pmatrix},$$

and that $B^\dagger(t) = B(t)$, we arrive at the time evolution of the operator $\hat{F}(t)$ given by Eq. (III.20).

Now that we have an expression for the operator $F(t)$ we can compute all the bath correlation functions. For the sake of brevity, we restrict ourselves to the explicit computation of $\langle \hat{F}^\dagger(t)\hat{F}(t)\rangle$ and, analogously to the main text, we only consider the first NM. The other correlation functions are computed in the very same way. We remind that the expectation value of the bath correlation function is given by $\langle \hat{F}^\dagger(t)\hat{F}(t)\rangle = \mathrm{Tr}\{\rho_{\tilde{B}_1}(0)\hat{F}^\dagger(t)\hat{F}(t)\}$, where the $\rho_{\tilde{B}_1}(0)$ is the initial density matrix of the first *NM* bath, cf. Eq. (III.6). Note that what we assumed is the initial density matrix of the *original system* bath – *not* the NM bath – to be in thermal equilibrium at temperature T, that is

$$\begin{aligned}\rho_{B_1}(0) &= \exp(-\beta\hat{H}_{B_1})/\,\mathrm{Tr}\{\exp(-\beta\hat{H}_{B_1})\} \\ &= \prod_i (1-\mathrm{e}^{-\beta\omega_i})\mathrm{e}^{-\beta\omega_i c_i^\dagger c_i}.\end{aligned}$$

However, do to the specific form of the Bogoliubov transformations between the bath operators $(\hat{c}_k,\, \hat{d}_k) \leftrightarrow (\hat{C}_k,\, \hat{D}_k)$, the NM baths turn out to be in thermal equilibrium at the same temperature T. Hence, the only nonvanishing initial expectation values between the operators $\hat{C}_k$ – the

same holds for the operators $\hat{D}_k$ – are given by

$$\begin{aligned}\langle C_k^\dagger(0)C_{k'}(0)\rangle &= \delta_{k,k'}n(\omega_k,T),\\ \langle C_k(0)C_{k'}^\dagger(0)\rangle &= \delta_{k,k'}(1+n(\omega_k,T)),\end{aligned} \tag{V.9}$$

where $n(\omega_k,T) = (\mathrm{e}^{\beta\omega_k}-1)^{-1}$ denotes the Planck distribution. Using the relations (V.9) we obtain the following expression for the bath correlation function

$$\begin{aligned}\langle \hat{F}^\dagger(t)\hat{F}(t)\rangle = \int_0^t \mathrm{d}t' \int_0^t \mathrm{d}t'' \left[\Lambda_1^*(t,t') + \Lambda_2(t,t')\right]\left[\Lambda_1(t,t'') + \Lambda_2^*(t,t'')\right]\\ \times \sum_k \tilde{g}_k(t')\tilde{g}_k(t'')\Big[2\cos\omega_k(t'-t'')n(\omega_k,T) + \mathrm{e}^{-i\omega_k(t'-t'')}\Big].\end{aligned}$$

The last line of this equation can be recast as

$$\frac{\omega_0 K_T(t'-t'')}{\sqrt{\Omega_1(t')\Omega_1(t'')}} \equiv \sum_k g_k^2\Big[\coth(\beta\omega_k/2)\cos\omega_k(t'-t'') - i\sin\omega_k(t'-t'')\Big],$$

where we have used the definition of $\tilde{g}_k(t)$, cf. Eq. (III.12). In the continuum limit, where we define $J(\omega) \equiv \sum_k g_k^2\delta(\omega-\omega_k)$, we get the result shown in Eqs. (III.24) and (III.25).

C TCL master equation

Similarly to the investigation of entanglement in Sec. III.5, we focus here on Gaussian states. As we discussed in the said section, the dynamics governed by the quadratic total Hamiltonian preserves Gaussian states. This argument makes clear that the master equation can only have at most bilinear terms in $\hat{a}$ and $\hat{a}^\dagger$. It is therefore of the following form:

$$\begin{aligned}\frac{\mathrm{d}}{\mathrm{d}t}\hat{\rho}_S(t) =& A\hat{a}\hat{\rho}_S + B\hat{\rho}_S\hat{a} + C\hat{a}^\dagger\hat{\rho}_S + D\hat{\rho}_S\hat{a}^\dagger \\ &+ E\hat{a}\hat{a}\hat{\rho}_S + F\hat{\rho}_S\hat{a}\hat{a} + G\hat{a}\hat{\rho}_S\hat{a} \\ &+ H\hat{a}^\dagger\hat{a}^\dagger\hat{\rho}_S + I\hat{\rho}_S\hat{a}^\dagger\hat{a}^\dagger + L\hat{a}^\dagger\hat{\rho}_S\hat{a}^\dagger \\ &+ M\hat{a}^\dagger\hat{a}\hat{\rho}_S + N\hat{\rho}_S\hat{a}^\dagger\hat{a} + O\hat{a}^\dagger\hat{\rho}_S\hat{a} \\ &+ P\hat{a}\hat{a}^\dagger\hat{\rho}_S + Q\hat{\rho}_S\hat{a}\hat{a}^\dagger + R\hat{a}\hat{\rho}_S\hat{a}^\dagger. \end{aligned} \tag{V.10}$$

If we impose hermiticity, that is $\hat{\rho}_S = \hat{\rho}_S^\dagger$, we find that the coefficients satisfy the conditions: $D = A^*$, $C = B^*$, $I = E^*$, $H = F^*$, $L = G^*$, $N = M^*$, $Q = P^*$. The second thing we want to ensure is that the master equation is trace preserving [135]. This amounts to requiring that $\mathrm{Tr}\{\frac{\mathrm{d}}{\mathrm{d}t}\hat{\rho}_S(t)\} = 0$, which imposes further conditions on the coefficients, i.e.

$$\begin{aligned} A + B = 0, \quad E + F + G = 0, \\ M + M^* + R = 0, \quad P + P^* + O = 0. \end{aligned}$$

Using all these relations, we can rewrite Eq. (V.10) as

$$\begin{aligned}\frac{\mathrm{d}}{\mathrm{d}t}\hat{\rho}_S(t) =& A[\hat{a},\hat{\rho}_S] - A^*[\hat{a}^\dagger,\hat{\rho}_S] - F[\hat{a}^2,\hat{\rho}_S] + F^*[\hat{a}^{\dagger 2},\hat{\rho}_S] \\ &- (M^* + P^*)[\hat{a}^\dagger\hat{a},\hat{\rho}_S] - G\big(\hat{a}^2\hat{\rho}_S - \hat{a}\hat{\rho}_S\hat{a}\big) \\ &+ G^*\big(\hat{a}^\dagger\hat{\rho}_S\hat{a}^\dagger - \hat{\rho}_S\hat{a}^{\dagger 2}\big) + O\big(\hat{a}\hat{\rho}_S\hat{a}^\dagger - \hat{a}^\dagger\hat{a}\hat{\rho}_S\big) \\ &+ R\big(\hat{a}^\dagger\hat{\rho}_S\hat{a} - \hat{a}\hat{a}^\dagger\hat{\rho}_S\big). \end{aligned} \tag{V.11}$$

Lastly, rewriting the last terms in Eq. (V.11) in Lindblad-like form and redefining the coefficients we obtain the TCL master equation (III.27).

D Parameters for the MCTDH-X computations

In Chpt. IV we have simulated the full-time evolution of the cavity-BEC system with $N = 1000$ atoms in a cavity driven by a transverse pump laser, cf. Fig. IV.1.

The dimensionless parameters used throughout the work are computed as follows. First we fix the length scale $L = 0.48\,\mu$m. The scale of energy for the specific choice of ^{87}Rb atoms is $\hbar^2/2mL^2 \approx 1.67 \times 10^{-31}$ J. Similarly, the scale of time is $2mL^2/\hbar \approx 0.63$ ms. In our computations the atoms have been chosen to interact weakly with each other with an interaction strength of $\lambda_0 \approx 0.01$ [cf. Eq. (I.27)]. In experiments λ_0 can be chosen by tuning the frequency of the transverse confining harmonic potential $\omega_\perp$. The one-dimensional scattering strength λ_0 is related to the three-dimensional scattering length a through $\lambda_0 = 4Lm\omega_\perp a/\hbar$ [174]. Using the listed parameters, and the fact that $a \approx 100a_0$ for ^{87}Rb, one obtains $\omega_\perp \approx 718$ Hz. The atom-cavity coupling $U_0 \approx 338.22$ Hz, the cavity resonance frequency $\omega_k \approx 2\pi \cdot 382.41$ THz and loss rate $\kappa \approx 2\pi \cdot 1.3$ MHz have been chosen in accordance with experimental values [37].

E MCTDH-X equations for a cavity-BEC system

When situated inside an optical cavity, the one-body Hamiltonian $\hat{h}$ [cf. Eq. (I.22) and (I.26)] has the form $\hat{h} = \hat{T} + V = \hat{T} + V_{\text{trap}} + V_{\text{cavity}}$, where $\hat{T}$ is the kinetic energy and V_{trap} the external potential. The potential V_{cavity} modifies the one-body Hamiltonian $\hat{h}$ in a time-dependent way: the atoms interact with the cavity field $a(t)$.

Since our numerical results in the main text are for a one-dimensional system, we use the coordinate x instead of $\mathbf{r}$ in the following.

The cavity field generates a potential $U(x)$ which contributes to the one-body potential V_{cavity},

$$U(x) = \frac{g_0^2}{\Delta_a} \cos^2(kx). \tag{V.12}$$

In addition, photons are scattered from the pump into the cavity field by the atoms, resulting in a cavity photon source term of the form

$$\eta(x,t) = \frac{g_0 \Omega_p(t)}{\Delta_a} \cos(kx). \tag{V.13}$$

Here g_0 is the atom-cavity coupling, Δ_a is the atomic detuning and Ω_p is the pump Rabi frequency, which depends on the pump laser power and in our case is explicitly time dependent. The combined one-body potential entering the many-body Hamiltonian of the combined system then reads

$$\begin{aligned} V(x,t) &= V_{\text{trap}}(x) + V_{\text{cavity}}(x,t) \\ &= V_{\text{trap}}(x) + V_0(t) + |a(t)|^2 U(x) + (a(t) + a^*(t))\,\eta(x,t). \end{aligned}$$

Here, $V_{\text{trap}}(x,t) = \frac{1}{2}\omega_x^2 x^2$ is the external trapping potential for the bosons, without the cavity, and $V_0(t) = \Omega_p^2(t)/\Delta_a$ is the potential created by the pump field.

The EOM of the cavity field $a(t)$ is given by

$$i\partial_t a(t) = \Big[-\Delta_c + \sum_{k,q=1}^{M} \Big(\rho_{kq}(t) U_{kq}\Big) - i\kappa \Big] a(t) + \sum_{k,q=1}^{M} \Big(\rho_{kq}(t)\eta_{kq}(t)\Big), \tag{V.14}$$

where we have introduced the matrix elements $U_{kq}(t) \equiv \langle \Phi_k | U(x) | \Phi_q \rangle$ and $\eta_{kq}(t) \equiv \langle \Phi_k | \eta(x,t) | \Phi_q \rangle$ using the orbitals Φ_i (see Sec. I.4) and Δ_c

is the cavity detuning. The complex damping term $-i\kappa$ has been introduced in order to deal with photon losses using the settled set of EOM, cf. (I.25), (I.26), (V.14).

F Mapping to the driven Dicke model

The Hamiltonian of the periodically driven Dicke model is given by [21, 121]

$$\mathcal{H}_S(t) = \omega_c \hat{a}^\dagger \hat{a} + \omega_a \hat{J}_z + \frac{\mu(t)}{\sqrt{N}}(\hat{a}^\dagger + \hat{a})(\hat{J}_+ + \hat{J}_-), \tag{V.15}$$

where ω_c is the cavity resonance frequency and ω_a is the level spacing of the two-level atoms. The operators $\hat{a}^{(\dagger)}$ are the standard annihilation/creation operators of the cavity field, while $\hat{J}_z$, $\hat{J}_+$, $\hat{J}_-$ are the atomic collective operators. The atom-cavity coupling is time-dependent and has the following explicit form: $\mu(t) = \mu_0 + \alpha\cos(2\Omega t)$. Using the standard Holstein-Primakoff transformation [107, 124], and assuming the number of particles N to be very large, allows us to write the Hamiltonian (V.15) in terms of bosonic operators $\hat{d}^{(\dagger)}$ as

$$H_S(t) = \omega_c a^\dagger a + \omega_a d^\dagger d + \mu(t)(a^\dagger + a)(d^\dagger + d). \tag{V.16}$$

The Hamiltonian (V.16) can be decoupled through a NM transformation (see Chpt. III), leading to

$$H_S(t) = \epsilon_+ c_+^\dagger c_+ + \epsilon_- c_-^\dagger c_-, \tag{V.17}$$

which is the Hamiltonian of two POs. The NM (polariton) dispersions for the experimental case ($\omega_c \gg \omega_a$) for the NP are given by

$$\left(\epsilon_+^{\mathrm{NP}}\right)^2 = \omega_c^2 + 4\mu^2(t)\frac{\omega_a}{\omega_c}, \tag{V.18}$$

$$\left(\epsilon_-^{\mathrm{NP}}\right)^2 = \omega_a^2 - 4\mu^2(t)\frac{\omega_a}{\omega_c}, \tag{V.19}$$

and for the SP by

$$\left(\epsilon_+^{\mathrm{SP}}\right)^2 = \omega_c^2 - \omega_a^2, \tag{V.20}$$

$$\left(\epsilon_-^{\mathrm{SP}}\right)^2 = 16\frac{\mu^4(t)}{\omega_c^2} - \omega_a^2. \tag{V.21}$$

Even though the system we study is more complex than the simple driven Dicke model studied in Ref. [21], this mapping helps us to estimate the periods at which the parametric instabilities emerge (cf. Sec. IV.2).

F

Bibliography

[1] L. D. Landau and E. M. Lifshitz, *Mechanics*, 3rd ed. (Elsevier, 1982).

[2] P. A. M. Dirac, "*The Quantum Theory of the Emission and Absorption of Radiation*," Proc. Royal Soc. Lond. A **114**, 243–265 (1927).

[3] N. W. Ashcroft and N. D. Mermin, *Solid State Physics* (Cengage, 2011).

[4] J. Bardeen, L. N. Cooper, and J. R. Schrieffer, "*Theory of Superconductivity*," Phys. Rev. **108**, 1175–1204 (1957).

[5] M. Faraday, "*On a peculiar class of acoustical figures; and on certain forms assumed by groups of particles upon vibrating elastic surfaces*," Philosophical transactions of the Royal Society of London **121**, 299–340 (1831).

[6] G. Floquet, "*Sur les equations differentielles lineaires a coefficients periodiques*," Ann. Sci. Ec. Norm. Sup. **12**, 47–88 (1883).

[7] G. W. Hill, "*On the part of the moon's motion which is a function of the mean motions of the sun and the moon*," Acta Math. **8**, 1–36 (1886).

[8] D. Rugar and P. Grütter, "*Mechanical parametric amplification and thermomechanical noise squeezing*," Phys. Rev. Lett. **67**, 699–702 (1991).

[9] D. W. Carr, S. Evoy, L. Sekaric, H. G. Craighead, and J. M. Parpia, "*Parametric amplification in a torsional microresonator*," Applied Physics Letters **77**, 1545–1547 (2000).

[10] W. Paul, "*Electromagnetic traps for charged and neutral particles*," Rev. Mod. Phys. **62**, 531–540 (1990).

[11] A. H. Nayfeh and D. T. Mook, *Nonlinear Oscillations*, Physics textbook (Wiley, 2008).

[12] E. A. Jackson, *Perspectives of nonlinear dynamics* (Cambridge University Press, 1989).

[13] H. W. C. Postma, I. Kozinsky, A. Husain, and M. L. Roukes, "*Dynamic range of nanotube- and nanowire-based electromechanical systems*," Applied Physics Letters **86**, 223105 (2005).

[14] L. G. Villanueva, E. Kenig, R. B. Karabalin, M. H. Matheny, R. Lifshitz, M. C. Cross, and M. L. Roukes, "*Surpassing Fundamental Limits of Oscillators Using Nonlinear Resonators*," Phys. Rev. Lett. **110**, 177208 (2013).

[15] R. B. Karabalin, R. Lifshitz, M. C. Cross, M. H. Matheny, S. C. Masmanidis, and M. L. Roukes, "*Signal Amplification by Sensitive Control of Bifurcation Topology*," Phys. Rev. Lett. **106**, 094102 (2011).

[16] H. Walther, T. H. V. Benjamin, B.-G. Englert, and T. Becker, "*Cavity quantum electrodynamics*," Rep. Prog. Phys. **69**, 1325 (2006).

[17] S. Haroche and J.-M. Raimond, *Exploring the quantum: atoms, cavities, and photons*, Oxford Graduate Texts (Oxford University Press, 2006).

[18] E. T. Jaynes and F. W. Cummings, "*Comparison of quantum and semiclassical radiation theories with application to the beam maser*," Proc. IEEE **51**, 89–109 (1963).

[19] F. W. Cummings, "*Stimulated Emission of Radiation in a Single Mode*," Phys. Rev. **140**, A1051–A1056 (1965).

[20] R. H. Dicke, "*Coherence in Spontaneous Radiation Processes*," Phys. Rev. **93**, 99–110 (1954).

[21] R. Chitra and O. Zilberberg, "*Dynamical many-body phases of the parametrically driven, dissipative Dicke model*," Phys. Rev. A **92**, 023815 (2015).

[22] M. Greiner, O. Mandel, T. Esslinger, T. W. Hänsch, and I. Bloch, "*Quantum phase transition from a superfluid to a Mott insulator in a gas of ultracold atoms*," Nature **415**, 39 EP – (2002).

[23] A. Polkovnikov, K. Sengupta, A. Silva, and M. Vengalattore, "*Colloquium: Nonequilibrium dynamics of closed interacting quantum systems*," Rev. Mod. Phys. **83**, 863–883 (2011).

[24] M. Grifoni and P. Hänggi, "*Driven quantum tunneling*," Phys. Rep. **304**, 229 – 354 (1998).

[25] S. Kohler, J. Lehmann, and P. Hänggi, "*Driven quantum transport on the nanoscale*," Phys. Rep. **406**, 379 – 443 (2005).

[26] M. Bukov, L. D'Alessio, and A. Polkovnikov, "*Universal high-frequency behavior of periodically driven systems: from dynamical stabilization to Floquet engineering*," Advances in Physics **64**, 139–226 (2015).

[27] H. Lignier, C. Sias, D. Ciampini, Y. Singh, A. Zenesini, O. Morsch, and E. Arimondo, "*Dynamical control of matter-wave tunneling in periodic potentials*," Phys. Rev. Lett. , 220403 (99).

[28] J. Gong, L. Morales-Molina, and P. Hänggi, "*Many-body coherent destruction of tunneling*," Phys. Rev. Lett. **103**, 133002 (2009).

[29] Y. Kayanuma and K. Saito, "*Coherent destruction of tunneling, dynamic localization, and the Landau-Zener formula*," Phys. Rev. A **77**, 010101 (2008).

[30] T. Nag, S. Roy, A. Dutta, and D. Sen, "*Dynamical localization in a chain of hard core bosons under periodic driving*," Phys. Rev. B **89**, 165425 (2014).

[31] L. D'Alessio and A. Polkovnikov, "*Many-body energy localization transition in periodically driven systems*," Annals of Physics **333**, 19 – 33 (2013).

[32] S. Fishman, D. R. Grempel, and R. E. Prange, "*Chaos, Quantum Recurrences, and Anderson Localization*," Phys. Rev. Lett. **49**, 509–512 (1982).

[33] A. Eckardt, C. Weiss, and M. Holthaus, "*Superfluid-insulator transition in a periodically driven optical lattice*," Phys. Rev. Lett. **95**, 260404 (2005).

[34] N. H. Lindner, G. Refael, and V. Galitski, "*Floquet topological insulator in semiconductor quantum wells*," Nature Physics **7**, 490–495 (2011).

[35] A. Kundu and B. Seradjeh, "*Transport Signatures of Floquet Majorana Fermions in Driven Topological Superconductors*," Phys. Rev. Lett. **111**, 136402 (2013).

[36] L. Jiang, T. Kitagawa, J. Alicea, A. R. Akhmerov, D. Pekker, G. Refael, J. I. Cirac, E. Demler, M. D. Lukin, and P. Zoller, "*Majorana Fermions in Equilibrium and in Driven Cold-Atom Quantum Wires*," Phys. Rev. Lett. **106**, 220402 (2011).

[37] K. Baumann, C. Guerlin, F. Brennecke, and T. Esslinger, "*Dicke quantum phase transition with a superfluid gas in an optical cavity*," Nature **464**, 1301–1306 (2010).

[38] A. Lazarides, A. Das, and R. Moessner, "*Equilibrium states of generic quantum systems subject to periodic driving*," Phys. Rev. E **90**, 012110 (2014).

[39] L. D'Alessio and M. Rigol, "*Long-time Behavior of Isolated Periodically Driven Interacting Lattice Systems*," Phys. Rev. X **4**, 041048 (2014).

[40] L. Papariello, O. Zilberberg, A. Eichler, and R. Chitra, "*Ultrasensitive hysteretic force sensing with parametric nonlinear oscillators*," Phys. Rev. E **94**, 022201 (2016).

[41] A. Leuch, L. Papariello, O. Zilberberg, C. L. Degen, R. Chitra, and A. Eichler, "*Parametric Symmetry Breaking in a Nonlinear Resonator*," Phys. Rev. Lett. **117**, 214101 (2016).

[42] L. Papariello and R. Chitra, "*Entanglement dynamics in the driven-dissipative Dicke model*," (2018), in preparation.

[43] K. Baumann, R. Mottl, F. Brennecke, and T. Esslinger, "*Exploring Symmetry Breaking at the Dicke Quantum Phase Transition*," Physical Review Letters **107**, 140402 (2011).

[44] F. Brennecke, R. Mottl, K. Baumann, R. Landig, T. Donner, and T. Esslinger, "*Real-time observation of fluctuations at the driven-dissipative Dicke phase transition*," Proc. Natl. Acad. Sci. U.S.A. **110 (29)**, 11763 (2013).

[45] P. Molignini, L. Papariello, A. U. J. Lode, and R. Chitra, "*Superlattice switching from parametric instabilities in a driven-dissipative BEC in a cavity*," Phys. Rev. A **98**, 053620 (2018).

[46] N. M. Krylov and N. N. Bogoliubov, *Introduction to Non-Linear Mechanics* (Princeton University Press, 1950).

[47] N. N. Bogoliubov and Y. A. Mitropolsky, *Asymptotic Methods in the Theory of Non-Linear Oscillations* (Gordon and Breach, 1961).

[48] M. Roseau, *Vibrations nonlinéaires et théorie de la stabilité* (Springer-Verlag, 1966).

[49] J. G. Besjes, "*On the asymptotic methods for non-linear differential equations*," Journal de Mécanique **8**, 357–373 (1969).

[50] L. M. Perko, "*Higher order averaging and related methods for perturbed periodic and quasi-periodic systems*," SIAM Journal on Applied Mathematics **17**, 698–724 (1969).

[51] J. Guckenheimer and P. Holmes, *Nonlinear oscillations, dynamical systems, and bifurcations of vector fields*, Applied mathematical sciences (Springer-Verlag, 1990).

[52] J. A. Sanders, F. Verhulst, and J. Murdock, *Averaging Methods in Nonlinear Dynamical Systems*, Applied Mathematical Sciences, Vol. 59 (Springer, 2007).

[53] Y. A. Mitropolsky and A. K. Lopatin, *Nonlinear Mechanics, Groups and Symmetry*, Mathematics and Its Applications, Vol. 319 (Springer, 1995).

[54] J. Murdock, *Normal Forms and Unfoldings for Local Dynamical Systems* (Springer, 2003).

[55] C. Holmes and P. Holmes, "*Second order averaging and bifurcations to subharmonics in duffing's equation*," Journal of Sound and Vibration **78**, 161 – 174 (1981).

[56] O. E. Alon, A. I. Streltsov, and L. S. Cederbaum, "*Unified view on multiconfigurational time propagation for systems consisting of identical particles*," J. Chem. Phys. **127**, 154103 (2007).

[57] O. E. Alon, A. I. Streltsov, and L. S. Cederbaum, "*The multi-configurational time-dependent Hartree method for bosons: Many-body dynamics of bosonic systems*," Phys. Rev. A **77**, 033613 (2008).

[58] P. Kramer and M. Saraceno, *Geometry of the Time-Dependent Variational Principle in Quantum Mechanics*, Lecture Notes in Physics, Vol. 140 (Springer-Verlag Berlin Heidelberg, 1981).

[59] C. J. Pethick and H. Smith, *Bose-Einstein Condensation in Dilute Gases*, 2nd ed. (Cambridge University Press, Cambridge, 2008).

[60] L. P. Pitaevskii and S. Stringari, *Bose-Einstein Condensation* (OxfordUniversityPress, 2003).

[61] M. Dykman, *Fluctuating Nonlinear Oscillators* (Oxford University Press, 2012).

[62] D. Rugar, R. Budakian, H. J. Mamin, and B. W. Chui, "*Single spin detection by magnetic resonance force microscopy*," Nature **430**, 329–332 (2004).

[63] Y. T. Yang, C. Callegari, X. L. Feng, K. L. Ekinci, and M. L. Roukes, "*Zeptogram-Scale Nanomechanical Mass Sensing*," Nano Letters **6**, 583–586 (2006).

[64] M. Poggio, "*Nanomechanics: Sensing from the bottom up*," Nat Nano **8**, 482–483 (2013).

[65] J. Chaste, A. Eichler, J. Moser, G. Ceballos, R. Rurali, and A. Bachtold, "*A nanomechanical mass sensor with yoctogram resolution*," Nat Nano **7**, 301–304 (2012).

[66] M. Aspelmeyer, T. J. Kippenberg, and F. Marquardt, "*Cavity optomechanics*," Rev. Mod. Phys. **86**, 1391–1452 (2014).

[67] S. Aldana, C. Bruder, and A. Nunnenkamp, "*Detection of weak forces based on noise-activated switching in bistable optomechanical systems*," Phys. Rev. A **90**, 063810 (2014).

[68] E. Mathieu, "*E. MATHIEU. — Mémoire sur le mouvement vibratoire des cloches (Journal de l'École Polytechnique, LIe Cahier, 1882)*," J. Phys. Theor. Appl. **2**, 32–33 (1883).

[69] W. Magnus and S. Winkler, *Hill's equation* (Interscience Publishers, 1966).

[70] N. McLachlan, *Theory and application of Mathieu functions* (Clarendon, 1951).

[71] C. M. Caves, "*Quantum-mechanical noise in an interferometer*," Phys. Rev. D **23**, 1693–1708 (1981).

[72] M. A. Castellanos-Beltran and K. W. Lehnert, "*Widely tunable parametric amplifier based on a superconducting quantum interference device array resonator*," Appl. Phys. Lett. **91**, 083509 (2007).

[73] I. Mahboob, E. Flurin, K. Nishiguchi, A. Fujiwara, and H. Yamaguchi, "*Interconnect-free parallel logic circuits in a single mechanical resonator*," Nat. Commun. **2**, 198 (2011).

[74] C. Eichler, Y. Salathe, J. Mlynek, S. Schmidt, and A. Wallraff, "*Quantum-Limited Amplification and Entanglement in Coupled Nonlinear Resonators*," Phys. Rev. Lett. **113**, 110502 (2014).

[75] A. Szorkovszky, A. A. Clerk, A. C. Doherty, and W. P. Bowen, "*Mechanical entanglement via detuned parametric amplification*," New J. Phys. **16**, 063043 (2014).

[76] I. Mahboob and H. Yamaguchi, "*Bit storage and bit flip operations in an electromechanical oscillator*," Nat Nano **3**, 275–279 (2008).

[77] W. Zhang, R. Baskaran, and K. L. Turner, "*Effect of cubic nonlinearity on auto-parametrically amplified resonant {MEMS} mass sensor*," Sensors and Actuators A: Physical **102**, 139–150 (2002).

[78] R. H. Rand, "*Lecture Notes on Nonlinear Vibrations*," (2000).

[79] L. Ruby, "*Applications of the Mathieu equation*," Am. J. Phys. **64**, 39–44 (1996).

[80] W. M. Dougherty, K. J. Bruland, J. L. Garbini, and J. A. Sidles, "*Detection of AC magnetic signals by parametric mode coupling in a mechanical oscillator*," Meas. Sci. Technol. **7**, 1733 (1996).

[81] A. Szorkovszky, A. C. Doherty, G. I. Harris, and W. P. Bowen, "*Mechanical Squeezing via Parametric Amplification and Weak Measurement*," Phys. Rev. Lett. **107**, 213603 (2011).

[82] L. Rayleigh, "*XVII. On the maintenance of vibrations by forces of double frequency, and on the propagation of waves through a medium endowed with a periodic structure*," The London, Edinburgh, and Dublin Philosophical Magazine and Journal of Science **24**, 145–159 (1887).

[83] A. Eichler, J. Moser, J. Chaste, M. Zdrojek, I. Wilson-Rae, and A. Bachtold, "*Nonlinear damping in mechanical resonators made from carbon nanotubes and graphene*," Nat Nano **6**, 339–342 (2011).

[84] J. Gieseler, B. Deutsch, R. Quidant, and L. Novotny, "*Subkelvin Parametric Feedback Cooling of a Laser-Trapped Nanoparticle*," Phys. Rev. Lett. **109**, 103603 (2012).

[85] M. C. Lifshitz, R. Cross, "*Nonlinear Dynamics of Nanomechanical and Micromechanical Resonators*," in *Reviews of Nonlinear Dynamics and Complexity* (Wiley-VCH, 2009) pp. 1–52.

[86] A. A. Batista, "*Cooling, heating, and thermal noise squeezing in a parametrically driven resonator*," Journal of Statistical Mechanics: Theory and Experiment **2011**, P02007 (2011).

[87] P. Hartman, *Ordinary Differential Equations* (Wiley, 1964).

[88] D. Ryvkine and M. I. Dykman, "*Resonant symmetry lifting in a parametrically modulated oscillator*," Phys. Rev. E **74**, 061118 (2006).

[89] J. Gieseler, M. Spasenović, L. Novotny, and R. Quidant, "*Nonlinear Mode Coupling and Synchronization of a Vacuum-Trapped Nanoparticle*," Phys. Rev. Lett. **112**, 103603 (2014).

[90] A. Eichler, J. Chaste, J. Moser, and A. Bachtold, "*Parametric Amplification and Self-Oscillation in a Nanotube Mechanical Resonator*," Nano Letters **11**, 2699–2703 (2011).

[91] J. Moser, A. Eichler, J. Güttinger, M. I. Dykman, and A. Bachtold, "*Nanotube mechanical resonators with quality factors of up to 5 million*," Nat Nano **9**, 1007–1011 (2014).

[92] J. A. Sidles, "*Noninductive detection of single-proton magnetic resonance*," Appl. Phys. Lett. **58**, 2854–2856 (1991).

[93] C. L. Degen, M. Poggio, H. J. Mamin, C. T. Rettner, and D. Rugar, "*Nanoscale magnetic resonance imaging*," Proceedings of the National Academy of Sciences **106**, 1313–1317 (2009).

[94] A. Eichler, T. L. Heugel, A. Leuch, C. L. Degen, R. Chitra, and O. Zilberberg, "*A parametric symmetry breaking transducer*," Appl. Phys. Lett. **112**, 233105 (2018).

[95] A. Cartella, T. F. Nova, M. Fechner, R. Merlin, and A. Cavalleri, "*Parametric amplification of optical phonons*," (2017), arXiv:1708.09231 [cond-mat.mtrl-sci] .

[96] A. von Hoegen, R. Mankowsky, M. Fechner, M. Först, and A. Cavalleri, "*Probing the interatomic potential of solids with strong-field nonlinear phononics*," Nature **555**, 79 EP – (2018).

[97] A. P. Itin and M. I. Katsnelson, "*Efficient excitation of nonlinear phonons via chirped pulses: Induced structural phase transitions*," Phys. Rev. B **97**, 184304 (2018).

[98] V. Anisimov and Y. Izyumov, *Electronic Structure of Strongly Correlated Materials*, Springer Series in Solid-State Sciences (Springer-Verlag Berlin Heidelberg, 2010).

[99] D. Fausti, R. I. Tobey, N. Dean, S. Kaiser, A. Dienst, M. C. Hoffmann, S. Pyon, T. Takayama, H. Takagi, and A. Cavalleri, "*Light-Induced Superconductivity in a Stripe-Ordered Cuprate*," Science **331**, 189–191 (2011).

[100] R. Mankowsky, A. Subedi, M. Först, S. O. Mariager, M. Chollet, H. T. Lemke, J. S. Robinson, J. M. Glownia, M. P. Minitti, A. Frano, M. Fechner, N. A. Spaldin, T. Loew, B. Keimer, A. Georges, and A. Cavalleri, "*Nonlinear lattice dynamics as a basis for enhanced superconductivity in YBa2Cu3O6.5*," Nature **516**, 71 EP – (2014).

[101] M. Mitrano, A. Cantaluppi, D. Nicoletti, S. Kaiser, A. Perucchi, S. Lupi, P. Di Pietro, D. Pontiroli, M. Riccò, S. R. Clark, D. Jaksch, and A. Cavalleri, "*Possible light-induced superconductivity in K3C60 at high temperature*," Nature **530**, 461 EP – (2016).

[102] M. Marthaler and M. I. Dykman, "*Switching via quantum activation: A parametrically modulated oscillator*," Phys. Rev. A **73**, 042108 (2006).

[103] M. Gross and S. Haroche, "*Superradiance: An essay on the theory of collective spontaneous emission*," Phys. Rep. **93**, 301 – 396 (1982).

[104] B. M. Garraway, "*The Dicke model in quantum optics: Dicke model revisited*," Phil. Trans. R. Soc. A **369**, 1137–1155 (2011).

[105] K. Hepp and E. H. Lieb, "*Equilibrium Statistical Mechanics of Matter Interacting with the Quantized Radiation Field*," Phys. Rev. A **8**, 2517–2525 (1973).

[106] C. Emary and T. Brandes, "*Quantum Chaos Triggered by Precursors of a Quantum Phase Transition: The Dicke Model*," Phys. Rev. Lett. **90**, 044101 (2003).

[107] C. Emary and T. Brandes, "*Chaos and the quantum phase transition in the Dicke model*," Phys. Rev. E **67**, 066203 (2003).

[108] N. Skribanowitz, I. P. Herman, J. C. MacGillivray, and M. S. Feld, "*Observation of Dicke Superradiance in Optically Pumped HF Gas*," Phys. Rev. Lett. **30**, 309–312 (1973).

[109] M. Gross, C. Fabre, P. Pillet, and S. Haroche, "*Observation of Near-Infrared Dicke Superradiance on Cascading Transitions in Atomic Sodium*," Phys. Rev. Lett. **36**, 1035–1038 (1976).

[110] A. Flusberg, T. Mossberg, and S. R. Hartmann, "*Observation of Dicke superradiance at 1.30 μm in atomic Tl vapor*," Phys. Lett. A **58**, 373 – 374 (1976).

[111] A. Crubellier, S. Liberman, and P. Pillet, "*Doppler-Free Superradiance Experiments with Rb Atoms: Polarization Characteristics*," Phys. Rev. Lett. **41**, 1237–1240 (1978).

[112] M. Gross, J. M. Raimond, and S. Haroche, "*Doppler Beats in Superradiance*," Phys. Rev. Lett. **40**, 1711–1714 (1978).

[113] F. Gounand, M. Hugon, P. R. Fournier, and J. Berlande, "*Superradiant cascading effects in rubidium Rydberg levels*," J. Phys. B **12**, 547 (1979).

[114] P. Cahuzac, H. Sontag, and P. E. Toschek, "*Visible superfluorescence from atomic Europium*," Opt. Comm. **31**, 37 – 41 (1979).

[115] N. W. Carlson, D. J. Jackson, A. L. Schawlow, M. Gross, and S. Haroche, "*Superradiance triggering spectroscopy*," Opt. Comm. **32**, 350 – 354 (1980).

[116] L. Moi, C. Fabre, P. Goy, M. Gross, S. Haroche, P. Encrenaz, G. Beaudin, and B. Lazareff, "*Heterodyne detection of Rydberg atom maser emission*," Opt. Comm. **33**, 47 – 50 (1980).

[117] L. Moi, P. Goy, M. Gross, J. M. Raimond, C. Fabre, and S. Haroche, "*Rydberg-atom masers. I. A theoretical and experimental study of super-radiant systems in the millimeter-wave domain*," Phys. Rev. A **27**, 2043–2064 (1983).

[118] F. Dimer, B. Estienne, A. S. Parkins, and H. J. Carmichael, "*Proposed realization of the Dicke-model quantum phase transition in an optical cavity QED system*," Phys. Rev. A **75**, 013804 (2007).

[119] P. Domokos and H. Ritsch, "*Collective Cooling and Self-Organization of Atoms in a Cavity*," Phys. Rev. Lett. **89**, 253003 (2002).

[120] D. Nagy, G. Kónya, G. Szirmai, and P. Domokos, "*Dicke-Model Phase Transition in the Quantum Motion of a Bose-Einstein Condensate in an Optical Cavity*," Phys. Rev. Lett. **104**, 130401 (2010).

[121] V. M. Bastidas, C. Emary, B. Regler, and T. Brandes, "*Nonequilibrium Quantum Phase Transitions in the Dicke Model*," Phys. Rev. Lett. **108**, 043003 (2012).

[122] L. P. Kadanoff and G. Baym, *Quantum Statistical Mechanics*, Frontiers in physics (W.A. Benjamin, 1962).

[123] K. Huang, *Statistical Mechanics* (Wiley, New York, 1987).

[124] T. Holstein and H. Primakoff, "*Field Dependence of the Intrinsic Domain Magnetization of a Ferromagnet*," Phys. Rev. **58**, 1098–1113 (1940).

[125] R. K. Bullough, "*Photon, quantum and collective, effects from Rydberg atoms in cavities*," Hyperfine Interact. **37**, 71–108 (1987).

[126] H. Zoubi, M. Orenstien, and A. Ron, "*Coupled microcavities with dissipation*," Phys. Rev. A **62**, 033801 (2000).

[127] C. Zerbe and P. Hänggi, "*Brownian parametric quantum oscillator with dissipation*," Phys. Rev. E **52**, 1533–1543 (1995).

[128] F. Galve, L. A. Pachón, and D. Zueco, "*Bringing Entanglement to the High Temperature Limit*," Phys. Rev. Lett. **105**, 180501 (2010).

[129] R. P. Feynman and F. L. Vernon, "*The theory of a general quantum system interacting with a linear dissipative system*," Ann. Phys. **24**, 118 – 173 (1963).

[130] H.-T. Tan and W.-M. Zhang, "*Non-Markovian dynamics of an open quantum system with initial system-reservoir correlations: A nanocavity coupled to a coupled-resonator optical waveguide*," Phys. Rev. A **83**, 032102 (2011).

[131] K. W. Chang and C. K. Law, "*Non-Markovian master equation for a damped oscillator with time-varying parameters*," Phys. Rev. A **81**, 052105 (2010).

[132] A. Caldeira and A. Leggett, "*Path integral approach to quantum Brownian motion*," Physica A: Statistical Mechanics and its Applications **121**, 587 – 616 (1983).

[133] A. Kossakowski, "*On quantum statistical mechanics of non-Hamiltonian systems*," Rep. Math. Phys. **3**, 247 – 274 (1972).

[134] G. Lindblad, "*On the generators of quantum dynamical semigroups*," Commun. Math. Phys. **48**, 119–130 (1976).

[135] H. P. Breuer and F. Petruccione, *The Theory of Open Quantum Systems* (Oxford University Press, 2007).

[136] U. Weiss, *Quantum Dissipative Systems* (World Scientific, 2008).

[137] M. Tokuyama and H. Mori, "*Statistical-Mechanical Theory of the Boltzmann Equation and Fluctuations in μ Space*," Progress of Theoretical Physics **56**, 1073–1092 (1976).

[138] F. Shibata, Y. Takahashi, and N. Hashitsume, "*A generalized stochastic liouville equation. Non-Markovian versus memoryless master equations*," J. Stat. Phys. **17**, 171–187 (1977).

[139] S. Chaturvedi and F. Shibata, "*Time-convolutionless projection operator formalism for elimination of fast variables. Applications to Brownian motion*," Z. Phys. B **35**, 297–308 (1979).

[140] F. Shibata and T. Arimitsu, "*Expansion Formulas in Nonequilibrium Statistical Mechanics*," J. Phys. Soc. Jap. **49**, 891–897 (1980).

[141] D. Nagy, G. Szirmai, and P. Domokos, "*Critical exponent of a quantum-noise-driven phase transition: The open-system Dicke model*," Phys. Rev. A **84**, 043637 (2011).

[142] M. A. Schlosshauer, *Decoherence: and the Quantum-To-Classical Transition* (Springer, 2007).

[143] M. A. Nielsen, *Quantum Computation and Quantum Information* (Cambridge University Press, 2010).

[144] R. Horodecki, P. Horodecki, M. Horodecki, and K. Horodecki, "*Quantum entanglement*," Rev. Mod. Phys. **81**, 865–942 (2009).

[145] B. L. Schumaker, "*Quantum mechanical pure states with gaussian wave functions*," Physics Reports **135**, 317 – 408 (1986).

[146] G. Adesso, S. Ragy, and A. R. Lee, "*Continuous Variable Quantum Information: Gaussian States and Beyond*," Open Syst. Inf. Dyn. **21**, 1440001 (2014).

[147] A. Peres, "*Separability Criterion for Density Matrices*," Phys. Rev. Lett. **77**, 1413–1415 (1996).

[148] M. Horodecki, P. Horodecki, and R. Horodecki, "*Separability of mixed states: necessary and sufficient conditions*," Physics Letters A **223**, 1 – 8 (1996).

[149] G. Vidal and R. F. Werner, "*Computable measure of entanglement*," Phys. Rev. A **65**, 032314 (2002).

[150] J. Williamson, "*On the Algebraic Problem Concerning the Normal Forms of Linear Dynamical Systems*," Am. J. Math. **58**, 141–163 (1936).

[151] G. Adesso, A. Serafini, and F. Illuminati, "*Extremal entanglement and mixedness in continuous variable systems*," Phys. Rev. A **70**, 022318 (2004).

[152] J. P. Paz and A. J. Roncaglia, "*Dynamics of the Entanglement between Two Oscillators in the Same Environment*," Phys. Rev. Lett. **100**, 220401 (2008).

[153] J. P. Paz and A. J. Roncaglia, "*Dynamical phases for the evolution of the entanglement between two oscillators coupled to the same environment*," Phys. Rev. A **79**, 032102 (2009).

[154] K.-L. Liu and H.-S. Goan, "*Non-Markovian entanglement dynamics of quantum continuous variable systems in thermal environments*," Phys. Rev. A **76**, 022312 (2007).

[155] A. K. Rajagopal and R. W. Rendell, "*Decoherence, correlation, and entanglement in a pair of coupled quantum dissipative oscillators*," Phys. Rev. A **63**, 022116 (2001).

[156] P. J. Dodd and J. J. Halliwell, "*Disentanglement and decoherence by open system dynamics*," Phys. Rev. A **69**, 052105 (2004).

[157] P. J. Dodd, "*Disentanglement by dissipative open system dynamics*," Phys. Rev. A **69**, 052106 (2004).

[158] T. Yu and J. H. Eberly, "*Finite-Time Disentanglement Via Spontaneous Emission*," Phys. Rev. Lett. **93**, 140404 (2004).

[159] E. Wigner, "*On the Quantum Correction For Thermodynamic Equilibrium*," Phys. Rev. **40**, 749–759 (1932).

[160] M. Hillery, R. F. O'Connell, M. O. Scully, and E. P. Wigner, "*Distribution functions in physics: Fundamentals*," Phys. Rep. **106**, 121 – 167 (1984).

[161] C. K. Zachos, D. B. Fairlie, and T. L. Curtright, eds., *Quantum Mechanics in Phase Space: An Overview with Selected Papers* (World Scientific, 2005).

[162] A. Polkovnikov, "*Phase space representation of quantum dynamics*," Ann. Physics **325**, 1790 – 1852 (2010).

[163] J. Preskill, "*Quantum information and physics: Some future directions*," J. Mod. Opt. **47**, 127–137 (2000).

[164] T. J. Osborne and M. A. Nielsen, "*Entanglement in a simple quantum phase transition*," Phys. Rev. A **66**, 032110 (2002).

[165] J. Vidal, R. Mosseri, and J. Dukelsky, "*Entanglement in a first-order quantum phase transition*," Phys. Rev. A **69**, 054101 (2004).

[166] J. Vidal, G. Palacios, and R. Mosseri, "*Entanglement in a second-order quantum phase transition*," Phys. Rev. A **69**, 022107 (2004).

[167] M.-F. Yang, "*Reexamination of entanglement and the quantum phase transition*," Phys. Rev. A **71**, 030302 (2005).

[168] W. H. Louisell, *Quantum Statistical Properties of Radiation*, Wiley Classics Library (Wiley, 1990).

[169] A. Altland and F. Haake, "*Quantum Chaos and Effective Thermalization*," Phys. Rev. Lett. **108**, 073601 (2012).

[170] G. Engelhardt, V. M. Bastidas, C. Emary, and T. Brandes, "*ac-driven quantum phase transition in the Lipkin-Meshkov-Glick model*," Phys. Rev. E **87**, 052110 (2013).

[171] R. Lin, L. Papariello, P. Molignini, R. Chitra, and A. U. J. Lode, "*Superfluid–Mott insulator transition of ultracold superradiant bosons in a cavity*," (2018), arXiv:1811.09634 [cond-mat.quant-gas] .

[172] A. U. J. Lode, F. S. Diorico, R. Wu, P. Molignini, L. Papariello, R. Lin, C. Lévêque, L. Exl, M. C. Tsatsos, R. Chitra, and N. J. Mauser, "*Many-body physics in two-component Bose–Einstein condensates in a cavity: fragmented superradiance and polarization*," New J. Phys. **20**, 055006 (2018).

[173] D. Nagy, G. Szirmai, and P. Domokos, "*Self-organization of a Bose-Einstein condensate in an optical cavity*," European Physical Journal D **48**, 127–137 (2008).

[174] M. Olshanii, "*Atomic Scattering in the Presence of an External Confinement and a Gas of Impenetrable Bosons*," Phys. Rev. Lett. **81**, 938–941 (1998).

[175] G. Kurizki, I. E. Mazets, D. H. J. O'Dell, and W. P. Schleich, "*Bose-Einstein Condensates with laser-induced dipole-dipole interactions beyond the mean-field approach*," Int. J. Mod. Phys. **18**, 961 (2004).

[176] I. B. Maschler, C. Mekhov and H. Ritsch, "*Ultracold atoms in optical lattices generated by quantized light fields*," Eur. Phys. J. D **46**, 545–560 (2008).

[177] A. U. J. Lode, M. C. Tsatsos, and E. Fasshauer, *MCTDH-X: The time-dependent multiconfigurational Hartree for indistinguishable particles software*.

[178] E. Fasshauer and A. U. J. Lode, "*Multiconfigurational time-dependent Hartree method for fermions: Implementation, exactness, and few-fermion tunneling to open space*," Phys. Rev. A **93**, 033635 (2016).

[179] A. U. J. Lode, "*Multiconfigurational time-dependent Hartree method for bosons with internal degrees of freedom: Theory and composite fragmentation of multicomponent Bose-Einstein condensates*," Phys. Rev. A **93**, 063601 (2016).

[180] A. U. J. Lode and C. Bruder, "*Fragmented Superradiance of a Bose-Einstein Condensate in an Optical Cavity*," Phys. Rev. Lett. **118**, 013603 (2017).

[181] A. I. Streltsov, O. E. Alon, and L. S. Cederbaum, "*Role of excited states in the splitting dynamics of interacting Bose-Einstein condensates when ramping-up a barrier*," Phys. Rev. Lett. **99**, 030402 (2007).

[182] T. Langen, T. Gasenzer, and J. Schmiedmayer, "*Prethermalization and universal dynamics in near-integrable quantum systems*," J. Stat. Mech.: Theor. Exp. , 064009 (2016).

[183] T. Langen, S. Erne, R. Geiger, B. Rauer, T. Schweigler, M. Kuhnert, W. Rohringer, I. E. Mazets, T. Gasenzer, and J. Schmiedmayer, "*Experimental observation of a generalized Gibbs ensemble*," Science **348**, 207–211 (2015).

[184] D.-G. Lai, F. Zou, B.-P. Hou, Y.-F. Xiao, and J.-Q. Liao, "*Simultaneous cooling of coupled mechanical resonators in cavity optomechanics*," Phys. Rev. A **98**, 023860 (2018).

[185] F. Piazza, P. Strack, and W. Zwerger, "*Bose–Einstein condensation versus Dicke–Hepp–Lieb transition in an optical cavity*," Annals of Physics **339**, 135 – 159 (2013).

[186] J. Klinder, H. Keßler, M. R. Bakhtiari, M. Thorwart, and A. Hemmerich, "*Observation of a Superradiant Mott Insulator in the Dicke-Hubbard Model*," Phys. Rev. Lett. **115**, 230403 (2015).

[187] R. Mottl, *Roton-type mode softening in a dissipative quantum many-body system with cavity-mediated long-range interactions*, Ph.D. thesis, ETH Zurich (2014).

[188] S. Wessel, F. Alet, M. Troyer, and G. G. Batrouni, "*Quantum Monte Carlo simulations of confined bosonic atoms in optical lattices*," Phys. Rev. A **70**, 053615 (2004).

[189] Y. Kato, Q. Zhou, N. Kawashima, and N. Trivedi, "*Sharp peaks in the momentum distribution of bosons in optical lattices in the normal state*," Nature Physics **4**, 617 EP – (2008).

[190] F. Mivehvar, F. Piazza, and H. Ritsch, "*Disorder-Driven Density and Spin Self-Ordering of a Bose-Einstein Condensate in a Cavity*," Phys. Rev. Lett. **119**, 063602 (2017).

Notations

*	Complex conjugation
$^\top$	Matrix transpose
†	Hermitian conjugation
$\lvert 0\rangle$, $\lvert \mathrm{vac}\rangle$	Vacuum for ladder operators
$\dot{}$	Indicates the first time derivative
$\ddot{}$	Indicates the second time derivative
$\lvert\cdot\rvert$	Absolute value of a scalar
$\lVert\cdot\rVert$	Vector norm
$[\cdot,\cdot]$	Commutator
$\{\cdot,\cdot\}$	Anti-commutator
$\langle\cdot\rangle$	Indicates the expectation value
$\langle\cdot\rangle_T$	Indicates the time average over a period T
$\otimes$	Direct/tensor/Kronecker product
$\mathbb{I}, \mathbb{I}_n$	Unit matrix (identity operator) of a given dimension n
$\mathbb{1}_{\{\cdot\}}$	Indicator function
$\hat{a}^\dagger$, $\hat{a}$	Raising and lowering ladder operator
β	Thermodynamic beta, $\beta = 1/k_B T$
$\delta_{i,j}$	Kronecker symbol
$\delta(x)$	Dirac delta "function"
D	Indicates the Jacobian matrix of a vector function
∂_i	Partial derivative with respect to coordinate i
∇	Del (nabla) operator
e	Euler's number 2.718 . . .
ε	Infinitesimally small positive real number
$\hbar$	(Reduced) Planck constant $1.0545718 \times 10^{-35}$ Js
i	Imaginary unit, $i^2 = -1$
Im	Imaginary part of a complex expression

$\mathcal{O}$	Big $\mathcal{O}$ otation to describe limiting behavior
$\mathcal{P}$	Cauchy principal value
$\hat{\Psi}$, $\hat{\Psi}^\dagger$	Field operators
Re	Real part of a complex expression
Tr	Indicates the trace of an operator
$\mathbb{Z}$	Integers
$\mathbb{Z}_2$	Cyclic group of order 2

List of acronyms

AM	Averaging Method
CM	Covariance matrix
D-NP	Dynamical normal phase
DM	Dicke model
EOM	Equation(s) of motion
FWHM	Full width at half maximum
HO	Harmonic oscillator
JC	Jaynes-Cummings
MaPaReP	Many-body parametric resonance phase
MCTDH-X	Multiconfigurational time-dependent Hartree method for indistinguishable particles
NIT	Near-identity transformation
NM	Normal mode
NP	Normal phase
PO	Parametric oscillator
QED	Quantum electrodynamics

QPT	Quantum phase transition
RWA	Rotating wave approximation
SMI	Self-organized Mott insulator
SP	Superradiant phase
SSF	Self-organized superfluid
TCL	Time-convolutionless

List of publications

1. **L. Papariello**, O. Zilberberg, A. Eichler, and R. Chitra, "*Ultrasensitive hysteretic force sensing with parametric nonlinear oscillators*", Phys. Rev. E **94**, 022201 (2016).

2. A. Leuch*, **L. Papariello***, O. Zilberberg, C. L. Degen, R. Chitra, and A. Eichler, "*Parametric Symmetry Breaking in a Nonlinear Resonator*", Phys. Rev. Lett. **117**, 214101 (2016).

3. Axel U. J. Lode, F. S. Diorico, R. Wu, P. Molignini, **L. Papariello**, R. Lin, C. Lévêque, L. Exl, M. C. Tsatsos, R. Chitra, and N. J. Mauser, "*Many-body physics in two-component Bose-Einstein condensates in a cavity: fragmented superradiance and polarization*", New J. Phys. **20**, 055006 (2018).

4. P. Molignini*, **L. Papariello***, Axel U. J. Lode, and R. Chitra, "*Superlattice switching from parametric instabilities in a driven-dissipative BEC in a cavity*", Phys. Rev. A **98**, 053620 (2018).

5. R. Lin, **L. Papariello**, P. Molignini, R. Chitra, and Axel U. J. Lode, "*Superfluid–Mott insulator transition of ultracold superradiant bosons in a cavity*", (2018), arXiv:1811.09634 [cond-mat.quant-gas].

6. **L. Papariello** and R. Chitra, "*Entanglement dynamics in the driven-dissipative Dicke model*", in preparation.

◇ New detection scheme for weak forces filed as a patent with the title "**Method and sensor for measuring small forces**" by the European Patent Office. Patent number: EP 3171145 (A1).

*Equal first author credit.

Curriculum Vitae

Personal data

Name	Luca Papariello
Date of birth	July 8, 1989
Citizen of	Bellinzona TI, Switzerland
Nationality	Swiss

Education

2015 – 2018	**Doctoral studies in theoretical physics** ETH Zurich, Switzerland Advisor: Dr. R. Chitra
2012 – 2014	**Master of Science in physics** ETH Zurich, Switzerland Thesis advisors: Dr. R. Chitra, Prof. Dr. Oded Zilberberg
2008 – 2012	**Bachelor of Science in physics** ETH Zurich, Switzerland

Acknowledgements

I wish to express my gratitude to all the people that supported me during the past four years. Without their presence, this work would not have reached its full blossom.

First and foremost, I would like to express my gratitude to my supervisor Chitra Ramasubramanian. I have profited considerably from her insights and extraordinary view for the bigger picture. What I value the most is her presence and guidance throughout my thesis. I am also very grateful to Manfred Sigrist for welcoming me into his group and bringing me into contact with Chitra. Manfred is a great teacher and it was a big pleasure to be teaching assistant for one of his lectures. Furthermore, I am indebted to my co-examiner Christoph Bruder for his insightful comments on my work and, above all, for his warm hospitality every time I visited his group in Basel.

During my PhD studies I had the opportunity to work with many colleagues. First, I would like to thank Oded Zilberberg, who was like a second supervisor during the first half of my academic life. I am also indebted to him for bringing me in touch with Axel Lode. Further, he has the merit of having strongly believed in the force sensing project and pushed for filing a patent. The guitar experiment would not have been possible without the exceptional know-how of Alexander Eichler, the great work done by Anina Leuch and the help of Christian Degen, who allowed us to use his laboratories. It was great to collaborate on this extravagant project! Axel Lode is responsible for the gradual shift of my interests towards the numerical side, which now I appreciate very much and still plays an important role for my post-academic career. His sense of humor made our collaborations very enjoyable. A special thank goes to Paolo Molignini, with whom I shared most of my time as a PhD

student. I really appreciated collaborating with him and, in particular, our interpersonal interactions and the many funny moments we shared. Besides, I had the pleasure to be co-supervisor of two excellent master students: Toni Heugel and Rui Lin, from whom I also learned a lot.

My time at ETH Zurich would surely not have been as enjoyable without the nice atmosphere in the Institute for Theoretical Physics. In particular, I would like to thank all the former and present members of the condensed matter theory groups I had the pleasure of spending time with these past four years. A special thank goes to Daniel Braitsch and Urs Hähner, with whom I spent a lot of time talking about cycling as well as climbing the nicest mountain passes out there!

Dal punto di vista personale vorrei ringraziare tutti i miei amici per portare bei momenti di distrazione e divertimento nella mia vita. Vorrei inoltre esprimere la mia profonda gratitudine ai miei genitori per avermi dato la possibilità di affrontare questo percorso universitario che è culminato col dottorato. Sono enormemente grato a loro, così come a mia sorella Fanja e al suo ragazzo Matteo, per tutto il sostegno datomi durante questi anni. Il mio ringraziamento più grande va alla mia straordinaria fidanzata, Sara Svaluto-Ferro, per essermi stata sempre vicina e avermi supportato in ogni momento di questa avventura. Infine vorrei ringraziare tutta la sua famiglia – che per me costituisce una sorta di seconda famiglia – e, in particolar modo, Nicole e Mirko Selber per avermi gentilmente ospitato durante i miei ultimi mesi a Zurigo.

Luca Papariello
Zürich, 14 December 2018